

**Measurement of charged particle multiplicity distributions in
Au+Au collisions up to 200 GeV**

by

Pradeep Sarin

B. Tech., Engineering Physics, 1997,
Indian Institute of Technology, Bombay, India

Submitted to the Department of Physics
in partial fulfillment of the requirements for the degree of

Doctor of Philosophy in Physics

at the

MASSACHUSETTS INSTITUTE OF TECHNOLOGY

June 2003

© Massachusetts Institute of Technology 2003. All rights reserved.

Author
Department of Physics
May 2, 2003

Certified by
Boleslaw Wyslouch
Professor of Physics
Thesis Supervisor

Accepted by
Thomas J. Greytak
Associate Department Head for Education

Measurement of charged particle multiplicity distributions in Au+Au collisions up to 200 GeV

by

Pradeep Sarin

Submitted to the Department of Physics
on May 2, 2003, in partial fulfillment of the
requirements for the degree of
Doctor of Philosophy in Physics

Abstract

Au+Au collisions in the Relativistic Heavy Ion Collider (RHIC) herald a new era of opportunities for studying hadronic matter under conditions of high energy density and nucleon density. The theory of strong interactions, Quantum Chromodynamics (QCD), tells us very little about the dynamics of a strongly interacting many-body system in this non-perturbative regime. Therefore, characterizing the collisions using global extrinsic observables becomes important.

The distribution of charged particles produced in an ultra-relativistic heavy ion collision, being proportional to the initial energy density in the collision volume, is one such global observable. An anomalous change in particle multiplicity from lower energy collisions and/or peripheral to central collisions could indicate the onset of non-perturbative effects like deconfinement of quarks and gluons, or non-linear dynamics such as parton saturation.

We determine the pseudo-rapidity distribution of charged particles from hits recorded in pixels of the PHOBOS silicon multiplicity detector, after applying corrections for detector acceptance, occupancy and background particles. The collision centrality is estimated by measuring the energy deposited in scintillator trigger detectors and comparing it to Monte Carlo simulations for events with different impact parameters.

We find the total number of charged particles produced in central Au+Au collisions at $\sqrt{s_{NN}} = 130$ GeV and $\sqrt{s_{NN}} = 200$ GeV to be 4160 ± 210 and 5050 ± 250 respectively. The pseudo-rapidity distributions of charged particles show two remarkable features. In the fragmentation region, the distribution follows a limiting curve independent of the collision energy, similar to the limiting fragmentation behaviour seen earlier in $p + p$ and $p + A$ collisions. In the mid-rapidity region, the yield of charged particles evolves smoothly as a function of $\sqrt{s_{NN}}$ and collision centrality. We compare our results with a compilation of data from lower energy $p + p$, $p + A$ and $A + A$ collisions and discuss their implications for various phenomenological models of particle production.

Thesis Supervisor: Boleslaw Wyslouch
Title: Professor of Physics

Contents

1	Introduction	9
1.1	Motivation for colliding heavy ions	16
1.2	Particle production in heavy ion collisions: Overview	22
1.3	Models of particle production	30
1.3.1	HIJING	31
1.3.2	Semiclassical model	33
2	Experimental Setup	35
2.1	The Relativistic Heavy Ion Collider	36
2.2	The PHOBOS detector	39
2.2.1	Trigger detectors	41
2.2.2	Multiplicity array	43
2.3	Front-End-Electronics for silicon detector readout	45
2.3.1	Front-end chips	46
2.3.2	Hybrids	47
2.3.3	Front-End Controllers	47
2.3.4	Data Concentrator	51
2.3.5	Data Acquisition	52
3	Data Analysis	57
3.1	Signal processing from Silicon detectors: ADC to keV	57
3.1.1	Pedestal and noise calculation	59
3.1.2	Common mode shifts	61
3.1.3	Gain Calibration	62
3.2	Quality assurance: comparison with detector simulations	64

3.2.1	Silicon detector simulation	65
3.2.2	Trigger detector simulation	68
4	Event selection and Centrality determination	71
4.1	Minimum bias trigger	71
4.1.1	Offline cuts	74
4.2	Centrality determination	76
4.2.1	Trigger efficiency and the ‘missing’ cross section	78
4.2.2	Determination of $\langle N_{part} \rangle$ and error analysis	79
4.3	Vertex reconstruction and selection	82
5	Determination of charged particle multiplicity	85
5.1	Hit Merging	86
5.1.1	Determination of δE_{minhit}^{oct}	88
5.1.2	Determination of $\delta E_{minmerge}^{oct}$, $\delta E_{maxmerge}^{oct}$	88
5.1.3	Determination of δE_{noise}^{oct} , δE_{noise}^{rings}	91
5.2	Correction for geometrical acceptance	91
5.2.1	Identifying and correcting for non-functional pads	93
5.3	Correction for high occupancy in multiplicity detector	94
5.3.1	Correction based on Poisson statistics	95
5.3.2	Correction based on shape of energy loss distribution	96
5.4	Correction for hits from secondary particles	99
5.5	Summary of applied corrections	102
6	Results and Conclusions	103
6.1	Results	104
6.1.1	Pseudo-rapidity distributions of charged particles	104
6.1.2	Fragmentation region	108
6.1.3	Central rapidity region	112
6.1.4	Total N_{ch}	114
6.2	Systematic Checks	116
6.2.1	Detector effects	117
6.2.2	Occupancy effects	120

6.2.3	Secondary particles and Decays	120
6.2.4	Summary of systematic errors	122
6.3	Comparison with models	123
6.3.1	HIJING	123
6.3.2	Two component fit: Hard versus soft processes	125
6.3.3	Semi-classical QCD dynamics	127
6.4	Conclusions	129
A	The QCD Phase diagram	131
A.1	Chiral symmetry	131
A.1.1	Spin and its relation to the mass of a particle	133
A.1.2	Quark interactions and isospin	135
A.2	QCD phase diagram	137
B	Response of silicon detectors and electronics	141
B.1	Equivalent noise model for single preamplifier channel	141
B.2	Landau distribution of charged particle's energy loss	143
B.3	Convolution of multiple Landau distributions	145
C	Comparison of different MC simulations	149

Chapter 1

Introduction

The history of physics delineates an obsession with attempts to explain everyday phenomena using fundamental building blocks that respond to universal laws. The earliest Western notion that all matter is composed of atoms goes back to Greco–Roman times. Thomson’s experimental discovery of the electron and Rutherford’s interpretation of experiments with α –particles scattering from gold foils to reveal a hard nucleus at the core of the atom mark important milestones in our modern understanding of the structure of matter. From a theoretical perspective, Maxwell’s presentation of electrodynamics as a field theory[1], melded with the development of quantum mechanics in the first half of the 20th century, gave birth to Quantum Electrodynamics (QED): a theory that employs local gauge symmetry to calculate the interactions between charged particles with the utmost accuracy verifiable by experiments.

The picture of atoms composed of electrons orbiting in quantized levels around a stable nucleus, that could be split to release protons and neutrons (and a great deal of energy!) was a nearly complete one within QED. But first signs that protons and neutrons were *not* point particles were already apparent from the early days of QED: one of its major triumphs was the explanation of the electron’s magnetic moment. The Dirac equation predicts it to be:

$$\vec{\mu} = g \frac{e}{m} \vec{S}$$

with $g = 2$, where classically, we would expect $g = 1$ for a point–like particle. By the same token however, the measured magnetic moments of the proton and neutron ($g_p = 5.585$ [2], and $g_n = -3.826$ [3]) differ greatly from their QED predicted value.

R. Hofstadter's experiments[4] in the 1950's with elastically scattering electrons off protons and neutrons gave a clear indication that the latter were composite objects of finite size. With the rapid discovery of many new heavy particle resonances in the 1960s, it became increasingly apparent that the proton and neutron were just two 'animals' in a multifaceted 'zoo' of particles.

The quark model of Gell-Mann[5] and Zweig[6], proposed in 1964, attempted to bring order to the particle zoo. The motivation was to exploit the symmetric patterns into which the observed resonances of the proton, neutron and the π -meson seemed to fit, by postulating that all the baryon resonances contained three fractionally charged spin- $\frac{1}{2}$ quarks and the meson resonances, a spin- $\frac{1}{2}$ quark+antiquark pair. Quarks were arranged in 'flavor' families, of which we now know there six: up (u), charm (c), top (t) with charge $+\frac{2}{3}e$ and down (d), strange (s), bottom (b) with charge $-\frac{1}{3}e$. Although the quark model accommodated these symmetries elegantly, there was a residual suspicion about the real existence of such fractionally charged quarks and especially about their dynamics. The model had predictive power since it could point experiments to look for new particle resonances at specific energies that fit into the symmetry scheme (the Ω^- resonance discovered at BNL[7] in 1963 is a good example).

The existence of the Δ^{++} resonance[8] presented a problem for the constituent quark model, since its quantum numbers seemed to indicate that it contained three u quarks all in the same spin $+\frac{1}{2}$ state, in violation of Pauli's exclusion principle. Nambu[9] and Greenberg[10] introduced the idea of an extra degree of freedom called *color* possessed by the quarks. In addition to solving the statistics problem, Nambu[11] obtained a simple explanation of quark three-color dynamics as the cause of qqq and $q\bar{q}$ being the lowest stable hadronic states (as opposed to qq , $qqqqqq$, $q\bar{q}q\bar{q}$ etc). In 1969, experiments performed by Kendall, Friedman and Taylor[12] at the Stanford Linear Accelerator on deep inelastic scattering of electrons from nucleons confirmed that the nucleons were indeed composed of spin- $\frac{1}{2}$ point-like particles. At high transverse energies of the scattered electrons, the cross section was observed to be many orders of magnitude higher than the exponential fall-off expected from a 'diffuse' nucleon, indicating hard scattering from point-like constituents. The measured angular distribution of the scattered electrons exhibited a remarkable resemblance to the $\sin^4(\frac{\theta}{2})$ dependence observed by Rutherford fifty years earlier in discovering a point-like *nucleus* at the core of the atom.

The theory of quark color dynamics, or Quantum Chromodynamics (QCD) was proposed in the early 1970's in independent papers by Fritzsch, Gell-Mann and Leutwyler[13] and Weinberg[14]. They essentially adopted the recently successful Yang-Mills¹ field theory, as used in $SU(2) \times U(1)$ electroweak gauge theory, and applied it to the $SU(3)$ color gauge group. Quarks were postulated to interact with each other via the exchange of *gluons*, massless vector bosons belonging to the octet representation of $SU(3)$. In contrast to photons which are the chargeless, massless gauge bosons of QED, the Yang-Mills Lagrangian allows gluons to carry color and interact among themselves. Various aspects of QCD have been experimentally tested over the years. The discovery of the J/ψ and ψ' resonances in 1974 was followed by many experiments to determine the evolution of the ratio of hadronic to electromagnetic cross sections:

$$R = \frac{\sigma(e^+e^- \rightarrow \text{hadrons})}{\sigma(e^+e^- \rightarrow \mu^+\mu^-)}$$

which QCD predicts in detail from the number of quark color and flavor degrees of freedom. The observation of two and three jet events, first in e^+e^- collisions and later in $p + \bar{p}$ collisions, provided firm evidence of the existence of quarks and gluons. The verification of jet cross sections calculated in perturbative QCD led to the acceptance of what is now called the Standard Model of particle physics.

A profound aspect of QCD, stemming from its non-Abelian gauge dynamics, is the concept of 'asymptotic freedom', uncovered by Gross, Wilczek[16] and Politzer[17] in their seminal papers on color-charge renormalization of QCD: the strength of the color force changes with distance in such a way that it is strong at long distances (low energies) and becomes weak at short distances (high energies). The behavior is analogous to the Debye screening of electric charge in QED: an electron's bare electric charge is screened by a cloud

¹The celebrated Yang-Mills Lagrangian[15]

$$\mathcal{L}_{YM} = -\frac{1}{4}F_{\mu\nu}^a F^{\mu\nu a}$$

generalising local gauge invariance to the non-Abelian gauge group $SU(2)$, had been written down much earlier in 1954. The original motivation was to identify ρ -mesons as massless, self-interacting vector particles mediating the strong interaction. When that failed, Feynman, among others, continued to pursue the mathematics of Yang-Mills fields, since the nonlinear self-interactions of gauge bosons offered hope of a quantum theory of gravity. This led to many important advances in the theoretical understanding of Yang-Mills fields, for example the ghost method developed by Faddeev and Popov, which ultimately found application in QCD.

of electron–positron pairs surrounding it such that from longer distances, the renormalized apparent charge is smaller than the bare charge (Fig. 1-1a,b). For a bare quark, the screening cloud is composed of not only quark–antiquark pairs, but also self–interacting gluons that carry color charge (Fig. 1-1c,d). The latter produce an anti–screening effect that overwhelms the normal screening as long as the number of quark flavors is less than 16. As a result, the renormalized color charge in QCD is *larger* when probed at longer distances.

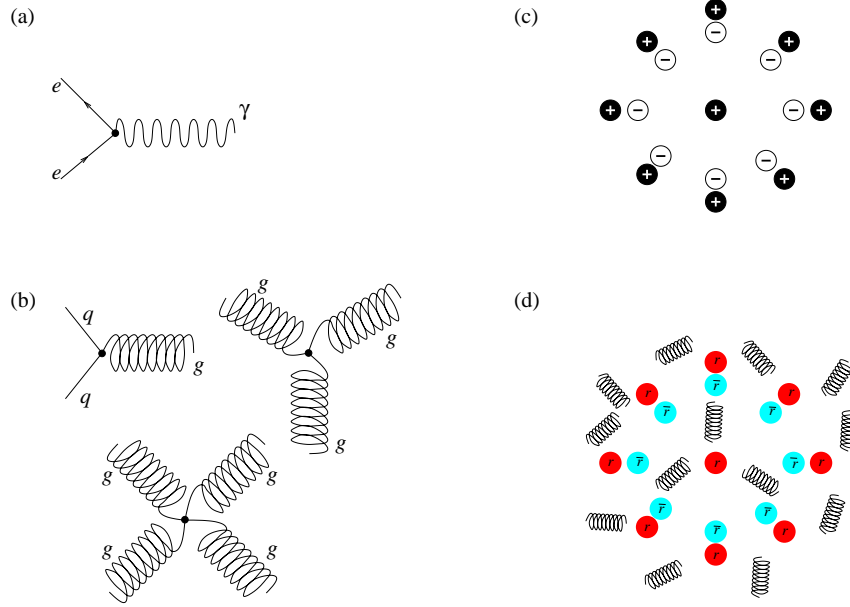


Figure 1-1: Basic Feynman diagrams allowed in QED(a) and QCD(b). Screening behaviour of bare charge in QED(c) and anti–screening in QCD(d)

The QCD Lagrangian density can be written as:

$$\mathcal{L}_{QCD} = -\frac{1}{4}G_{\mu\nu}^a G^{\mu\nu a} + \sum_j^{N_f} \bar{q}_j (i\gamma^\mu \nabla_\mu - m_j) q_j + \frac{\Theta}{16\pi^2} G_{\mu\nu}^a \tilde{G}^{\mu\nu a} \quad (1.1)$$

where q_i are the quark fields of mass m_i and flavor i . $G_{\mu\nu}^a$ (with dual $\tilde{G}^{\mu\nu a}$) is the gluon strength tensor expressed in terms of the 8 gluon fields A_μ^a ; ($a = 1..8$):

$$G_{\mu\nu}^a = \partial_\mu A_\nu^a - \partial_\nu A_\mu^a - gf_{abc} A_\mu^b A_\nu^c \quad (1.2)$$

∇_μ is the gauge-covariant derivative:

$$\nabla_\mu = \partial_\mu + igA_\mu^a \frac{\lambda_a}{2} \quad (1.3)$$

λ_a are the SU(3) Gell-Mann matrices, and f_{abc} are structure constants of the SU(3) group. Non-zero values of the structure constants f_{abc} cause quartic and trinomial non-Abelian gluon self-interaction terms to appear in the Lagrangian Eqn. (1.1). The last term in Eqn. (1.1), whose magnitude depends on the *a priori* unknown parameter Θ , is included only because it is allowed by the symmetries of the Lagrangian. It does not determine the classical (*i.e.*, observable dynamics) of the theory, but does affect the quantum dynamics through hypothesized particles called ‘axions’. Θ is believed to be very close to zero based on many indirect experimental hints[18, 19, 20].

The QCD running coupling constant $\alpha_s \equiv g^2/4\pi$ determines the strong interaction dynamics in Eqn. (1.1). Applying the renormalization technique to calculate α_s , Gross and Wilczek[21] obtained, to second order in perturbation theory:

$$\alpha_s(Q^2) = \frac{12\pi}{(33 - 2N_f)\log\left(\frac{Q^2}{\Lambda_{QCD}^2}\right)} \quad (1.4)$$

By using renormalization, the formal infinities in the ‘bare’ coupling constant caused by infinite momentum contributions from virtual particles are traded for a finite observable coupling constant.

Given an assumed value of the coupling at a specific momentum transfer Q^2 between the interacting particles (usually taken as $Q^2 = M_Z^2$, the mass of the Z boson), Eqn. (1.4) describes the ‘running’ of $\alpha_s(Q^2)$ with Q^2 . $\Lambda_{QCD} \sim 0.1-0.5$ GeV is a cut-off parameter that determines the momentum scale down to which the perturbative calculation holds.

For Q^2 much higher than Λ_{QCD}^2 , or equivalently, inter-particle distances less than ~ 1 fm, $\alpha_s(Q^2)$ exhibits a logarithmically falling dependence on Q^2 that has been experimentally verified by many techniques as summarized in Fig. 1-2.

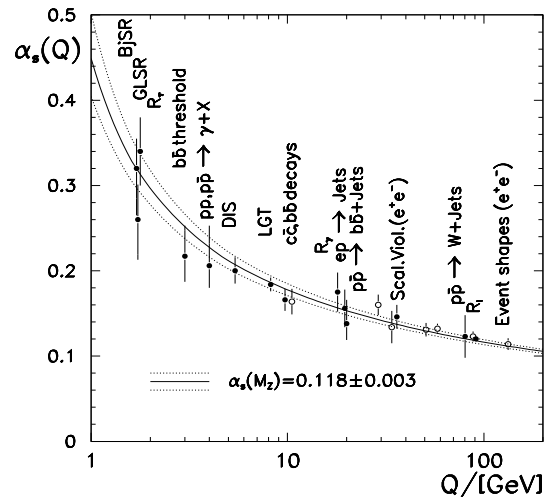


Figure 1-2: Summary[22] of experimental determinations of $\alpha_s(Q^2)$. The dashed line is the second-order perturbative QCD calculation

Two remarkable features of the strong coupling constant are apparent from Fig. 1-2:

Asymptotic Freedom: For inter-particle distances approaching zero, (equivalent to Q^2 being asymptotically large), the strong coupling $\alpha_s(Q^2)$ asymptotically approaches a very small value, i.e. it becomes ‘weak’. At small distances, the force between quarks as measured by α_s becomes very weak, and the quarks become ‘asymptotically free’. An important consequence of such asymptotic freedom is apparent in the Q^2 domain: the contributions from higher order loop diagrams to the perturbative calculation of α_s become asymptotically small, and even though the number of such diagrams increases, the calculation converges quickly [23, 24], as evidenced by the excellent agreement of experiment and theory for large Q^2 in Fig. 1-2. At large Q^2 , most particles emerging from a QCD interaction do so in the form of jets, whose cross sections can be computed with great precision. For example, the ratio of two-jet events, originated by a single $q + \bar{q}$ pair, to three-jet events, involving a gluon in addition to $q + \bar{q}$, is directly related to α_s , since the probability of initial gluon emission at the $q \rightarrow q + g$ vertex involves a single power of α_s . At large Q^2 , higher order perturbative corrections to this ratio are small, and it provides a direct measurement of α_s , among the best in Fig. 1-2.

Confinement: Asymptotic freedom provides a very simple description of how quarks and gluons interact over distance scales less than ~ 1 fm, *i.e.*, as long as they are *inside* a nucleon of size ~ 1 fm. However, as Q^2 decreases down to Λ_{QCD}^2 , $\alpha_s(Q^2)$ becomes of order 1, and the perturbative calculation that leads to the result in Eqn. (1.4) breaks down. Some physical insight can be gained by considering the extreme $Q^2 \rightarrow 0$ limit: in a model developed by Schwinger[25], Bjorken[26] and Casher *et al*[27], the color potential between a $q + \bar{q}$ at rest with respect to each other can be written as:

$$V(r) = -\frac{A(r)}{r} + K \cdot r$$

The first term is the normal Coulomb-like² force which gives rise to the dipolar lines of force as in the case of QED (Fig. 1-4a), and close to the quarks in QCD (Fig. 1-4b). For large r , the second term takes over, implying that the $q + \bar{q}$ potential rises linearly with separation, and that the force remains constant. The lines of force are therefore confined in

² Due to renormalisation, the co-efficient A is not a constant as in the pure Coulomb case, but has an r -dependence: $A(r) \sim 1/\ln(r^{-1})$. For small r , where the Coulomb term is important in this equation, A can be taken as constant.

a flux tube between the quarks. Within the flux tube, the field strength is roughly uniform and the energy of the system is proportional to the length of the flux tube. This implies that the energy cost of separating the $q + \bar{q}$ pair completely is infinite. However, when the energy stored in the flux tube exceeds twice the rest energy of a quark, a new $q + \bar{q}$ pair is produced, with the new particles acting as source or sink for the flux lines.

Although the Schwinger model provides an intuitive picture, it is hard to quantify. Some reference can be made to the trapping of magnetic flux in a tube inside a superconductor, the *Meissner* effect in condensed matter physics[28], but rigorously explaining the color confinement of massive quarks in QCD remains an unsolved problem³.

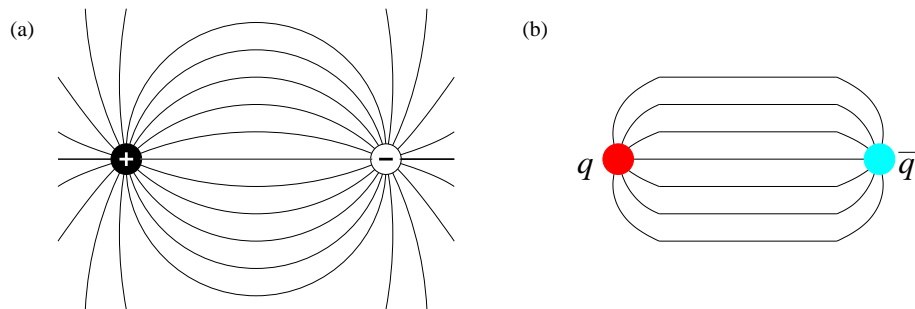


Figure 1-4: Lines of force between (a) e^+e^- pair in QED and (b) $q + \bar{q}$ pair in QCD.

In summary, the concept of asymptotic freedom is mathematically manifest in the running of the renormalized coupling, but the *mechanism* through which confinement is achieved in nature is not fully understood yet. Free colored quarks and gluons have never been observed in experiments since all hadrons are color-less. High energy hadronic collisions can be studied in QCD using quarks and gluons as the primary degrees of freedom, but the final observables in the laboratory are jets of composite hadrons originating, presumably, from the struck quarks and radiated gluons. ‘Hadronization’, or the process by which the leading high momentum quark leaves behind a trail of $q\bar{q}$ pairs, is modelled by fragmentation functions understood only up to a phenomenological level[31]. For example,

³

Perhaps the greatest hope is held out by t’Hooft’s conjecture[29] that in the limit of large N_c (number of colors), only planar Feynman diagrams contribute to quark loops; the large number of such diagrams fill up the hole in the center of the quark loop and provide the content of the flux tube between the q and \bar{q} . This idea naturally leads to connections with string theory since the quark loop can be regarded as the boundary of a D-brane[30], but discussion of D-branes is beyond the scope of this thesis.

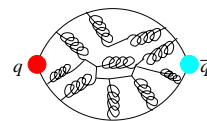


Figure 1-3: t’Hooft’s conjecture for large N_c

the distribution of quantum numbers of the leading quark into the many hadrons constituting a jet remains an unknown quantity. Structure functions describing the momentum composition of hadrons cannot be written down from first principles in QCD[32], nor can questions about their spin composition be answered easily at present.

With this brief introduction to the puzzling feature of confinement exhibited by QCD, the motivation to understand the puzzle by creating a *deconfined* phase of QCD becomes apparent. As pointed out at the beginning, a reductionist point of view forces us to look for the smallest building blocks of nature: the Standard Model indicates that quarks and gluons (along with the leptons and photon) are these ultimate blocks, and yet seems to ‘hide’ away the quarks and gluons inside hadrons through confinement.

1.1 Motivation for colliding heavy ions

In the early days of the quark model and QCD, there were many experimental attempts made to observe quarks in isolation, based on the naïve assumption that it should be possible to ‘ionize’ hadrons and liberate their constituents at high enough energies. Accelerator based isolated quark searches using hadron beams of energies up to 1.8 TeV failed to yield a positive result[33], as did Fairbank and Morpugo’s early experiments[34, 35] to use the equivalent of Millikan’s oil drops to measure the fractional charge of quarks. As the concept of confinement in QCD gained widespread understanding, the failures of such direct searches for free quarks could be placed in context[36].

The idea that relativistic heavy ion collisions may shed some light on the nature of QCD in the low- Q^2 , large distance, confinement regime is nearly as old as QCD itself[37, 38, 39]. An open question in astrophysics at the time was the nature of extremely dense neutron star cores, which had been deduced from astronomical observations to have a central matter density $\sim 10^{16} \text{ g} \cdot \text{cm}^{-3}$ [40, 41], very much in excess of nucleon matter density $8 \times 10^{14} \text{ g} \cdot \text{cm}^{-3}$. Neutron stars are created at a stage when gravitational collapse has forced protons to recombine with electrons, producing an extremely dense gas of neutrons, held stable by the repulsive Fermi degeneracy pressure balancing the attractive gravitational force.

Collins and Perry[37] suggested that matter at such high densities is a ‘quark soup’: the neutrons overlap and their identity becomes confused. In such a system, long range

interactions are screened because of many-body effects, and hence the troublesome long-distance features of the strong interaction can be ignored. A transition occurs from a rarified hadronic gas phase with confined quarks, to a dense phase in which the long distance interaction is screened by the presence of many quarks and gluons, and the quarks are therefore allowed to move freely outside the confining boundary of hadrons. This is similar to the formation of an electromagnetic ‘plasma’ in a dense ionized gas of electrons and nuclei.

In classical electrodynamics, a plasma is defined as a phase in which the Debye screening length (λ_D) in a gas is much smaller than the volume of the the gas, leading to the screening of Coulomb force between isolated charges and collective unrestricted motion of positive and negative charges in the gas. The Coulomb potential is modified from $V(r) = -\frac{C}{r}$ to $V(r) = -\frac{C}{r}e^{-r/\lambda_D}$; the potential is heavily screened for $r \gg \lambda_D$. In the case of superdense QCD, the many-body effects caused by the high density of quarks and gluons effectively provide an infrared (*i.e.*, long distance) cut-off to the renormalized strong interaction, thus providing an effective Debye screening[42].

Since distant neutron stars are not quite amenable to experimental probing, we look for alternative ways of creating very high density matter. In the context of *relativistic* many-body physics, increasing the *temperature* of a hadron gas is *analogous* to increasing its density. Since temperature is a measure of the frequency of interactions in a gas and the energy available for the particles to interact, higher temperatures cause more particles to be generated through pair production. For QCD, the self-interacting gluons enhance this effect and cause the density of the system to increase even further at high temperatures. In the laboratory, a possible method of creating such excited nuclear matter at high temperature is to collide two heavy nuclei at high center of mass energy per participating nucleon $\sqrt{s_{NN}}$ ⁴.

The nuclei have to be accelerated to very high energies (the earliest collisions were at $\sqrt{s_{NN}} = 1$ GeV; modern accelerators go up to $\sqrt{s_{NN}} = 200$ GeV) to ensure that the participating nucleons each have enough energy to cause pair production, *i.e.*, roughly in excess of twice the π mass, since most of the produced particles are π mesons. At the same time, the nuclei also have to be of large A , to ensure that the produced particles have time

⁴The definition of $\sqrt{s_{NN}}$ as the center-of-mass energy of a two-nucleus collision system divided by the total maximum number of participating nucleons is true for a symmetrical collider system like RHIC, but not necessarily true for fixed-target or asymmetrical collisions. We will use this term frequently in the rest of this thesis, with appropriate conversion applied for the latter case.

to thermally equilibrate. The magnitude of A required can be estimated as follows. The total cross section for $p + p \rightarrow n\pi$ is ~ 30 mb at these energies, which gives an equilibration time of 6×10^{-34} sec. The total time available for meson production is the time over which the two nuclei overlap: $0.2R/c_s$ where $R \sim (1.2 \times 10^{-15} m) \cdot A^{1/3}$ is the nuclear radius, the factor 0.2 is used since half the mass of a uniformly dense nucleus is contained within $0.2R$ of its surface. c_s is the speed of sound, $\sim \sqrt{\frac{1}{3}}c$ for an ‘ideal’ gas of nucleons and pions at a temperature of 140 MeV. This implies[38] that the disassembly time is long enough to allow thermal equilibrium to be achieved, if $A \gtrsim 50$.

It is important to note that while long-range interactions are screened in the quark gluon plasma at high temperatures (*i.e.*, the running coupling $g(T) \ll 1$, where T is the temperature), it *does not* imply that the interactions can be treated perturbatively. This can be simply understood by using the analogy of a simple harmonic oscillator in quantum mechanics: consider a slightly anharmonic oscillator with potential energy of the form:

$$V(x) \sim \omega_0^2 x^2 + g^2 x^4 \quad (1.5)$$

Even if the anharmonic g^2 term is very small, its effect becomes non-perturbative for $\omega_0^2 \rightarrow 0$, *i.e.*, the low-momentum or long wavelength modes of a hot QCD plasma cause non-perturbative effects that cannot be calculated analytically. To put this in context with the earlier discussion of deconfinement, the confining process in QCD ensures that *dynamically* generated color fields (the equivalent of electromagnetic fields) are confined inside the flux tube between a $q + \bar{q}$ pair. However, *static* magnetic fields are not confined, as in the case of QED plasmas. The sun, for example, produces a static magnetic field spanning the solar system, while any electromagnetic field generated within the sun’s plasma due to the presence of free charges is immediately expelled by the collective movement of those charges. It is such unscreened static magnetic fields that give rise to non-perturbative effects in the weakly interacting QCD plasma.

To obtain further quantitative insight into the non-perturbative behaviour of QCD in such a many-body system at large temperatures, a technique called *lattice QCD*[43] is used to numerically simulate the interactions on a discretized lattice of space-time points. The grand canonical partition function Z is the quantity of interest, and the volume V , temperature T and baryo-chemical potential μ_B are the control parameters on which Z depends.

The numerical evaluation of Z involves counting the number of microstates available to a system of quarks and gluons in going from an initial state $|i\rangle$ to a final state $\langle f|$, using the appropriate Lagrangian weight for each micro-state. This is equivalent to evaluating the path integral functional $\langle f|Z|i\rangle$ in quantum field theory, with the time variable (it) replaced by the temperature parameter $\beta \equiv 1/k_B T$. Contributions from small t , high frequency modes correspond to high temperature effects in a weakly interacting ‘quark soup’. Due to the necessity of having only real-valued contributions in a probabilistic sum, lattice calculations are difficult to perform for a system that is rich in baryons, *i.e.*, has $\mu_B \neq 0$ [44].

Numerical calculation of Z in lattice QCD provides direct information on the equation of state for QCD, since

$$\frac{PV}{k_B T} = \ln Z = \langle n \rangle$$

in the grand canonical ensemble, where $\langle n \rangle$ is the number of degrees of freedom available. A striking result of this calculation is shown in Fig. 1-5: the pressure P in a quark-gluon system undergoes a sharp rise at critical temperature $T_c = 180$ MeV. Such a rise can be understood as a *phase transition* from a weakly interacting hadron gas to a deconfined plasma of quarks and gluons. While the order of the transition depends on the number of light quark flavors used, the vast difference between the $T \ll T_c$ and the $T \gg T_c$ phases is clear.

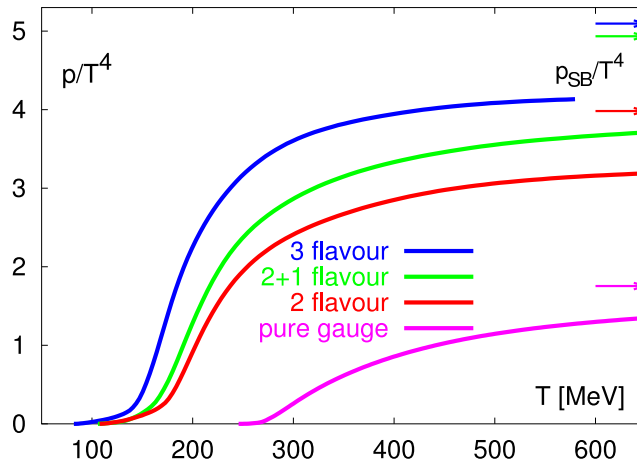


Figure 1-5: Numerical calculation[44] of pressure P/T^4 variation with temperature T . A phase transition is observed near $T_c = 180$ MeV for all the number of quark flavors considered.

Consider QCD at low temperatures with just u and d quarks, ignoring the heavier flavors. If there is no net concentration of baryons ($\mu_B = 0$), as assumed in the lattice

calculation, then the dominant degrees of freedom initially are the pions π^\pm, π^0 which carry zero baryon number and can be easily pair produced. Neglecting their rest mass and interactions, the pressure due to such an ‘ideal’ pion gas is given by the Stefan–Boltzmann blackbody radiation formula:

$$P_\pi = -\left.\frac{\partial Z}{\partial V}\right|_{T,\mu} = 3 \times \frac{\pi^2}{90} T^4 \quad (1.6)$$

where the factor 3 counts the number of pion charge states.

The equivalent expression for a plasma of free light quarks and massless gluons which are no longer confined within hadrons is much larger, since there are many more degrees of freedom, *i.e.*, *the plasma is a state of higher entropy*:

$$P_{q\bar{q}} = 2 \times 2 \times 3 \times \frac{7}{4} \times \frac{\pi^2}{90} T^4 ; P_g = 2 \times 8 \times \frac{\pi^2}{90} T^4 \quad (1.7)$$

In the $P_{q\bar{q}}$ contribution, there are 2 helicity states each, 2 flavor states (u and d), and 3 color states. The factor $\frac{7}{4}$ arises due to the Fermi–Dirac statistics of the quarks (the pion gas obeys Bose–Einstein statistics). For P_g there are 2 helicity states and 8 color states. The sum $P_{qgp} = P_{q\bar{q}} + P_g = \frac{37}{90}\pi^2 T^4$ represents the Stefan–Boltzmann limit for a non–interacting plasma. The values determined from lattice calculations for $T > T_c$ as shown in Fig. 1-5, after undergoing a sharp rise at T_c , fall below this ‘ideal gas’ limit, indicating that some degree of interactions persist in the plasma phase. These residual interactions are similar to van der Waal’s forces which modify the radiation formula for a real gas from its ideal Stefan–Boltzmann limit. In the plasma phase, this corresponds to the Debye screening length λ_D being small but non–zero. For QCD, $\lambda_D(T) \propto 1/T$, and Fig. 1-5 indicates[45] that for T not much greater than T_c , $\lambda_D \sim 0.1\text{fm}$.

A second important result from lattice QCD which shows a similar phase transition as a function of temperature, is the value of the chiral condensate $\langle\psi\bar{\psi}\rangle$, as shown in Fig. 1-6 (cf. Appendix A for a discussion on the role of chiral symmetry in the QCD Lagrangian, and its relation to the QCD phase diagram). Fig. 1-6 also shows the free energy function L , related to the free energy of an isolated quark $f_q(T)$ via $L \propto \exp(-f_q/T)$.

For $T < T_c$, the condensate $\langle\psi\bar{\psi}\rangle$ is large, signalling chiral symmetry breaking, and L is small, implying that the energy of an isolated color source charge diverges or equivalently, the energy cost of separating a $q\bar{q}$ pair approaches infinity. For $T > T_c$ the reverse behavior

is seen, indicating that both chiral symmetry is restored and color charges are no longer confined in the plasma phase.

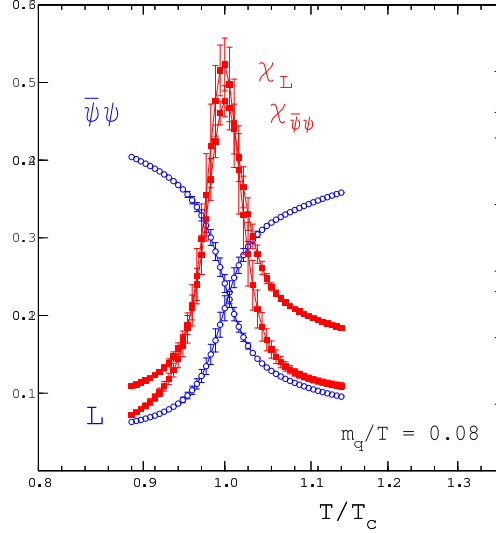


Figure 1-6: Chiral condensate $\langle\bar{\psi}\psi\rangle$ and quark free energy function $L(f_q(T))$ as a function of T in the neighbourhood of the phase transition, together with their associated susceptibilities[44].

Also shown in Fig. 1-6, are the associated susceptibilities defined as $\chi_L = \langle L^2 \rangle - \langle L \rangle^2$. These susceptibilities indicate how strongly thermodynamic observables fluctuate. As second derivatives of the free energy, they are found to peak or even diverge at the phase transition. The reason why these two *a priori* distinct phase transitions, signalled by peaks in χ_L and $\chi_{\langle\bar{\psi}\psi\rangle}$ occur at nearly the same temperature is not understood yet⁵.

These numerical results on the equation of state from lattice QCD calculations, supported by the general expectation of deconfinement in hot, dense matter from the QCD Lagrangian, provide the strongest motivation for studying particle production in heavy ion collisions. The aim is to study the phase of quark matter in the high temperature $T \gg T_c$ regime, as well as to determine the nature of the transition near $T \sim T_c$. The former is pursued in this thesis by measuring the total particle production in the collision; the latter study requires other order-parameter-like signatures involving observables that are not considered here.

⁵ It is important to emphasize that the behaviour of thermodynamic observables shown in Fig. 1-5 and Fig. 1-6, is the *result of numerical evaluation* of properties of the otherwise intractable QCD Lagrangian. At zero baryo-chemical potential $\mu_B = 0$, the lattice results can be rigorously shown to approach the continuum limit asymptotically, and are generally regarded as strong theoretical evidence of a QCD phase transition

1.2 Particle production in heavy ion collisions: Overview

The primary result of lattice QCD, from which the measurement presented here is motivated, is the enormous increase in the number of degrees of freedom in going from a dilute hadron gas phase at low temperature, to a dense quark gluon plasma at high temperature. Even though the ideal gas approximations used in Eqn. (1.6) and Eqn. (1.7) assume thermodynamic equilibrium, the fact remains that the increased entropy in a deconfined quark gluon medium, once produced, cannot be destroyed - even if the system does not evolve in equilibrium. As the temperature falls below T_c , the large entropy present in the colored plasma cannot survive as is, and must lead to production of colorless hadrons that is quantitatively different from what would have been produced by the collision of two hadronic systems without a phase transition.

Since we will be presenting measurements of particle production in heavy ion collisions and looking for a large increase in the number of particles produced, it is useful to first review what is known about hadronic particle production in smaller, simpler systems like hadron-hadron ($p + p$ and $p + \bar{p}$) and hadron-nucleus ($p + A$) collisions. By convention, the distribution of the produced particles in phase space is measured using two kinematic quantities that are both experimentally accessible and theoretically simple by virtue of being Lorentz invariant under longitudinal transformations:

- Rapidity $y \equiv \frac{1}{2} \ln \left(\frac{E+p_z}{E-p_z} \right)$, where E is the particle's energy and p_z is the longitudinal component of its momentum along the beam (\hat{z}) direction. The rapidity difference dy is boost invariant.
- Transverse momentum \vec{p}_T , a two dimensional vector quantity, whose differential element is usually taken as $2\pi p_T dp_T$

By measuring the momentum of the produced particles, and determining their mass (through spectroscopic identification) or their energy (through calorimetry), the phase space distribution can be determined in the form $\frac{1}{p_T} \frac{dN}{dy dp_T}$. As the number of produced particles increases, it becomes less practical to identify all of them experimentally. For $p_T^2 \gg m^2$ of

the particle⁶, the rapidity y can be simplified to a quantity called pseudo-rapidity η :

$$\eta = -\ln\left(\tan\frac{\theta}{2}\right)$$

which is much simpler to measure, since it involves only one kinematic variable θ , the angle of production with respect to the beam \hat{z} axis. The pseudo-rapidity η , unlike y , is not Lorentz invariant.

A second simplification necessitated by experimental limitations is that it is much easier to detect charged particles, than neutral particles, as the former deposit energy directly in detectors through ionization. Since hadronic interactions which are of interest here do not affect the electronic charge dynamics, it is fair to assume⁷ an equipartition of particles in the $+$, $-$ and 0 charge states, and hence measure just the charged particles. Some interesting effects may occur in event-by-event fluctuations of the ratio of neutral to charged particles due to chiral symmetry restoration[48], but for an *inclusive average* multiplicity measurement, it is safe to consider only the N_{ch} component in measuring $\frac{1}{p_T} \frac{dN_{ch}}{d\eta dp_T}$. With these preliminaries, we conduct a brief review of charged particle production in hadron-hadron, hadron-nucleus and nucleus-nucleus collisions.

Hadron-Hadron collisions

We consider first, $p + p$ and $p + \bar{p}$ collisions at high center of mass energy. There exists a wealth of data from experiments performed at the CERN ISR, CERN SPS and Sp \bar{p} S, DESY(Germany) and the FermiLab Tevatron colliders, which was the proving ground of many early QCD ideas. Fig. 1-7a shows the mean number of charged particles produced in $p + p$ and $p + \bar{p}$ collisions for beam energies ranging from 2 GeV to 2000 GeV. Up to thirty particles are produced in the higher energy range and most of the particles are released in the form of jets. For a collision of two protons at center of mass energy \sqrt{s} , the rapidity of each is $y_p = \pm \ln\sqrt{s}/m_p$. Fig. 1-7b shows the rapidity distribution of the produced charged particles.

⁶ An approximation easily applicable for pions, but not for protons. However, it can be shown[46] that the difference between distributions in η and y differ only by $\sim 10\%$ for values of y close to zero.

⁷This follows from the isospin-conserving nature of the strong interaction[47]

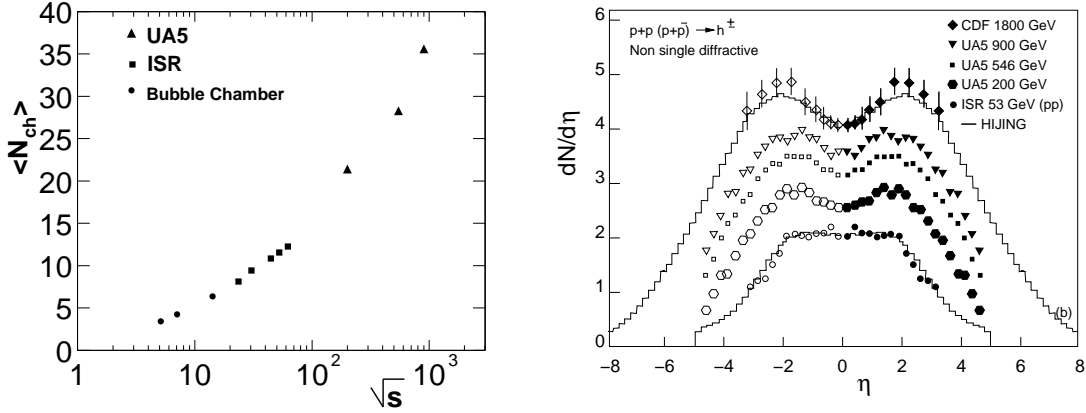


Figure 1-7: (a) Compilation[49] of mean number of charged particles $\langle N_{ch} \rangle$ as a function of $\sqrt{s_{NN}}$ in $p + p$ collisions. (b) $dN_{ch}/d\eta$ in $p + p$ and $p + \bar{p}$ collisions[49, 50]. Open symbols are reflection of the measured data points (closed symbols) around $\eta = 0$.

Based on early ideas in Feynman’s parton model of nucleons[51], one expects a rapidity plateau between the limiting values of $\pm y_p$, with the extent of the plateau increasing with increasing beam energy as $\pm y_p$ are pushed outwards. This expectation arises from considering the collision dynamics in the rest frame of a produced particle at (say) $y = 0$. In this frame, the two initial protons look identical approaching from opposite direction at velocities near the speed of light, and pass through each other so quickly that only their slowest constituents have time to interact and produce a particle–antiparticle pair at $y = 0$. By Lorentz invariance, the same is true for most other values of y between $+y_p$ and $-y_p$, until we get close to either end, where one proton looks quantitatively different from the other. This naturally leads to a rough separation of the pseudo-rapidity range into two regions: the ‘fragmentation region’ centered around $\pm y_p$, consisting of fragments arising mostly from the breakup of protons, and the ‘central rapidity’ region, characterized by a plateau shape whose extent increases with increasing \sqrt{s} .

The expectation of a rapidity plateau can be also quantified in terms of the momentum distribution of the constituent ‘partons’. Each parton carries a certain fraction ($\equiv x_F$) of the nucleon’s longitudinal momentum. Partons with low x_F are now generally identified with gluons[22] whose concentration, or structure function is expected to behave as $G(x) \propto 1/x$. The rapidity plateau in $p + p$ collisions is therefore expected as a result of scaling of the structure function. Particles at or near mid–rapidity are produced from ‘soft’ partons whose interactions have a finite range of 1 to 2 units of rapidity, and as the collision energy

increases, the concentration of these soft partons remains unaffected. Naïvely, we would expect the height of the plateau to remain constant with increasing \sqrt{s} , and the mean number of charged particles to increase linearly as $\sim 2y_p \sim \ln\sqrt{s}/m$. In reality, the measured $\langle n_{ch} \rangle$ (Fig. 1-7a) increases faster than $\ln\sqrt{s}$, and a rapidity plateau is not observed in the pseudo-rapidity distributions. This is due to violation of the scaling hypothesis[52]: the gluon structure function at small x rises somewhat faster than $1/x$, and the mid-rapidity yields are therefore dominated by increasing charged particle production from soft gluons.

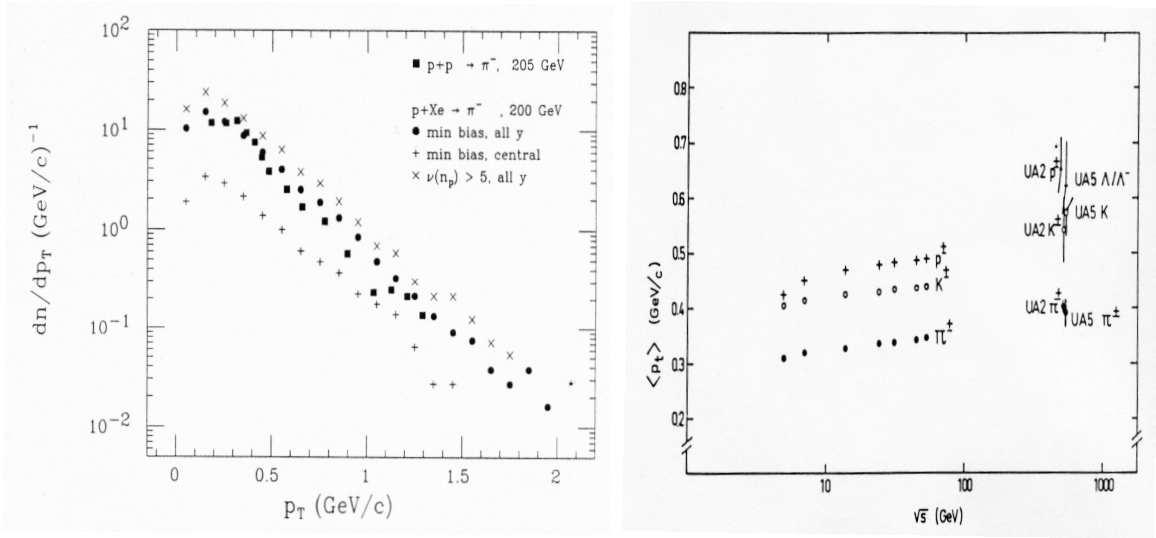


Figure 1-8: Compilation[53] of p_T distribution of π^- produced in $p+p$ and $p+A$ collisions.

A second feature of particles produced in $p+p$ collisions is exhibited by their transverse momentum (p_T) distribution. Although we will not be discussing it much in the rest of this thesis, it is remarkable to note that the transverse momentum of most of the identified particles (π , K , p) is described very well by a Boltzmann distribution, nearly independent of energy. This implies that even in a $p+p$ collision, the particles appear to be produced from a thermally equilibrated system: $\frac{1}{p_T} \frac{dN_{ch}}{dp_T} \sim e^{-\frac{p_T}{T}}$ with the inverse slope parameter T acting as an effective temperature. The mean $\langle p_T \rangle$ is measured to be ~ 350 MeV for π^- , and remains nearly constant over two orders of magnitude variation in the beam energy. The fitted slope $T \approx 180$ MeV corresponds to the temperature at which the π^- suffer their last interactions, as they leave the collision volume, but may also be interpreted as simple phase-space dominance[54].

Hadron–Nucleus collisions

Following the success of $p + p$ collisions in uncovering the basic features of QCD dynamics like jet formation, many hadron–nucleus collision experiments were performed using high energy π , K and p beams scattering on C , Au , Pb target foils with the primary purpose of understanding how hadrons lose energy in travelling through nuclear matter[55]. The measured pseudo-rapidity and rapidity distributions in hadron–nucleus collisions is shown in Fig. 1-9. For a direct comparison, the data from $p + p$ and $p + A$ collisions is also shown in cartoon form in Fig. 1-10 to highlight a few interesting features.

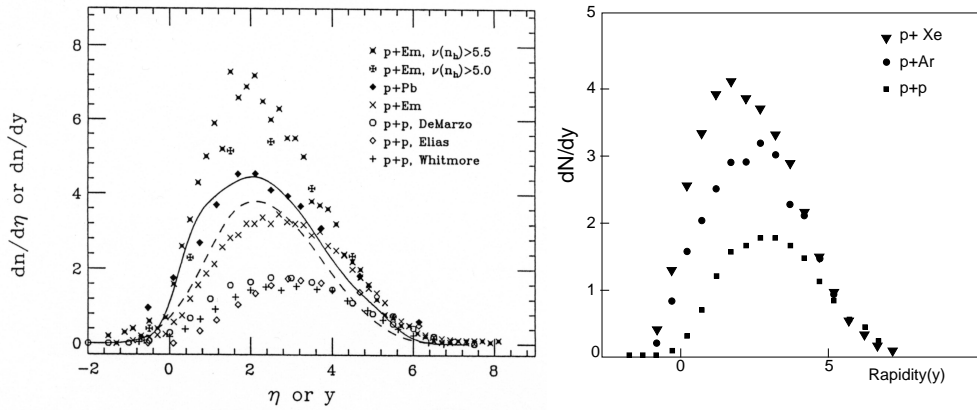


Figure 1-9: Compilation[53, 56] of pseudo-rapidity and rapidity distributions of charged particles in $p + A$ collisions. Data from $p + p$ collisions is also shown for comparison.

Above a threshold, the multiplicity in the projectile fragmentation region is found to be independent of the target identity A and the projectile’s energy. In the target fragmentation region it depends linearly on the target ‘thickness’, as measured by a parameter $\bar{\nu} = A\sigma_{hp}/\sigma_{hA}$, the mean number of collisions suffered by the hadron in traversing the nucleus. This phenomenon is called “limiting fragmentation” and was first predicted by Benecke *et al*[57].

In the central rapidity region, the multiplicity interpolates smoothly between the rising target fragmentation region and the constant projectile fragmentation region. Such a distribution can be understood using a “wounded nucleon model”[58] which assumes that as the fast-moving hadron projectile traverses the nucleus, it perturbs or excites nucleons along the way, and the wounded nucleons remain so, until they leave the interaction zone, wounding other nucleons along the way. The number of wounded nucleons is governed by the nuclear geometry, and their properties characterize particle production.

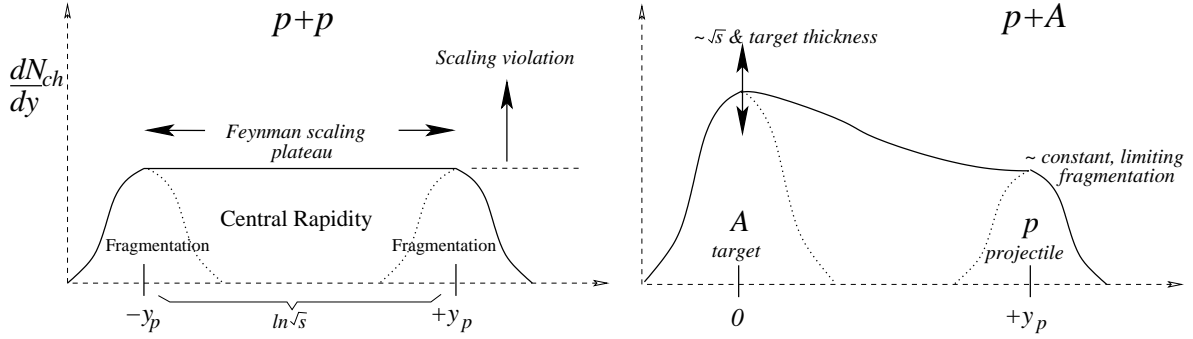


Figure 1-10: Schematic of multiplicity distributions observed in (a) $p + p$ and (b) $p + A$ collisions.

Two important concepts introduced in hadron–nucleus collisions that are new compared to $p + p$ collisions are the impact parameter and the hadron’s energy loss. The impact parameter b is defined as the perpendicular distance to the center of the target nucleus (Fig. 1-10). If the impact parameter is small, the hadron has to traverse a much bigger length inside the nucleus, than it would in striking the periphery of the nucleus. This implies a larger number of collisions $\bar{\nu}$, and an increase in the number of wounded nucleons. Thus, the multiplicity expected in different hadron–nucleus collisions varies depending on the impact parameter of the collision, and is not just a superposition of many independent $p + p$ collisions.

The second concept, extensively studied by Busza and Goldhaber[59], relates to the energy loss suffered by the projectile hadron, also referred to as the nuclear stopping power. The energy loss can be quantified in terms of the median *rapidity* loss of the projectile which was initially travelling at a rapidity y_p . Through extensive analysis of all the available $p + A$ data, they found under quite general conditions that, on average, protons traversing a nuclear medium lose two units of rapidity due to inelastic collisions with nuclear matter. The loss is somewhat dependent on the “thickness” of the nucleus, but the rapidity loss per unit length is constant. This implies that if we observe a $p + A$ collision at $\sqrt{s} \lesssim 4$ GeV in the center-of-mass system (corresponding to $y_{beam} \sim \pm 2$), most of the baryon number carried by the projectile proton is ‘stopped’ or brought to the $y = 0$ central rapidity region, where energy lost by the projectile can be used to produce particles. For higher center-of-mass energies $\sqrt{s} \gg 4$ GeV the proton’s energy loss is insufficient to bring enough baryon number density to $y = 0$, *i.e.*, the proton and nucleus are transparent to each other and particle production at $y = 0$ occurs purely through non–perturbative heating of the vacuum as the two pass through each other.

Nucleus–Nucleus collisions

A summary of charged particle multiplicity measurements from fixed target Au+Au collisions at the AGS accelerator (BNL, USA) and Pb+Pb collisions at the CERN SPS accelerator are shown in Fig. 1-11. At the AGS the center of mass energy went up to $\sqrt{s_{NN}} = 4.3$ GeV, while at the SPS $\sqrt{s_{NN}}$ went up to 17.2 GeV.

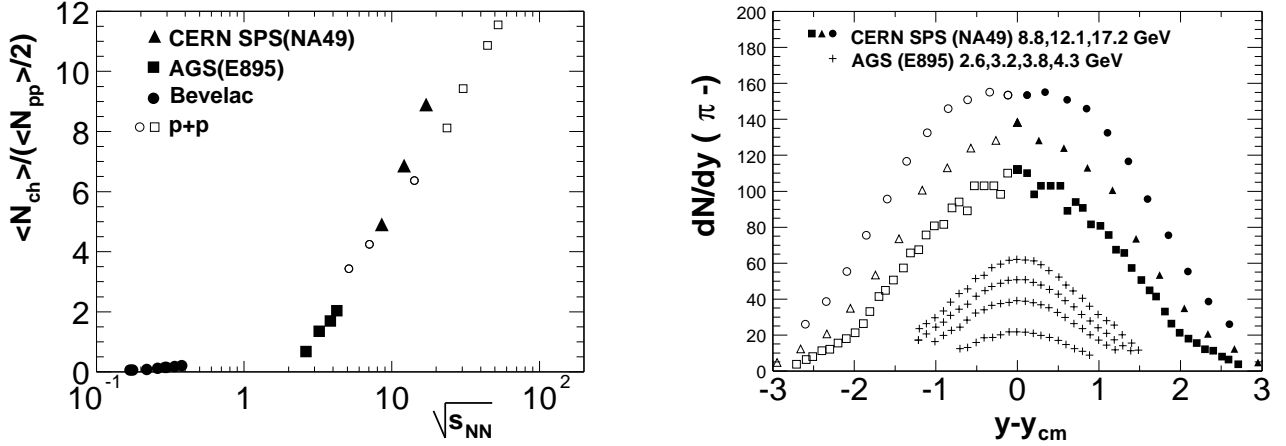


Figure 1-11: a) Mean number of charged particles per participant pair $\langle N_{ch} \rangle / (\langle N_{pp} \rangle / 2)$ as a function of $\sqrt{s_{NN}}$ in central A+A collisions. Data are from Bevelac[60], AGS[61] and SPS[62] experiments. p + p data are also shown as open symbols for comparison. b) dN/dy for π^- produced in central A + A collisions at AGS and SPS experiments[61, 62] for increasing values of $\sqrt{s_{NN}}$. For the NA49 results, open symbols represent data reflected about $y = 0$

Most of the qualitative features observed in hadron–nucleus collisions are carried over to nucleus–nucleus case. The total number of charged particles produced per participating pair of nucleons in central A + A collisions is independent of the mass number A of the nuclear species at a given $\sqrt{s_{NN}}$, but larger than in p + p collisions for $\sqrt{s_{NN}} \gtrsim 10$ GeV. The rapidity distribution of π^- produced in central A + A collisions which tracks the total $dN_{ch}/d\eta$ evolves smoothly as a function of $\sqrt{s_{NN}}$.

The physical picture of a heavy ion collision is depicted in Fig. 1-12. In the center of mass system, the two colliding nuclei appear as highly Lorentz contracted ‘pancakes’. The perpendicular distance between the center of the two nuclei, the impact parameter b determines the centrality of the collision. For a collision that is not head-on, only a part of the nuclei overlap in position space, and therefore only some of their nucleons will participate in the collision dynamics. These are called ‘partic-

ipants’. The remaining nucleons, called ‘spectators’ continue in the beam direction and eventually produce nuclear fragments. They can provide an excellent estimate of the impact parameter of a collision, by depositing energy in a calorimeter placed at 0° to the beam direction, traditionally called the Zero Degree Calorimeter (ZDC). The number of participating nucleons $N_{part} = A - N_{spec}$ provides a very important handle in characterizing $A + A$ collisions: at a fixed $\sqrt{s_{NN}}$, N_{part} varies monotonically with the centrality of the collision. For very central collisions, nearly all the nucleons participate, while for very peripheral collisions, N_{part} is fairly small. In a model due to Glauber[63], it is simple to estimate the number of binary collisions that these participants undergo, and from the discussion of $p + A$ data earlier, it is clear that the particle production must be a monotonic function of the number of such binary collisions.

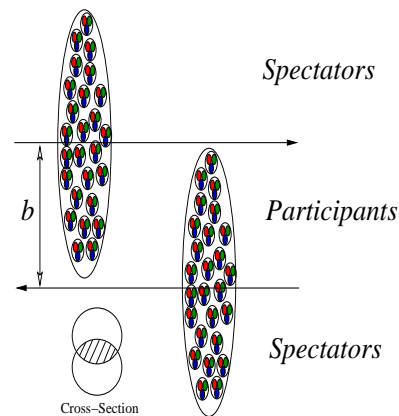


Figure 1-12: Schematic of an $A + A$ collision

This does not mean however, that the particle production process in heavy ion collisions is by any means simple! A few considerations that complicate things are:

1. There is of course the expectation from lattice QCD arguments developed earlier, that at high enough $\sqrt{s_{NN}}$, it is not just the nucleons that participate in the collision. Quark-gluon degrees of freedom are liberated, and it is these that govern the collision dynamics. The enormous amount of entropy liberated in the deconfinement phase transition makes for a much hotter ‘soup’ of interacting plasma, that attains thermal equilibrium quickly, and expands outward at relativistic speeds. The expansion is driven by the need to conserve entropy density as the colored system cools to a temperature T_c and hadronizes into colorless hadrons[64]. Naïvely, we expect the extra entropy in the colored phase to show up in an enhanced production of particles in the final state, primarily at mid-rapidity in both the nuclear stopping and transparency regimes where the highest baryon density and/or energy density is deposited. Not so naïvely[65], we expect at least the *partition* of extra entropy to affect the distribution of produced particles.

2. A second aspect of $A + A$ collisions, having nothing in common with $p + p$ and $p + A$ systems, is the *hydrodynamical* evolution of the collision volume. In a central Au+Au collision, there are approximately 340 participating nucleons and the system can be treated

using statistical techniques. Thermodynamic quantities like the pressure P (cf Fig. 1-5) are relevant and can be directly estimated from experimental observables like ‘flow’[66]. Hydrodynamic flow arises in $A + A$ collisions due to the conversion of spatial anisotropy in the initial state (the almond shape of the collision volume in Fig. 1-12) into a momentum anisotropy: particles moving along the long axis of the elliptical almond suffer much more momentum degradation due to multiple collisions than the ones moving along its short axis. This can be measured[67] by a Fourier analysis of the azimuthal charged particle distribution $dN_{ch}/d\phi$.

3. In the event of the collision volume being composed mostly of a hot quark gluon plasma, there are many other physical effects that become feasible, and could be used to signal the onset of deconfinement and perhaps even study the properties of the deconfined medium. An explosive growth in the charged particle multiplicity has already been mentioned as a possible signature of the former. Another possible effect is the inability of $c\bar{c}$ pairs to bind together in a densely colored medium leading to a suppression of yield of J/ψ particles. Photons and lepton pairs produced in the plasma, being electromagnetic, would leave without interacting with the colored medium, and therefore provide clean probes of the plasma’s temperature. The reader is referred to [68] for a detailed review of many such signatures.

1.3 Models of particle production

To overcome the difficulty of quantitatively treating the multiparticle final state of heavy ion collisions, a number of phenomenological models have been developed[69]. They may be broadly classified into three groups, based on the different relevance given in each model to underlying QCD dynamics and degrees of freedom (quarks, ‘strings’, hadrons, classical fields) in the initial state:

1. ‘Soft’ or ‘Cascade’ models that emphasize soft (*i.e.*, low- Q^2) dynamics. Collisions are modelled using ‘strings’ – a phenomenological entity spanning two partons that mimics the interaction between them. String breaking leads to particle production in such models. Examples of this type are: RQMD[70], UrQMD[71], VENUS[72], NEXUS[73].
2. ‘Hard’ models that focus on the high- Q^2 perturbative dynamics, dominated by jet formation from high momentum partons. These hard partons are taken as the starting

point of expansion and eventual hadronization. HIJING[74], EKRT[75] are models of this type. Since the bulk of produced particles in heavy ion collisions are actually soft, these models usually add on a soft part for the hadronization step.

3. Thermal models[76] which treat the collision as a statistical system, using thermodynamic analysis to predict the ratios of different produced particle species. To get absolute quantities like the number of charged particles, extra input to these models is needed, like the total volume at freezeout.

A summary of predictions for the the charged particle pseudo-rapidity density at $\eta = 0$, in central Au+Au collisions at $\sqrt{s_{NN}} = 200$ GeV from a variety of models is shown in Fig. 1-13. The range of predictions varies by more than a factor of two. In the interest of brevity, only two models which make the least naïve assumptions of relevant dynamics will be discussed further in this thesis.

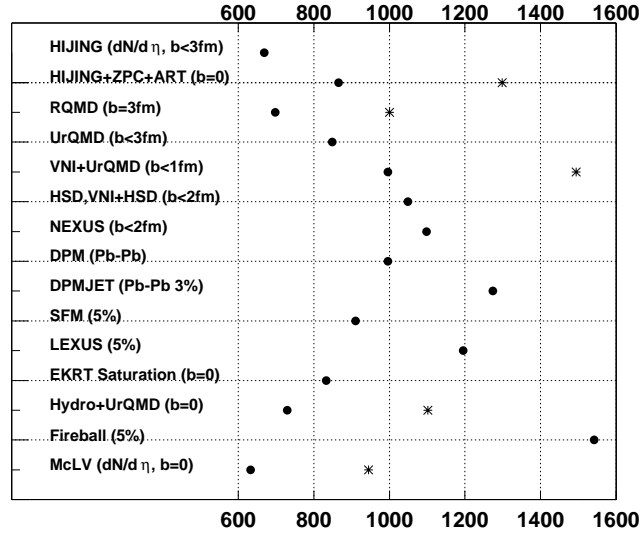


Figure 1-13: Model predictions for $dN_{ch}/d\eta$ at $\eta = 0$ in central Au+Au collisions at $\sqrt{s_{NN}} = 200$ GeV shown at the Quark Matter 2001 conference[77]. (*) represent predictions for N_{tot} provided by some models, which are then converted to N_{ch} (●) by applying a factor of 2/3.

1.3.1 HIJING

Heavy-Ion Jet Interaction Generator (HIJING) is a Monte Carlo simulation of the microscopic collision dynamics. It incorporates code from PYTHIA[78] to calculate hard scattering cross sections of partons in perturbative QCD upto leading order. This pro-

vides a starting point with the number of ‘mini’-jets per inelastic nucleon–nucleon collision. FRITIOF[79] string calculations are then added to model hadronization through non-perturbative soft collisions. A p_T cutoff (p_0) determines the distinction between the hard and soft regimes. Based on comparison with $p + \bar{p}$ data, a fixed cutoff of $p_0 = 2$ GeV is used, independent of A and centrality.

By default, HIJING tries to simulate physics as already known from extensive study of $p + \bar{p}$ collisions⁸. It therefore provides an important baseline of what we expect in heavy ion collisions, if they are merely a superposition of nucleon–nucleon collisions. There are some switches provided to turn on interesting effects that could possibly modify our expectations in a many-body environment. For example, the parton structure functions can be made impact parameter dependent (this is called ‘shadowing’). It is also possible to study the dependence of high p_T observables on energy loss per unit length (dE/dx) of high energy partons traversing the dense matter produced in the collision, in a phenomenon called ‘jet quenching’. Estimates indicate that dE/dx of mini-jets in a colored medium could be significantly higher than ordinary nuclear matter. A summary of charged particle pseudo-rapidity densities predicted by HIJING for various impact parameters at $\sqrt{s_{NN}} = 200$ GeV is shown in Fig. 1-14

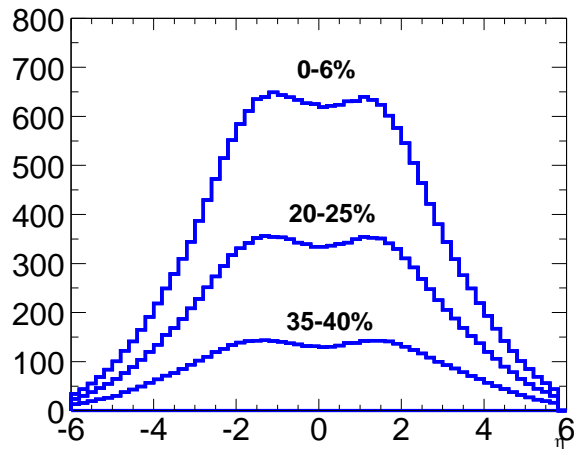


Figure 1-14: HIJING predictions for the pseudo-rapidity distribution $dN_{ch}/d\eta$ in Au+Au collisions at $\sqrt{s_{NN}} = 200$ GeV for different percentage selections of the total cross section. The top curve (0-6%) corresponds to most central collisions, with impact parameter $b < 3$ fm.

⁸PYTHIA and FRITIOF, the core components of HIJING, have been extensively tested against detailed $p + p$ and $p + \bar{p}$ data

1.3.2 Semiclassical model

In the physical picture of a heavy ion collision discussed in the previous section, it is possible to generate high parton densities by heating the vacuum in a nearly transparent collision of two heavy nuclei. A semi-classical description of the system is possible if the parton density becomes so high that it saturates the available phase space, and no new partons can be produced. Assuming that most of the partons are gluons, this saturation occurs when:

$$\frac{N_g(Q)}{\pi R_A^2} \times \sigma_g(Q) \gtrsim 1$$

where R_A is the nuclear radius and $\sigma_g(Q)$ is the gluon fusion cross section at a momentum transfer Q . $N_g(Q)$ is the number of interacting gluons. Gluons with a transverse momentum at or below Q_{sat} for which the above equality holds, saturate the phase space. Referring back to the analogy with a slightly anharmonic simple harmonic potential $V(x) \sim \omega_0^2 x^2 + g^2 x^4$, parton saturation corresponds to the limit of high energy where the system can probe large spatial x , leading to the anharmonic term becoming non-perturbative even for small g , and a semi-classical description of the oscillator dynamics becomes possible.

In a model of initial state saturation authored by Kharzeev and Nardi[80], the saturation occurs in the initial parton distributions, even before the nuclei collide. The colliding nuclei are highly Lorentz contracted, and most of the partons participating in the interaction are gluons, due to their large structure function. At small values of Bjorken x (fraction of longitudinal nucleon momentum carried by the parton), by uncertainty principle, the interaction develops over large longitudinal distances $z \sim 1/mx$ where m is the nucleon mass. When z becomes larger than the nuclear diameter, the interaction cannot distinguish between nucleons at the front and back edges of the nucleus, and all partons within a transverse area $\sim 1/Q^2$ determined by the momentum transfer Q participate *coherently* in the interaction.

Since the number of gluons $N_g(Q) \sim xG_A(x, Q^2)$ and the gluon fusion cross section $\sigma_g(Q^2)$ scales with α_s , the gluon *density*—which primarily determines the final charged particle multiplicity in this model, evolves with α_s at the saturation scale:

$$\frac{dN_{ch}}{d\eta} \propto \frac{dN_g}{d\eta} \sim \frac{S_A Q_s^2}{\alpha_s(Q_s^2)}$$

where S_A is the nuclear overlap area (πR_A^2 for central collisions, and an N_{part} determined fraction of it for non-central collisions). The saturation scale Q_s is determined from a detailed semi-classical QCD analysis. All the produced particles are assumed to evolve linearly from the saturated partons in the initial state, no provision is made for final state particle production; so the results need to be normalised against a measured value of $dN_{ch}/d\eta$ to obtain the proportionality constant in the above equation. The prediction of this simple model for the pseudo-rapidity distribution of charged particles at various values of impact parameters for Au+Au collisions at $\sqrt{s_{NN}} = 200$ GeV are shown in Fig. 1-15.

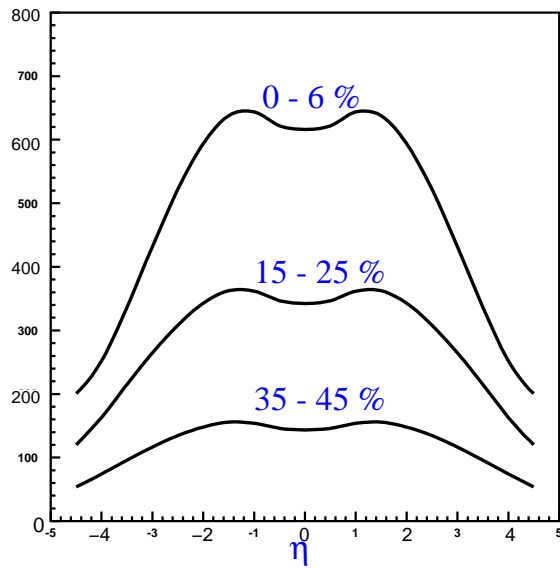


Figure 1-15: Predictions for the pseudo-rapidity distribution $dN_{ch}/d\eta$ in Au+Au collisions at $\sqrt{s_{NN}} = 200$ GeV for different impact parameters from the semiclassical initial state saturation model of Kharzeev et al[80]

After this brief introduction to the basic physical processes expected to occur in relativistic heavy ion collisions, the rest of this thesis will focus on a relatively straightforward measurement of the number of charged particles produced: specifically, their distribution in pseudo-rapidity as a function of centrality and center-of-mass energy of the collision. A dramatic increase of charged particle multiplicity over that expected from hadron-hadron, hadron-nucleus and nucleus-nucleus collisions at lower energies could signal the onset of new physics. At the very least, the measurement will provide a strong constraint on the number of partons or degrees of freedom in the initial state of the collision, and point out the QCD dynamics that are important to the system's evolution.

Chapter 2

Experimental Setup

Collisions of heavy ions with $\sqrt{s_{NN}} = 200$ GeV at RHIC create the highest energy densities over an extended volume accessible for study in the laboratory, the earlier maximum having been achieved at the CERN SPS over the past decade by colliding Pb+Pb at $\sqrt{s_{NN}} = 17$ GeV. The PHOBOS experiment was conceived on the premise that signatures of new physics at RHIC energies are largely unknown; current phenomenology and data from lower energies at CERN can only act as a useful guide to measurements that can be interesting, but cannot predict signatures unambiguously.

Given this concept, the PHOBOS detector system was designed to initially study *all* collisions in an unbiased manner. In each collision, the aim is to study the production of *all* hadronic particles. We measure the production angle θ (or equivalently the pseudo-rapidity η) and the azimuthal angle ϕ of all the produced charged particles. This requires a minimum bias collision trigger and a charged particle multiplicity detector with full 4π coverage. The detailed design, implementation and readout of the triggering system and a nearly- 4π multiplicity detector array is discussed in detail in sections 2.2 and 2.3.

In addition, for 2% of the produced particles, the aim is to measure in detail properties like identity and momentum. The 2% includes particles in the mid-rapidity and low- p_T region, where the effects of new physics are likely to be most striking. This requires a multi-particle spectrometer with limited but uniform phase space coverage and a two-particle resolution good enough to be useful for particle correlation studies. A two-arm spectrometer for PHOBOS was built with these considerations in mind, with an acceptance of 11° in ϕ , over 1 unit of mid-rapidity centered at $\eta = 1$ and reaching down to $p_T \sim$

30 MeV/ c . The high p_T coverage of the spectrometer is augmented with a time-of-flight (TOF) detector made of an array of scintillator detectors. Data from the spectrometer and TOF system were not used in the context of this thesis, so their design is not discussed in detail here.

2.1 The Relativistic Heavy Ion Collider

Fig. 2-1 shows the layout of RHIC[81]. Au^{+79} nuclei circulating in RHIC originate as Au^{-1} products of a sputtered ion source operating in pulsed mode. Typical pulse duration is kept at 500 μs , and the ions are accelerated twice through a potential of 14 MV in a tandem Van de Graff generator. At the end of each acceleration cycle, 12 and 21 electrons are respectively stripped from the Au^{-1} ions by passage through a thin carbon stripping foil. Typical stripping efficiencies are 15% at each stage, resulting in a pulsed beam of $\sim 10^{10}$ Au^{+32} ions at a total energy of ~ 1 GeV/nucleon (kinetic energy 2 MeV/nucleon) available for further acceleration.

These low-energy Au^{+32} ions are transported to a booster ring for pre-acceleration up to an energy of 1.03 GeV/nucleon, sufficient to survive the stripping of another 45 electrons. The resulting pulsed beam of Au^{+77} ions is injected into the AGS ring where it is accelerated up to 9.79 GeV/nucleon, stored for multiple turns and delivered to experimental beam lines: one of these beam lines leads into the Relativistic Heavy Ion Collider (RHIC). RHIC employs superconducting magnets arranged in two concentric rings to accelerate two beams of Au^{+79} ions up to 100 GeV/nucleon. After acceleration, it works as a storage ring, circulating the counter-rotating ion beams for up to 10 hours at a time. The beam orbits intersect at 6 points along the RHIC circumference leading to bunch crossings every 1.2 μs , providing collisions simultaneously to 6 experimental halls. Four experiments: BRAHMS[82], PHENIX[83], PHOBOS[84] and STAR[85] are currently in place to observe the by-products of these collisions.

The beam transport and acceleration mechanisms used all work on the principle of an alternating synchrotron, common in most modern accelerator systems. A confined beam of highly charged ions traveling at relativistic speeds tends to disperse due to repulsion among the ions. The beam is focussed using an array of quadrupole magnets arranged to alternately provide focusing in two perpendicular transverse directions. Each set of

magnets focuses the beam in one transverse direction and defocuses it in the other direction. As in optical lenses,¹ the net effect of the array is to maintain the focus of the beam. Dipole magnets inserted in this array provide small angular deflections and keep the beam in a circular orbit. Electromagnetic cavities with RF fields are used to impart synchronised ‘kicks’ of acceleration to the bunches as they circulate around the ring, with the frequency of the kicks increasing as the velocity of the ions increases. In storage mode, the RF cavities are used to provide just enough acceleration to compensate for the (small) energy loss due to synchrotron radiation and maintain a stable beam orbit.

Table 2.1 summarizes important operating parameters of the RHIC, AGS and booster complex over two running periods in 2000-2001, during which data presented here were collected.

A noteworthy feature of all accelerators required to accelerate particles beyond an energy of a few GeV is the phenomenon of ‘transition’ [86, 87]. For a particle at the center of a bunch that is in perfect synchronisation with the RF, the time period of an orbit is $T = C/v$ where C is the circumference and v is its velocity. For an *off*-synchronous particle with a momentum difference Δp :

$$\frac{\Delta T}{T} = \frac{\Delta C}{C} - \frac{\Delta v}{v} = \left(\alpha_c - \frac{1}{\gamma^2}\right) \frac{\Delta p}{p} \equiv \eta \delta \quad (2.1)$$

¹ The net focal length of 2 lenses of focal length f_1, f_2 (negative) situated s apart is:

$$\frac{1}{F} = \frac{1}{f_1} + \frac{1}{f_2} - \frac{s}{f_1 f_2}$$

If $|f_1| = |f_2|$, then $F = |f_1 f_2|/s > 0$. The alternate magnetic ‘lenses’ are arranged in a ‘FOcusing-DefOcusing (FODO) lattice’ with their focussing and defocussing planes rotated by 90° to achieve a similar effect.

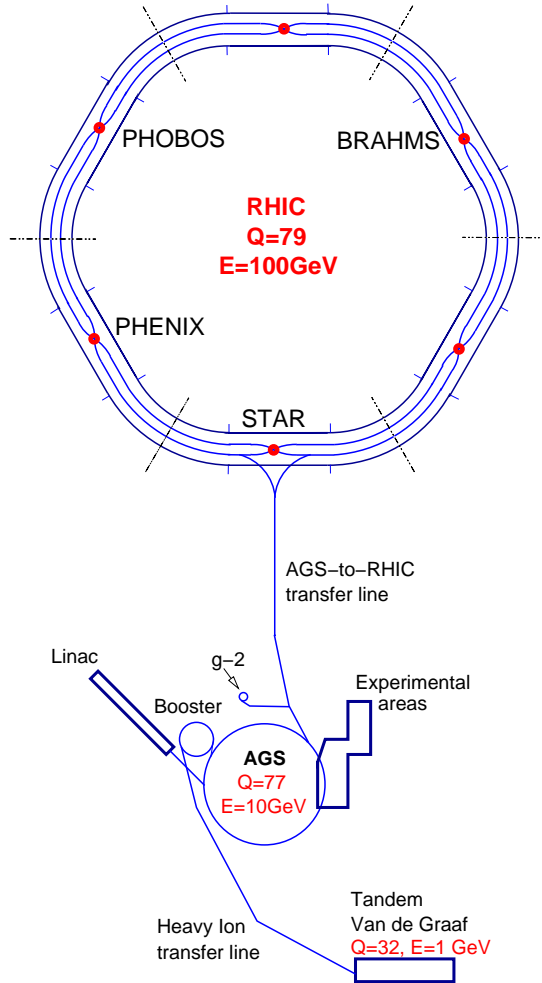


Figure 2-1: Layout of RHIC/AGS

Machine	Q	Injection E (GeV/nucleon)	γ_T	Extraction E (GeV/nucleon)
Booster	+32	0.932	–	1.032
AGS	+77	1.028	8.5	10.264
RHIC	+79	9.558	22.9	(See table below)

RHIC Run	Dates	RHIC $\sqrt{s_{NN}}$ (GeV)	Beam Intensity (ions/beam)	Luminosity (Instantaneous/Integrated)
CR00	March-July 2000	56,130	$\sim 10^9$	$<0.1 \text{ pb}^{-1}/\text{s}; <5 \text{ nb}^{-1}$
PR00	July-Aug 2000	130	$\sim 10^9$	$1 \text{ pb}^{-1}/\text{s}; 2.4 \mu\text{b}^{-1}$
PR01	July-Nov 2001	22,200	$\sim 5 \times 10^{10}$	$100 \text{ pb}^{-1}/\text{s}; 35 \mu\text{b}^{-1}$

Table 2.1: RHIC/AGS/Booster parameters over 3 running periods: CR00 = Commissioning Run 2000; PR00 = Physics Run 2000; PR01 = Physics Run 2001.

where $\Delta C/C \equiv \alpha_c \Delta p/p$ is the definition of the so-called ‘momentum compaction factor’ α_c . For a critical value of $\gamma = \gamma_T \equiv \alpha_c^{-1/2}$ during acceleration, all particles in a bunch travel rigidly around the accelerator with equal revolution frequencies.

For $\gamma < \gamma_T$, a higher momentum particle will have a shorter revolution period than the synchronous particle. Since its higher velocity will compensate for its longer path length, it will arrive at a fixed location earlier than the synchronous particle. In the absence of a longitudinal confining field, a higher momentum particle will therefore drift away from the synchronous particle at a rate $\sim T_0 \eta \delta$ per revolution.

For $\gamma > \gamma_T$ however, Eqn. (2.1) changes sign, and the converse is true. At $\gamma = \gamma_T$, the frequency spread of the beam $\Delta\omega = -\eta\omega\Delta p/p$ vanishes, and there is almost no damping of longitudinal collective instabilities. The switch from $\gamma < \gamma_T$ to $\gamma > \gamma_T$ is called transition, and the longitudinal dispersion of the beam needs to be carefully controlled during this phase.

Various schemes[88] with the RF acceleration cavities can be employed to preserve longitudinal stability of the beams. For PR01, an innovative γ_T -jump scheme was employed in RHIC: as the beam energy nears transition, the *amplitude* of phase oscillations of particles in the beam reduces to zero, so selective quadrupole magnets are pulsed for short periods of time to provide discontinuous phase shifts to particles in the bunches. RHIC ($\gamma_T = 22.9$) is the first accelerator with superconducting magnets to cross transition.

2.2 The PHOBOS detector

Fig. 2-3 shows the PHOBOS experimental setup located at the 10 o'clock interaction region in RHIC. It comprises several major components but few technologies. The primary division is between photo-multiplier based detectors used for triggering and time-of-flight measurement on the one hand, and silicon pad detectors used in the multiplicity array, the vertex detectors and two-arm spectrometer. The trigger detectors and multiplicity array are described in detail in the following sections.

The apparatus is centered around a beryllium beam pipe and anchored by double-dipole magnets used for momentum analysis in the spectrometer (only the bottom yokes of the magnet are shown in Fig. 2-3). The two counter-rotating ion beams are bent towards a single interaction point by RHIC dipole magnets situated on either side of the interaction region (Fig. 2-2 shows the layout of the PHOBOS experimental hall). The beryllium beam pipe used to confine the beams is 5 cm in radius, 1 mm in thickness and spans 12 m in three sections. The thickness is kept at a bare minimum to minimize the amount of background generated even in this low- Z material.

The standard PHOBOS co-ordinate system has its origin at the nominal interaction point. The \hat{z} -axis is along the beam line, with the spectrometer arms located towards positive values of \hat{z} . The \hat{y} -axis is defined to be vertically *up* and the \hat{x} -axis is defined to make the co-ordinate system right-handed. For a particle produced at $(0,0,0)$, the polar angle θ defined with respect to $+\hat{z}$ determines its pseudo-rapidity $\eta \equiv -\ln(\tan \frac{\theta}{2})$.

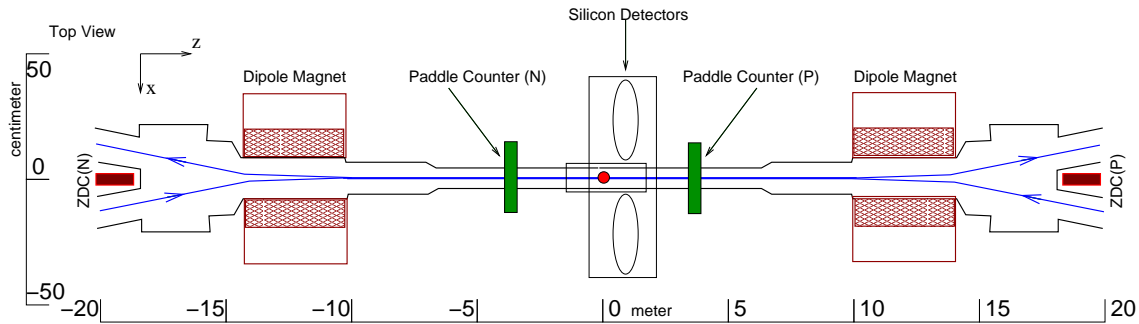


Figure 2-2: Layout of the PHOBOS experimental hall

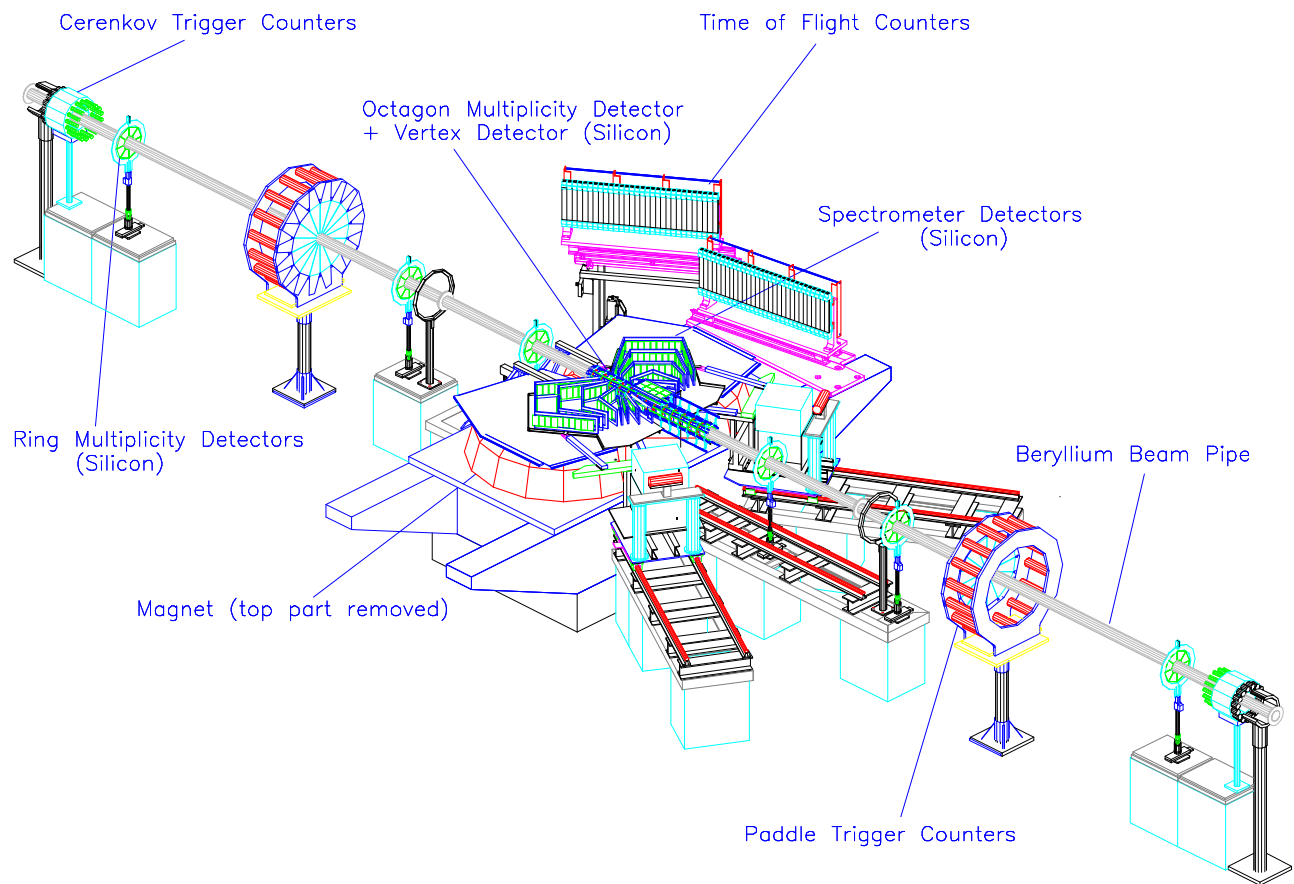


Figure 2-3: The PHOBOS experiment. Relevant sub-detectors used in this thesis are described in the text

2.2.1 Trigger detectors

The primary triggering for PHOBOS is provided by the paddle counters[89]: two sets of 16 scintillators located at -3.21 m (PN) and $+3.21$ m (PP) from the nominal interaction point along the \hat{z} -axis. The scintillators form annuli perpendicular to the beam line. The paddle's active area subtends 99% of the solid angle over a pseudo-rapidity range of $3 < |\eta| < 4.5$. Fig. 2-4 shows one set of paddle counters and a detail of one of the modules. The individual scintillators are

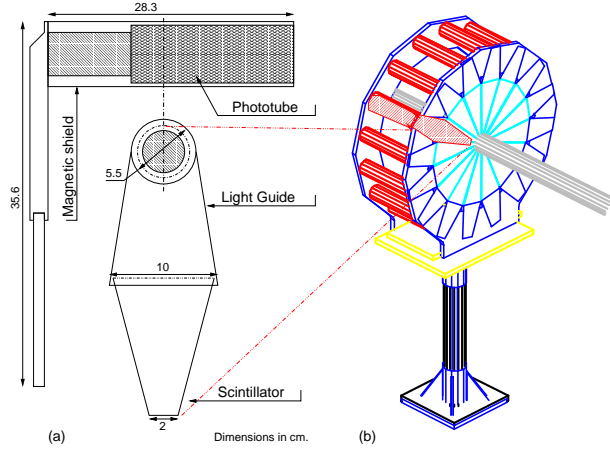


Figure 2-4: a) Design of a single paddle module. b) 16 paddle modules mounted together.

made of BC-400 plastic. The light guide (BC-800) has two components, one that couples to the scintillator and another that couples to the phototube. A 45° aluminized mirror reflects light through the 90° angle between the two components of the light guide. The scintillator and light guide are coupled with BC-500 optical epoxy. At the end of the light guide, a hybrid photo-multiplier tube assembly (H1151-2 from Hamamatsu) is attached with silicon elastomer and encased in a magnetic shield. By design, the paddle counters are not sensitive to the direction of the beam, i.e., there is no difference in the module response to particles incident from the front or back of the scintillator.

Charged particles created in Au+Au collisions stream outwards and deposit energy in the paddle scintillator modules. A coincidence of at least one hit in any of the modules in both the positive (PP) and negative (PN) paddles, within a time window of 76 ns provides the primary, minimum bias trigger for the experiment. Since the time-of-flight to either PP or PN paddles is $s/c \sim 11$ ns, the primary trigger captures both collision events as well as various forms of background. Background events are rejected online and offline through various hardware and software means, described in chapter 4. Per collision, timing and pulse height information is recorded for each paddle module. A typical minimum-ionizing particle deposits 1.64 MeV in one of the scintillator modules and the detectors have a typical signal-to-noise ratio of 20:1 with a time resolution of about 1 ns. Under the

assumption that number of charged particles hitting the paddle modules in a collision event increases monotonically with increasing number of participants (or equivalently, decreasing impact parameter), the energy deposited in the paddle counters provides a good estimator of centrality of collisions.

A second component of the trigger system is a pair of zero degree calorimeters(ZDC)[90] located along the \hat{z} -axis at ± 18 m from the nominal interaction point. Neutrons produced in the mutual Coulomb dissociation of spectator matter from heavy ion collisions travel along the beam axis and deposit energy in the ZDC (charged fragments are swept away by the beam focusing magnets). Theoretical calculations of the cross section for this process[91], indicate a big resonance for the production of single neutrons when such spectator matter dissociates. Requiring a coincidence of neutrons emitted in both forward and backward directions provides a good minimum bias trigger on collisions – background from beam-gas induced dissociations is automatically vetoed. In addition to the purely electromagnetic dissociation through exchange of photons, the number of neutrons produced through *hadronic* interaction is proportional to the geometric overlap of the two colliding ions, though in a non-monotonic manner: for very central collisions, very little spectator matter is available, so the number of emitted neutrons is small. For semi-peripheral collisions, there is a large number of wounded nucleons available for production of neutrons. But for no collisions at all, there is again ‘missing’ energy in the ZDC.

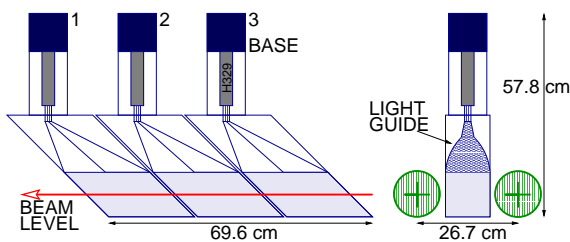


Figure 2-5: Schematic of a ZDC module

Fig. 2-5 shows the schematic design of a ZDC module. It consists of alternating layers of tungsten alloy absorber and cerenkov fiber layers (made from polymethyl acrylate) oriented at 45° to the beam direction and the vertical axis. The shape is optimized to contain the particle shower from absorbed neutrons and discriminate against background particles entering from the back of the ZDC. Three photomultiplier tubes collect light from the modules: timing and energy information from each tube is recorded per event.

The ZDC's constitute the only common sub-detector across all four experiments at RHIC. The triggers provided by forward-backward coincidence of signals in each set of ZDC's are a consistent diagnostic for RHIC machine physicists to tune beam orbits. In

addition, the total inelastic cross section measured in the ZDC's being reasonably well understood[91, 92], the rate of triggers is a good measure of the beam luminosity. In the PHOBOS experiment, the timing signals provided by the ZDC are mainly used to veto background events in the primary paddle coincidence trigger. The energy measured in the ZDC's also provides an important cross-check on the centrality of collisions in the range where the ZDC response is monotonic.

2.2.2 Multiplicity array

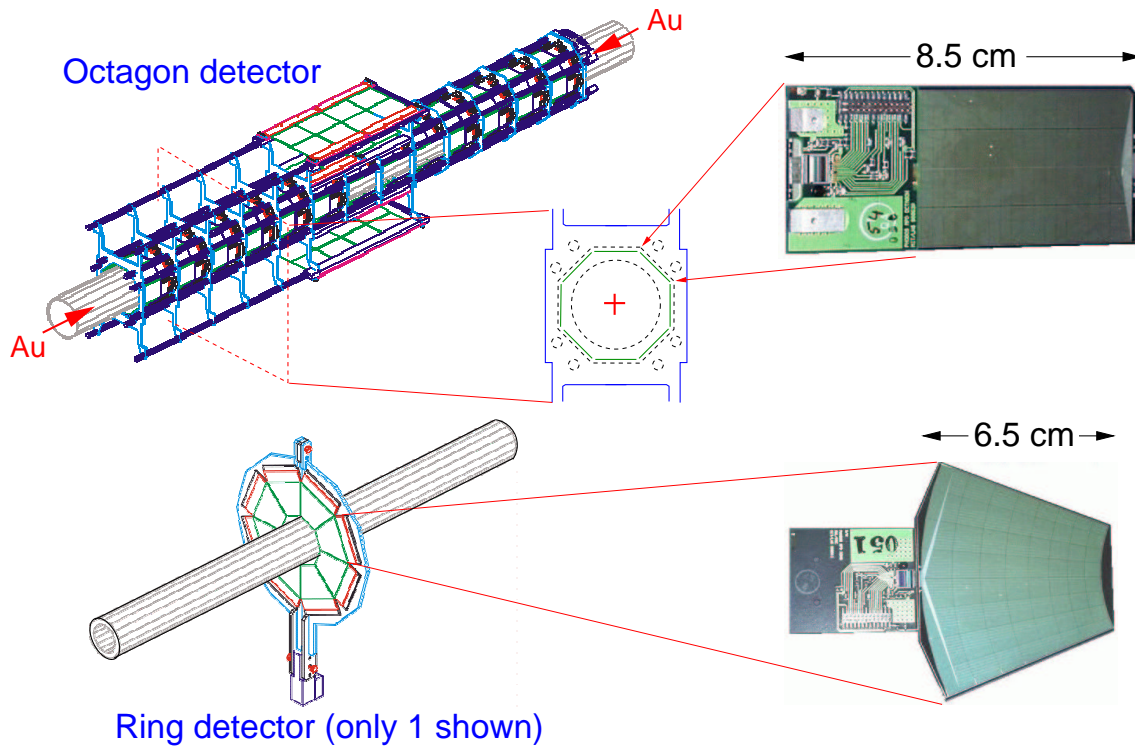


Figure 2-6: Components of the multiplicity detector

The primary sub-detector used for measuring the distribution of charged particles presented here is the PHOBOS multiplicity array, depicted in Fig. 2-6. It consists of rectangular silicon pad detectors with $2.7 \text{ mm} \times 8.7 \text{ mm}$ pads mounted in an octagonal barrel approximately 1.2m long: the *octagon* detector. Each of the eight “ladders” or sides of the octagon contains 13 silicon sensors mounted parallel to \hat{z} , at a distance of 4 mm from the beam pipe. Three sensors in four of the ladders are absent, to prevent extra material intruding into the acceptance of spectrometer and vertex sub-detectors. The octagon detector acceptance for charged particles extends over $|\eta| < 3.2$ and nearly 2π in ϕ . The acceptance is

extended out to $3 < |\eta| < 5.4$ by the *ring* detectors. These are annuli of silicon divided into azimuthal segments mounted at $z = \pm 1, \pm 2$ and ± 5 m from the nominal interaction point. Each silicon sensor in the ring detector has pads laid out in 8 rows along the radius, and 8 columns along ϕ , with the pad size increasing radially outward to ensure that each pad spans an equal $\Delta\eta\Delta\phi$ slice.

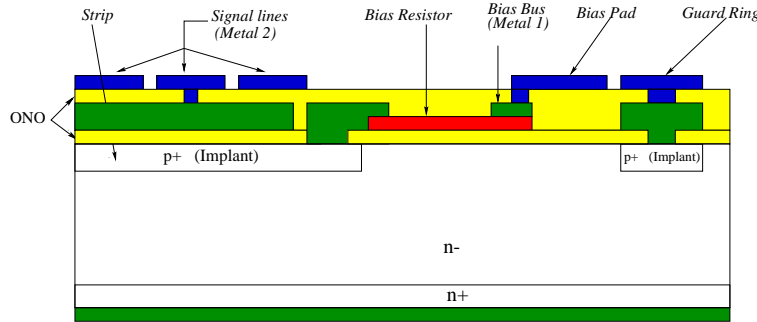


Figure 2-7: Cross section of a silicon sensor

The silicon sensors[93] all work on the principle of charged particle passage causing electron-hole pair creation in a fully depleted, reverse biased p-n junction. The sensors are made from nominally $300 \mu\text{m}$ thick silicon wafers implanted with p^+ (Boron) pads to create a matrix of p-n junctions. A reverse bias voltage is applied to the sensor through an n^+ (Arsenic) doped back-contact layer coated with aluminum. The bias voltage is adjusted such that nearly the full thickness of the silicon is depleted of free carriers, and an electric field is set up across the thickness of the sensor. When a charged particle traverses the sensor, ionization leads to electron-hole pairs which drift under the influence of the electric field and induce a signal in aluminum pickup pads AC-coupled to the p^+ pads via an ONO (oxide-nitrous-oxide) dielectric layer. Each aluminum pad connects to its own aluminum readout line, which carries the induced charge to the front-end-electronics mounted at the edge of the silicon sensor (described in detail in the following section). The network of readout lines is separated from the layer of aluminum pickup pads by a thick dielectric layer. A cross section of a typical sensor is shown in Fig. 2-7.

The long metal readout lines used to connect individual pads on a silicon sensor to the inputs of the readout chip are kept narrow ($\sim 15 \mu\text{m}$), but nonetheless provide an undue capacitive coupling to other pads over which they must run. This capacitive coupling not only proves to be an undesirable mechanism for channel-to-channel cross talk, but also acts

as an input capacitance to ground to the front-end-electronics, degrading the signal-to-noise ratio. This issue is discussed in detail in chapter 3.

2.3 Front-End-Electronics for silicon detector readout

The front-end electronics for the silicon detectors[94] serves 146,944 readout channels: of which there are approximately 56,000 active channels in each of two spectrometer arms, 15,000 in the multiplicity array and 8,000 in the vertex detectors. Due to projective geometry and the differing needs in the spectrometer, multiplicity and vertex systems, the physical form of the detector modules varies somewhat throughout the detector. The various requirements are met using modules which have from one to four sensors served by as many as sixteen, 64- or 128-channel front-end chips.

The front-end system has a uniform readout structure comprised of the elements shown in Fig. 2-8. A detector module, composed of silicon sensors and front-end chips on a hybrid, connects via a short cable to a nearby front-end controller. The controller digitizes the event data and sends it over G-Link to a data concentrator; the latter collates the event data into serial streams and transmits them over optical fibers to the data acquisition (DAQ) system. Together the front-end and DAQ systems handle event rates up to 200Hz with raw data of 260 kB/event, and the DAQ system sends data to the RHIC central data storage system at a sustained rate of 30 MB/s. Pedestal subtraction and zero suppression of the data is handled off-line. The following sub-sections cover the design features of the different system components in the front-end electronics.

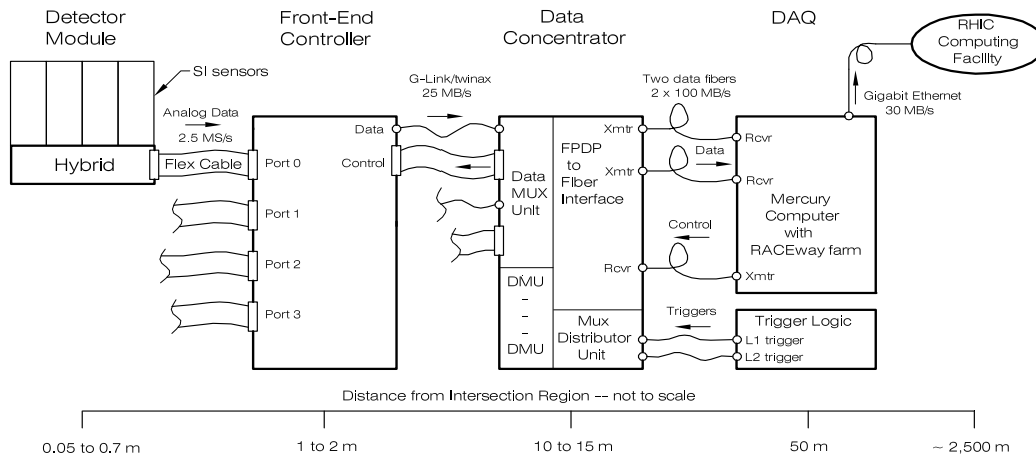


Figure 2-8: Layout of the PHOBOS silicon readout system

2.3.1 Front-end chips

The front-end chips are from the commercially available line of VA integrated circuits[95, 96, 97]. These chips have a dynamic range of 100 MIPs and are configured in 64- and 128-channel versions. A partial, functional block schematic of the chip is shown in Fig. 2-9. Each channel of the chip contains a charge-sensitive pre-amplifier; the integration time is 100 ns at a 10 pF source capacitance, and the decay time is adjusted to about 50 μ s. The pre-amplifier is followed by an RC-CR shaping stage, with peaking time of 1.2 μ s, and a track-and-hold stage. A suitably delayed version of the event trigger switches the chip from track to hold and captures the peak of the signals on their respective hold capacitors. During readout an output control shift register (not shown) sequentially selects the hold capacitor in each channel and connects it to the output stage which drives differential output currents onto the analog bus. The “SHIFT_OUT” from the shift register feeds the “SHIFT_IN” input of the next chip. A second shift register (not shown) on the chip is invoked only during test or calibration. The calibration step input signal (0 to 190mV max.) is fed via an off-chip, 2 pF calibration capacitor to an internal bus on the chip, and the test shift register connects this bus to each channel’s input in turn. A detailed discussion of the calibration system and its performance is given in [98].

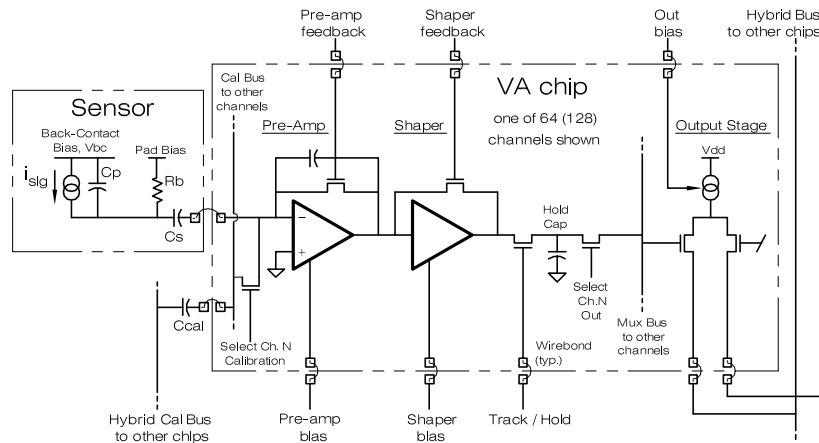


Figure 2-9: Partial schematic of VA chip

The VA chip’s control shift registers and bussed differential analog output allows several of the chips to be concatenated on one hybrid. This renders the connection requirements between hybrid and front-end controller uniform throughout the system, *i.e.*, makes the connections independent of the number of chips per detector module.

2.3.2 Hybrids

The hybrids use thick-film circuits on alumina substrates that provide good thermal conduction of the heat generated by the VA chips (about 1.3 mW/channel) to the water-cooled aluminum mounting frames. The circuits are composed of six layers: three signal layers on the top side, and on the bottom a layer each for ground and the two power rails ($V_{dd} = +2V, V_{ss} = -2V$). Of the three signal layers, two accommodate the 200 μm pad pitch at the control side of the VA chip, and the third carries a bus which connects all chips to the I/O connector, a 30-pin header, at one end of the substrate. The densest substrate used in the spectrometer is 148 mm in length, carries twelve 128-channel chips, and has a total current draw of 0.9A on -2V and 0.15A on +2V. The hybrids used for the multiplicity detector components are relatively simpler, carrying one 128-channel chip per octagon sensor, and one 64-channel chip per ring sensor. Since the VA chip uses power rails of only ± 2 V, gold thick-film conductors are used to minimize the load-induced voltage drops along the length of the substrate. Top-side components include the VA chips and their associated biasing resistors, bypass capacitors, a calibration signal attenuator, the calibration capacitors, and a temperature sensor. Bottom-side components are restricted to the 10 k Ω limiting resistors and 4.7nF/200 V bypass capacitors that serve the back-contact electrode of each silicon sensor.

2.3.3 Front-End Controllers

The detector modules are powered, controlled and read out over flex cable by front-end controller (FEC) modules located 2 m from the silicon array. Due to their proximity to the detector, the FECs and the crates which house them are custom-designed to meet tight spatial constraints. The FEC is a 6U-high module composed of a signal board and a daughter power board with power regulators. There is no crate back-plane: the control signals and data are cabled directly to the module's respective data multiplexer unit in the data concentrator. Low-voltage, DC power is distributed on a busbar system at the rear of the crate and is jumper-ed to the FEC's power board.

FEC Signal Board

A block schematic of the signal board is shown in Fig. 2-10. The signal board has four ports; each port controls and reads out a detector module. In addition to providing the control signals for the VA chips, each port uses a serially-loaded 8-bit DAC to provide programmable bias for the sensor's back-contact and a set of biases for the VA chips. Each port uses an 8-bit scanning ADC to monitor these biases and the substrate temperature; the digitized values are appended to the event data at readout time.

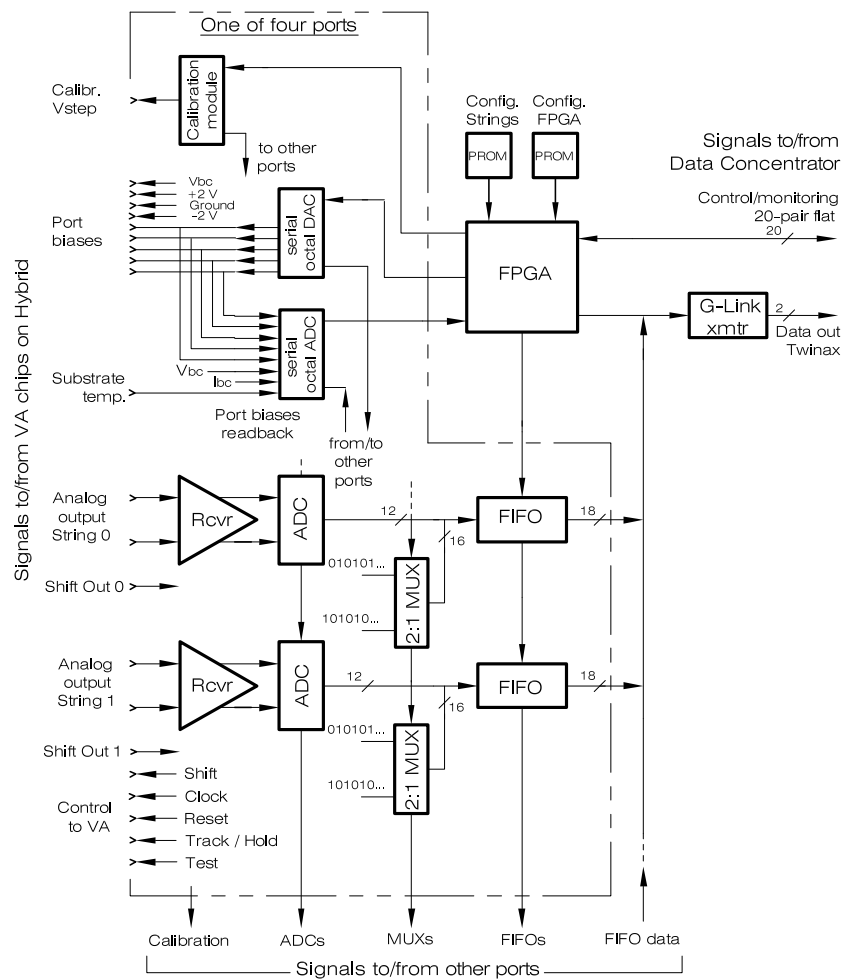


Figure 2-10: Schematic of Front-End-Controller signal board

To reduce dead-time, the detector module's readout chain is divided into two strings to be read out simultaneously. Each string sources a differential analog signal and a digital signal, "SHIFT_OUT", which flags that the last channel of the string has been read. The two circuits (one per string) in each port of the signal board each contain a differential

receiver, a differential pipelined 12-bit ADC, and a FIFO which can store two events worth of data from up to 1,000 channels; the maximum number of channels/string in our system is 768. The string circuit also contains a built-in pattern generator for testing the data chain beginning at the FIFO input.

The FEC uses a field programmable gate array (FPGA) to coordinate the activities of the module in each of four modes: Set-up; Test; Calibration and Run. At power-on, the FPGA's internal logic is configured from a PROM. The configured FPGA then reads a second PROM containing information specific to each port including safe, initial bias levels for the sensor and VA chips, and the number of channels per string. In the Run mode, the FPGA idles with the VA chips in tracking mode; upon receiving Level-1 trigger, the FEC sends a "HOLD" signal to the VA chips causing them to capture the peak of the channel signals. At the Level-2 trigger, the FEC begins reading out the strings into their respective FIFOs. When this process is complete, the controller unloads the FIFOs in sequence and appends a trailer block with temperature and bias values for each port. A G-Link interface in the FEC transmits this event data at 25 MB/s over a 10 m, twin-axial cable to a data multiplexer unit in the data concentrator described below. If a Level-2 trigger is not received within $10 \mu\text{s}$ of the Level-1 trigger, the FEC puts the VA chips back in tracking mode.

FEC Power Board

Due to the rather fragile nature of the silicon system, the DC power distribution system is partitioned at the port level: each port has its own $\pm 2\text{V}$ regulators for the VA chips (and the drivers and bias circuits which control them), a programmable 0 to $+200\text{V}$ regulator for the sensor back-contact bias (V_{bc}), and $\pm 5\text{V}$ regulators for the port's analog front-end. A single, $+5\text{V}$ regulator provides power for the digital logic and serves the whole board. Since the VA chip has no ESD protection at its detector signal inputs, the V_{bc} regulator is designed to limit the rate of change of its output voltage; this in turn limits to a safe level the back-contact-to-pad capacitive charging/discharging currents at the VA chip inputs. To further protect the VA chips, low dropout regulators fed from $\pm 3\text{V}$ supplies are used; the worst-case voltage applied to the VA chips due to regulator failures is 6V which is still within the voltage rating of the process ($1.2 \mu\text{m}$, n-well CMOS) used for fabricating the chips. The 5V regulators are fed from 6V , and the four DC inputs to the power board, $\pm 3\text{V}$ and $\pm 6\text{V}$, are supplied by a power unit which handles up to 8 FECs – potentially as

many as 64,000 channels. The power unit is located about 2 m from the FEC crate; it is controlled and monitored via CANbus, and it also provides monitoring for the fan cooling units attached to the crate.

Radiation issues and Latch-up Protection

Although operating front-end electronics in a heavy ion collider environment carries a heavy radiation penalty, the expected integrated dose of radiation received by the detector and electronics (~ 4 krad/year) at nominal RHIC energies and luminosity is not expected to cause severe degradation in the detector performance for at least a few years. Therefore, the front end electronics is operated at room temperature, with a circulating water cooling system to dissipate heat from the hybrids. It is only at the much higher energies and luminosities of the future Large Hadron Collider (LHC), that sustained high-radiation dose requires the electronics to be operated at cryogenic temperatures: CMOS electronics that has been pre-exposed to radiation and is operated at cryogenic temperature becomes radiation tolerant to the levels of tens of Mrad[99].

Nevertheless, with energetic beams of heavy ions circulating in the collider, the possibility exists for instantaneously sending unusually large amounts of radiation through the sensors and front-end chips of the silicon detector modules: if part or all of the beam clips the wall of the beam pipe, the fragments from this “fixed target” collision are sent in a very forward direction in close proximity to the beam pipe in the intersection region.

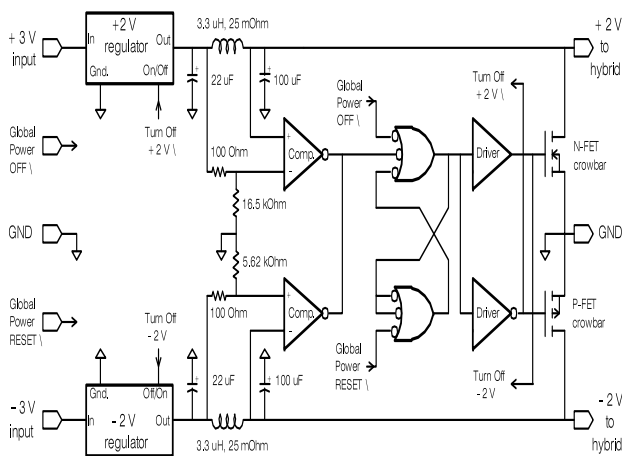


Figure 2-11: Latch-up protection circuit schematic

Since the plane of the sensors and chips of the detector modules near the beam pipe are aligned with the axis of the pipe, a rogue particle can travel several millimeters in a given sensor or chip. If a charged fragment of the collision passes through a front-end chip, the charge it deposits in the bulk of the chip causes the parasitic transistors (which are inherent in the CMOS structure and create a parasitic, four layer silicon controlled rectifier) to suddenly turn on, latch up, and con-

duct abnormally large currents which disable the chip[100].² Normal operation can only be recovered by immediately turning off the power to the hybrid and then later resetting the power. To protect against such radiation induced latch-up, an interlock-style system was pioneered and implemented in the PHOBOS front end controller boards. Fig. 2-11 shows a block schematic of the latch-up protection circuit integrated with each port of the power board. A dual comparator monitors the voltage drops across the inductors in the π -filters at the outputs of the $\pm 2V$ regulators. If either voltage drop exceeds a fixed threshold, the comparator circuit disables both regulators and activates the crow-bar circuits which rapidly discharge their respective output lines. This action is taken within a few tens of microseconds of the radiation-induced event. The power can be re-applied a few seconds later by sending a global power reset signal.

In practice, the automated latch-up protection system was triggered quite frequently (\sim once per 15 minutes) due to imperfect control of beam dynamics in the RHIC startup phase. In the later stages of running, the frequency of such events fell to about once per hour.

2.3.4 Data Concentrator

Shown in Fig. 2-12, the data concentrator multiplexes and collates data from the FECs into two bit streams for transmission to the DAQ system. Triggers from the control room are sent to the data concentrator where they are opto-coupled and fanned out to the front-end system. All FECs are unloaded in parallel; each FEC transmits its data at 25 MB/s via G-Link over twin-axial cable to one of two ports of a data multiplexing unit (DMU) in the data concentrator. The DMU interfaces control and monitoring signals to and from the FECs over 20-pair flat cables. The DMU's port data are stored, two hits wide with parity, in a 36-bit x 4k-word FIFO. Under the control of the Multiplexer Distributor Controller (MDC), the DMU FIFOs are multiplexed in turn to a common 32-bit bus with Front Panel Data Port (FPDP) protocol[101].

²In the worst case, it was found under test conditions that the delicate bond wires supplying current to the chip fused due to abnormally large current draw and needed to be replaced. In some cases, the bond wires did not fuse, causing permanent overcurrent damage to the chip

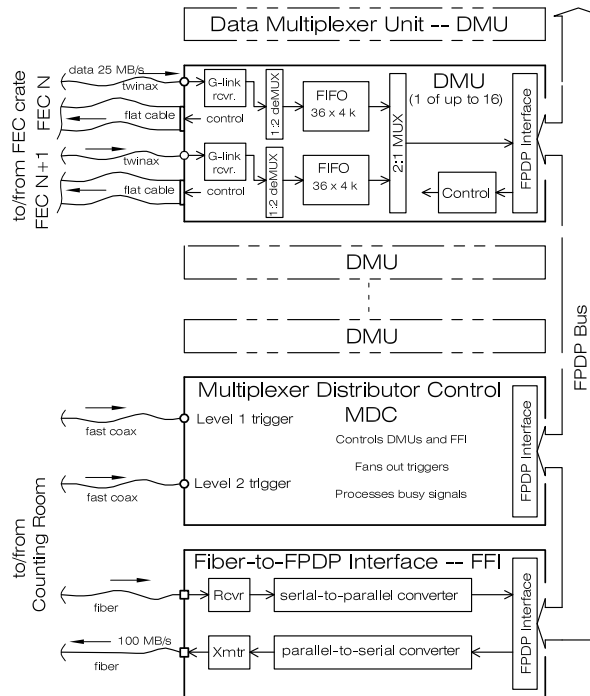


Figure 2-12: Data concentrator for multiplexing data from FECs

Data on this bus are received by a Fiber-to-FPDP Interface (FFI) module in the same crate; this full-duplex module serializes the data and transmits them at 100 MB/s over an optical fiber to the control room. The MDC module provides the master function in a crate filled with DMU modules, and it prepares data (bias parameters for each of four ports in each FEC) for downloading to the front-end system. It fans out the L1, L2 triggers to the front-end controllers and handles their busy signals. It checks record length and parity for data on the FPDP bus and adds status information at the end of each record. The MDC's tasks are controlled by commands received over fiber from the DAQ system; this receiving fiber occupies the second port of the full-duplex FFI module.

2.3.5 Data Acquisition

The data acquisition system (DAQ) for PHOBOS[102] receives data from 135,000 silicon detector channels and 2000 scintillator detector channels. It occupies a single VME crate and can accept data at a rate of up to 200 events/sec and send them over Gigabit network to the RHIC central data storage system at a sustained rate of 30 MB/s. The total benchmarked processing power is 330 SPECint95.

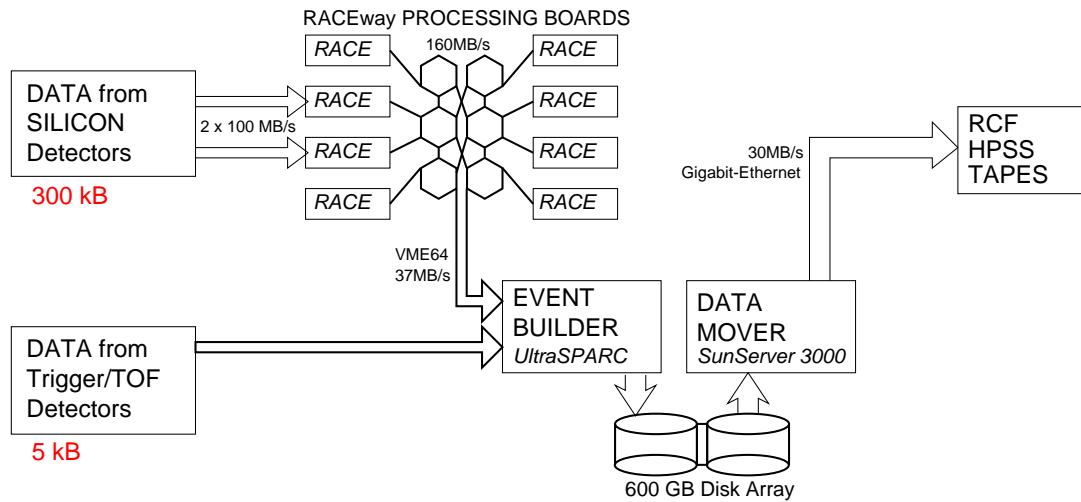


Figure 2-13: Layout of the PHOBOS DAQ

The structure of the PHOBOS DAQ is shown in Fig. 2-13. It consists of a top-level event-builder processor, which is triggered by a set of trigger-managers that generate Level-0 and Level-1 triggers. It receives data from two sources:

1. Silicon front-end-electronics, via a set of PowerPC processors interconnected by a RACEway[103] network, and
2. Scintillator detectors (trigger detectors and the TOF array), via a set of FastBus[104]-based signal and timing modules.

Due to the vast difference in sizes, these two subsystems have very different latency times. Once a Level-0 trigger has been issued, the scintillator subsystem is ready to be read out in $\sim 10 \mu\text{s}$, while data from the silicon subsystem has to arrive through the multi-stage front-end electronics and is only available after $\sim 3 \text{ ms}$. The front-end design and dead times are also quite different: the scintillator subsystem is not multi-buffered, so each event needs to be read out sequentially. If an event is to be rejected, a 'FASTCLEAR' needs to be issued to the scintillator readout modules earlier than 400 ns after Level-0, before digitization of data has begun. The silicon subsystem starts operations when it receives a Level-1 trigger, as has already been described in the previous section. A composite timing diagram of DAQ operations is shown in Fig. 2-14.

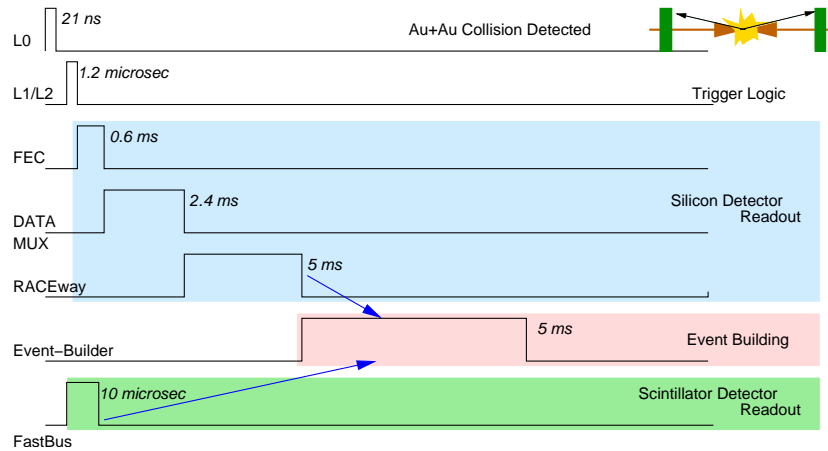


Figure 2-14: Data acquisition timing diagram

Triggering of DAQ readout is managed by a set of VME-based custom-designed trigger-manager modules[102]. Various combinations of outputs from the trigger detectors are used to arrive at logical signals signifying ‘interesting’ events and fed into the Level-0 trigger-manager (details of the logic are presented in the chapter 4). The Level-0 trigger-manager is aware of the ‘BUSY’ status of all subsystems, and if the DAQ is unable to accept this trigger, a ‘FASTCLEAR’ is issued to the scintillator subsystem. Otherwise, it is propagated up to the Level-1 trigger-manager. At Level-1, details of the logic are examined (certain background events are partially ignored or ‘scaled down’) and the timing is adjusted to broadcast a Level-1 trigger to all subsystems. Nominally, the Level-1 trigger is timed to arrive at the silicon front-end-electronics at $1.2\text{ }\mu\text{s}$ after the collision has occurred, and acts as the ‘HOLD’ signal issued to VA chips.

The synchronization of DAQ components is overseen by an event-manager module. Upon receiving a valid Level-1 trigger, the event-manager generates a unique 8-bit synchronization number and sends it out to the silicon and scintillator detector subsystems. The front-end electronics for both subsystems send up digitized, multiplexed data buffers tagged with this 8-bit number in the header to the event-builder.

The multiplexed data from the silicon front-end electronics arrives over two fiber optic cables to the DAQ VME crate (Fig. 2-13). All data transfer within the crate occurs over RACEway, a network of crossbar switches, which connect terminal elements such as Compute Environment modules (CE), I/O modules and communication bridges. Two RACEway input devices (RINT) receive the data under the control of a ‘Master CE’. The data is distributed to local memories of analyzing ‘Worker CEs’. Each Worker watches a buffer in

its local queue for modification and as soon as it detects arrival of the last word of a dedicated data buffer it starts data processing. All the CE modules used are dual PowerPC-750 processors each with 32 MB of on-chip RAM and 32 kB of L2 cache memory. The point-to-point connections created by RACEway between the processors allow high-speed (160 MB/s) transfers of data between memory buffers on different processors. There are 23 Worker CE's in the system, all running copies of the same code on its input queue of data frames. The typical size of the frame is 12 kB, it contains data from 2 Front End Controllers (FEC). Such division is dictated by the cache size of the PowerPC processor (32 kB): any high-level processing algorithm like compression to be performed on the data frame is optimal when pedestals and conversion table (12 kB + 6 kB) for the particular data frame are accommodated into the cache. Minimally, the integrity of the data frames is checked and various slow-monitoring parameters included by the FECs in the data frame are evaluated. The processed data frames are tagged with the 8-bit synchronization number sent by the event manager and sent to the output queue located in the Master CE's local memory. The output queue is organized in a slot-based manner, with slots ordered by the synchronization number. System level semaphores and locks are used for communications between the Worker CE's, the Master CE and the event-builder, to enable data to move in a pipelined mode.

The event-builder program is located on an UltraSPARC VME board, in the same VME crate as the RACEway system. It connects to the RACEway network over VME backplane, and pulls data from the Master CE's output queue using DMA-D64 block transfer. In parallel, data from all the scintillator detectors are digitized in the FastBus crate and tagged with the same synchronization number; the event-builder reads them using a dedicated fast ethernet link. As operated over the running periods of 2000-2001, the main function of the event-builder was to concatenate data from the silicon and scintillator subsystems per event and build events in ROOT data format. ROOT [105] is a C++ based object-oriented software framework developed at CERN, around which all PHOBOS analysis software is written. The output of the DAQ therefore consists of ROOT events that are immediately available for online and offline analysis. Further real-time processing of the data, especially compression of the silicon data blocks in the RACEway CE's, and higher level trigger rejection is planned for future running periods.

The event-builder is able to send data directly over Gigabit ethernet to the RHIC central

computing facilities' HPSS[106] central data storage system. However to balance the CPU load, and guard against network latency issues, the data is staged locally on a SCSI disk array. The S100 disk array controller used[107] is a 2×8 SCSI switch, allowing 2 hosts to concurrently access an array of 8 disks. One host port is connected to the event-builder, and the second to a data mover: a 4-processor desktop Sun UltraSPARC 3000 server. The disk usage is scheduled in a round-robin manner so that the event-builder writes data files to one physical disk while the data-mover reads another file from other disk and sends data over Gigabit Ethernet to the HPSS central storage. Scripts run by the data-mover computer automatically launch reconstruction software to make a first pass at analyzing these raw data files on a 200-processor reconstruction farm at the RHIC central computing facility. Thus minimally analyzed data files are available to the end-user typically a couple of hours after the data has been written to HPSS, to proceed with further analyses like the one presented in the following chapters.

Chapter 3

Data Analysis

In this chapter, we provide details of the procedure used to convert analog signals from detector pixels into usable physical parameters. The derivation and application of various calibration constants for the silicon pixel detectors are presented, and the techniques used to correct for noise in the electronics are discussed. Finally, the measured signal response of the detectors is compared to the expected theoretical response.

3.1 Signal processing from Silicon detectors: ADC to keV

As described in the previous chapter, charge deposited in silicon detector channels is collected by pre-amplifiers in the VA front-end chips, and digitized by *analog-to-digital* converters (ADC's) in the front-end controllers. The digitized value of signal from each detector channel (called the ADC value) is written to a data file by the DAQ system for offline analysis. Fig. 3-1 shows the typical ADC values from a silicon sensor for one event. The horizontal axis gives the channel number: each channel corresponds to an (x, y) pixel position on the sensor. The measured ADC output is a convolute of four contributions: it contains the actual signal from a particle traversing the detector, a DC voltage offset of the channel referred to as the “pedestal”, electronics and thermal noise in the channel, and a random event-to-event shift of all voltages on one chip called the “common mode noise” (CMN). Data analysis starts with disentangling each of these contributions to extract the signal.

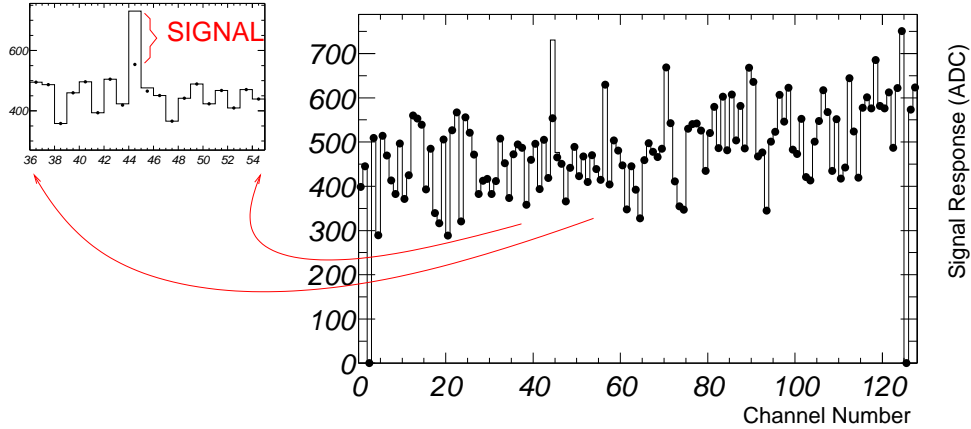


Figure 3-1: Raw data ADC values from Silicon sensor (1 event). The calculated pedestals are superimposed as markers. The inset shows a zoom on a few channels, one of which contains a signal superimposed on the pedestal.

In the following discussion index i denotes the channel number and k the event:

$$ADC_i(k) = S_i(k) + N_i(k) + P_i + CMS(k) \quad (3.1)$$

S_i represents the energy deposited by a particle traversing a detector pixel; a calibration procedure is required to convert it into energy units. N_i is the random noise from the readout electronics associated with each channel. It is roughly independent of the neighbouring channel noise, uncorrelated between events, and cannot be deconvoluted from the particle signal. Its frequency spectrum is not uniform as it is the output of band pass filters in the readout chain *i.e.*, it is not white noise.

The pedestal P_i corresponds to a DC offset of the channel output voltage. At the detector level, it arises mainly from DC leakage currents through the reverse-biased silicon bulk. Active current sources are provided in parallel with each leg of the differential output of the preamplifiers at the FEC level, to correct for a large component of the offset on a per-module basis. Nonetheless, the offset has to be calculated for each channel and corrected in the offline analysis, as large deviations between channels can occur. The pedestals also vary slowly with time as a result of temperature variations and drifts of power supply voltages.

In addition to signal, noise, and pedestal, the voltages of all or a subgroup of channels within a chip can be shifted by a common positive or negative amplitude, called a “common mode shift” ($CMS(k)$). On a chip wise basis, this can be caused by the positive or negative

supply voltage rails sagging due to very large current consumption in a few channels that have a large signal in them. Capacitive coupling to noisy grounds in front-end electronics (“ground loops”) can also induce unwanted common mode shifts. However, the fully differential signal paths used in the VA front-end chips along with meticulous attention to the grounding scheme in the installed detector ensure that this contribution is very small, at a level commensurate with the intrinsic noise of the detector. For the multiplicity detectors, a different source of common mode shifts becomes important: most of the shifts are observed to affect a single row of pads along the length of the sensor. The specific effect observed in the multiplicity detectors, and the procedure used to correct for it is described in detail in the following sections.

3.1.1 Pedestal and noise calculation

In order to prevent drifts of the pedestal values from affecting processing of signals, the pedestals are calculated per data file from the first few events in the run. Since a single run typically spans an hour, and the drifts were found to be insignificant over such a short time scale, the applicability of such pedestal values calculated *in situ* is assured.

The pedestals are calculated in two passes: by looping over the first 200 events in a run and averaging the signal separately for each silicon channel, a “pre-pedestal” value is obtained. In a second pass over the next 300 events, the signals from each channel with the pre-pedestal subtracted, are histogrammed. The most probable ADC value, *i.e.*, the value where the resulting distribution peaks gives for each channel the desired “pedestal” (P_i). Since particle hits can be present in the sample, taking the peak of the distribution gives a better estimate of the pedestal than simply taking the average ADC value. If a peak is not sufficiently evident in this distribution, as may occur for example in parts of the multiplicity detector where the flux of particles hitting the detector is quite high, then the sample of events used is expanded until the peak is found.

The noise is calculated by looping over the next 600 events in the run. The pedestal and common mode shifts (described in the next section) are subtracted for every channel. The resulting distribution is then fitted with a Gaussian in a restricted range around its most probable value. The root mean square obtained from the fit gives the desired value of the noise. The pedestal and noise values are calculated per data run, stored in a central database, and referenced on the fly when analyzing events from the run.

Fig. 3-2a indicates the typical noise values obtained for a representative octagon detector module. The distributions of event-by-event pedestal-subtracted and CMS-subtracted values for a typical channel are also shown in Fig. 3-2b,c.

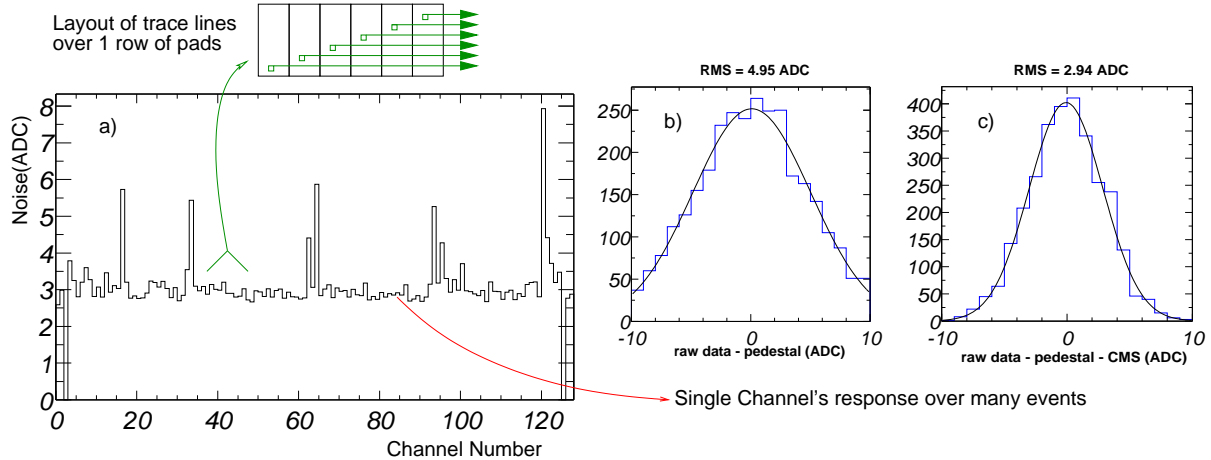


Figure 3-2: a) Calculated noise in ADC units for a typical Octagon sensor. b) Noise distribution in a single channel (3000 events) c) Same distribution after CMS correction.

The distribution of noise as a function of channel number is fairly uniform across the detector and on average is approximately 3 ADC units. The measured value agrees quite well with the modelled noise response of the silicon sensors and front-end electronics (cf. Appendix B for details). It has a characteristic structure (Fig. 3-2a) associated with the geometry of the pads and the layout of readout trace lines on the silicon sensor. Each sensor consists of 120 pads in a 30 (row) \times 4 (column) matrix and is read out by a 128 channel VA front-end chip. The first and last three input channels of the chip are not connected to any silicon pad, with channel numbers 2 and 125 capacitively coupled to the guard ring (*i.e.*, virtual ground) as reflected in their zero noise and pedestal values. In addition, channels 63 and 95 are connected to trace lines that run over the full length of the sensor, but are not connected to any pad. As depicted in the inset of Fig. 3-2a, the noise increases slightly as the length of the trace lines increase, since these run over all the adjacent pads and present an increasing parasitic coupling capacitance at the preamplifier input.

A few readout channels exhibit noise much larger than average, presumably due to defects in the silicon itself causing large leakage currents as charge builds up at the imperfection site. Strict quality control in pre-installation tests of detector modules restricted the fraction of such noisy channels to less than 2%. Over the PR00 and PR01 running periods, the fraction of noisy channels increased only slightly: a few more channels developed

larger noise due to irradiation. When calculating the noise, these channels are marked as anomalous, and discarded in later stages of data analysis.

3.1.2 Common mode shifts

Event-by-event common mode shifts are calculated by making a distribution of pedestal-subtracted signals from groups of channels in the same event. In the absence of any shift, the distribution peaks at zero. Any non-zero offset represents the common mode shift for the group and needs to be subtracted from each channel's response.

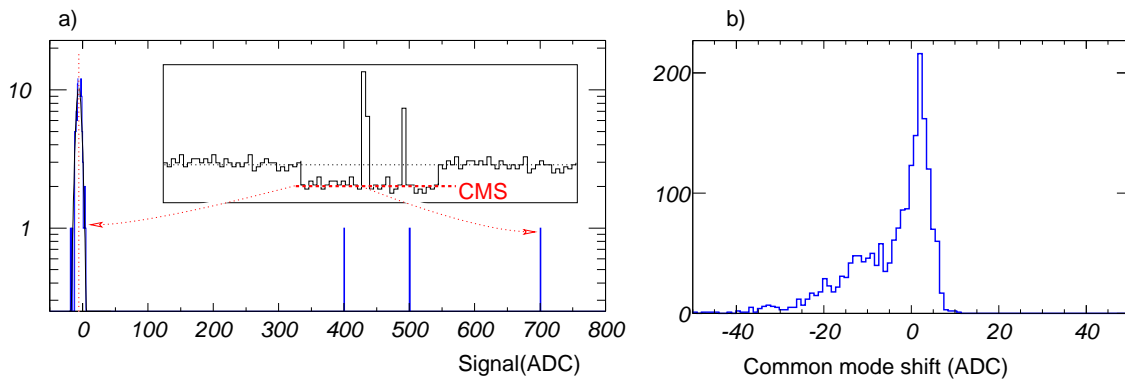


Figure 3-3: a) Distribution of pedestal-subtracted response from one row of pads in an octagon sensor for a single event. The selected row's data is displayed channelwise in the inset, along with two adjacent rows indicating the common mode shift. b) Distribution of the common mode shifts in this row over 3000 events.

Fig. 3-3a shows such a distribution for a single event in a group of 30 channels belonging to a single row in an octagon detector module. As shown in the inset, a large signal in one of the pads in the row causes the baseline of all the other channels in the same row to sag from the capacitive coupling of tracelines running over them. A similar effect is also seen in the ring detector modules, where the shift is worsened by the larger size of the pads and their correspondingly large capacitance. In addition, the pad size in the ring detectors is not uniform: it increases substantially going from the inner to outer radius of a ring module (Fig. 2-6), causing a slope in the capacitive coupling to the tracelines and a corresponding slope in the common mode shift of all channels belonging to the affected row. The common mode correction algorithm for the ring detector takes this slope into account.

In events with large numbers of charged particles traversing the detector, the fraction of channels containing large signals is quite high (up to 80% at mid-rapidity for central

collisions at $\sqrt{s_{NN}} = 200$ GeV) and it is important to ensure that large common mode shifts in otherwise non-hit channels are not mistaken for signal hits. Moreover, the shift is subtracted from the signal in Eqn. (3.1) and can potentially distort the signal distribution from channels containing valid hits. This has been studied using various quality cuts in the context of the multiplicity measurement and is discussed further in chapter 5.

Fig. 3-3b shows the distribution of the calculated common mode shifts for a representative row in an octagon sensor over an ensemble of 3000 events, with shifts upto 30 ADC units on the negative side. It is interesting to note its Gaussian-like shape, lending further support to the hypothesis that the shifts do indeed originate in the parasitic capacitances on the silicon sensor itself. As all the signals pass through the low and high pass filtering stages of the front-end electronics, common mode shifts originating in the latter stages of the electronics would have a non-Gaussian distribution. The distribution shown in Fig. 3-3b has both a Gaussian contribution from sensor capacitances and a non-Gaussian one from voltage rail modulation at the VA chip level.

3.1.3 Gain Calibration

Particles traversing the silicon sensors deposit energy by creating ionization electrons that appear as charge at the input of the preamplifier electronics. After suitable amplification and signal shaping, the digitized value of the charge appears at the output of the ADC. The calibration procedure has two goals:

1. Obtain a *relative* normalization between detector channels so that all channels read the same value (after pedestal subtraction) for a given input charge.
2. Obtain an *absolute* calibration wherein a measured output value of the ADC corresponds to a specific energy loss in the silicon bulk.

For the analysis presented here, the absolute calibration is not important since our inclusive multiplicity measurement relies on the number of hit pixels based on a signal-to-noise cut and not on the absolute value of energy deposited in the pixels. Knowledge of the energy loss is only required to identify particles in conjunction with momentum measurements by using the Bethe-Bloch parametrization[108].

The first objective mentioned above is achieved by injecting known precise charges at the input of the front-end preamplifiers and measuring the outputs. Practically, this is done in dedicated calibration runs by applying fixed voltage steps across known capacitances

connected to individual preamplifier inputs. By increasing the voltage steps, the response of the front-end electronics over the full dynamic range is calibrated. Fig. 3-4a shows the typical response curves of a few channels to the applied voltage steps. The responses are linear and closely matched over most of the dynamic range, and start showing some saturation near the upper limit. These curves are fitted with a straight line in the lower range, and the slopes used to normalize the response of different channels.

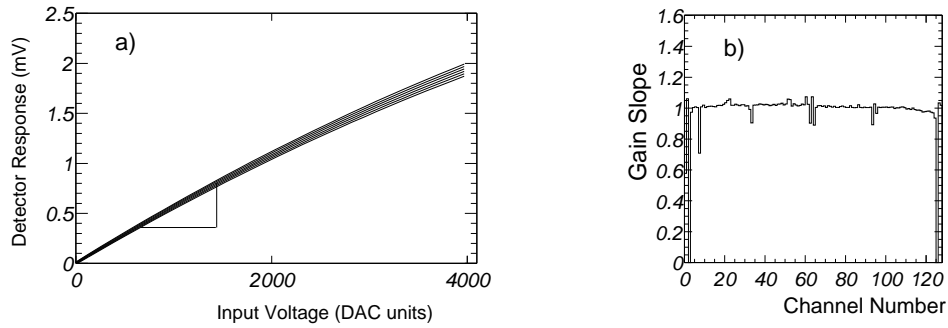


Figure 3-4: a) Response of a few channels in an octagon detector module to the calibration input signal b) The fitted slopes (“gains”) for all channels in the same module

The slope parameters or “gains” obtained from this procedure for all channels in a typical octagon detector module are shown in Fig. 3-4b. A few channels (less than 2% in the installed detector) show anomalously low gain due to faults in their associated readout electronics; these are discarded in later stages of the analysis. Since the measured gains remain nearly constant with time (they are mostly determined by passive components along the front-end electronics chain), calibration runs were taken only once per day during the running period and results of the gain calculation stored in the central database. Offline analyses refer to the most recent gains calculated before the time of data-taking for any specific run.

The calculated gains are multiplied into the event-by-event response of each channel to obtain the normalized ADC response:

$$NormADC_i(k) = ADC_i(k) * G_i \quad (3.2)$$

The normalized ADC measurement can be converted into a specific energy loss by charged particles traversing the channel to obtain an absolute calibration. The conversion procedure

is roughly as follows: the analog-to-digital converters used have a 12-bit range corresponding to a voltage input of -2V to +2V. The amplification and shaping stages can be modelled simply as a charge-to-voltage converter with a net gain of $0.0476 \text{ mV}/\text{ADC}$.¹ The charge is sampled across a nominal capacitance $C_h = 2.14 \text{ pF}$. Since the energy required to produce 1 electron-hole pair (i.e. $1.6 \times 10^{-4} \text{ fC}$ charge) in the reverse-biased silicon bulk is 3.62 eV [109], the required formula to obtain the energy deposited by ionization is:

$$dE_{dep}(\text{eV}) = \text{NormADC} * \left[2.14 \text{ pF} * 0.0476 \frac{\text{mV}}{\text{ADC}} \right] * \frac{3.62 \text{ eV}}{1.6 * 10^{-4} \text{ fC}} \quad (3.3)$$

which simplifies to an absolute calibration of $1 \text{ NormADC} \approx 2.1 \text{ keV}$ energy deposited. All the data presented from here onwards is shown in terms of these calibrated energy units rather than electronic ADC units.

3.2 Quality assurance: comparison with detector simulations

Although the *in situ* electronics calibration procedure described in the previous section is relatively straightforward and parameter-free, it is quite important to also have a well understood physics model of the apparatus. Specifically, an *a priori* unknown fraction of charged particles reaching the silicon detectors may originate as background from secondary interactions in the intervening material, or as decay products of short-lived resonances away from the primary collision vertex. In order to discriminate such background, a simulation of the full apparatus including most mechanical structures has been created using the GEANT 3.21[110] software package. GEANT is a detector simulation software developed at CERN since the 1970's to simulate the passage of particles through matter based on physics parameterizations verified in many test-beam experiments over the years.

The theory of energy loss of charged particles in matter has been developed from first principles by Bethe and Bloch[108] and fluctuations in the energy loss have been treated by Landau[111] with some corrections[112] and additions[113]. Most of these physical principles are encoded in the GEANT simulations, and used to model the response of the silicon detectors.

A second advantage of understanding the detector response in this fashion is that by

¹There is a variation of $\sim 10\%$ in this quantity due to tolerance of passive components and the operational bias settings of the preamplifier and shaper: see Appendix B for details

varying known inputs to the simulation, for example the impact parameter of the collision, the change in response can be gauged. The PHOBOS trigger detectors have also been studied in the simulations to obtain a handle on the impact parameter of collisions as described in the following chapter.

3.2.1 Silicon detector simulation

Fig. 3-5 shows the observed distribution of signals from the silicon pads in a typical multiplicity detector module over a typical ensemble of triggered Au+Au collisions. In events where a pad is not hit, its response is nearly equal to the pedestal value with some fluctuations due to noise. The distribution of signals due to energy deposition by charged particles peaks at the characteristic ‘MIP’ or minimum-ionizing-particle position, with secondary peaks seen for events in which two

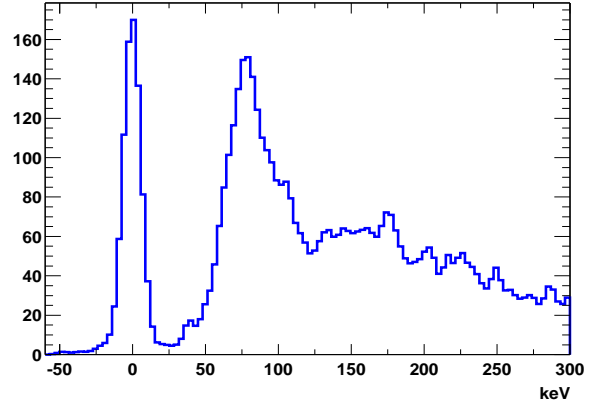


Figure 3-5: Measured calibrated energy loss spectrum from a typical octagon module

or more such particles traverse a single pad. The aim of the simulation is to reproduce this detector response in as much detail as possible, using well understood parameters of the physical processes involved in depositing energy into the the silicon pads.

Moderately relativistic charged particles excluding electrons deposit energy in matter primarily by ionization. The energy loss mechanism can be understood simply in a classical picture of Rutherford scattering off atomic electronics. The energy loss per collision depends strongly on the Z/A of the material, the charge(z) and velocity(β) of incident particle and weakly on other properties of the material. In the limit of a thick absorbing material, the number of such collisions is large and distribution of energy loss is nearly Gaussian, with a *mean* energy loss per unit thickness given by the Bethe-Bloch formula[108]:

$$\xi \equiv \langle \Delta \rangle = K * \left(\frac{Z}{A} \right) * \left(\frac{z}{\beta} \right)^2 * \left[\frac{1}{2} \ln \frac{2m_e c^2 \beta^2 \gamma^2 T_{max}}{I^2} - \beta^2 - \frac{\delta}{2} \right] \quad (3.4)$$

where T_{max} is the maximum kinetic energy imparted to a free electron in single collision, I is the mean excitation energy and $K = 4\pi N_A r_e^2 m_e c^2 = 0.307 \text{ MeVg}^{-1} \text{cm}^2$ is a constant.

δ is an empirically derived density effect correction. The equation produces results valid for charged particles ranging in momentum from 40 MeV/c to 6 GeV/c; beyond these limits, other effects become important. Also, it is implicitly assumed that all the energy lost is deposited in the bulk of the material, i.e. the ionization electrons donot escape in the form of ‘knock-on’ electrons or δ -rays which need to be accounted for separately.

The mean energy loss $\langle \Delta \rangle$ falls rapidly with increasing β , until the $\ln(\beta\gamma)$ term takes over, and the value shows a gentle relativistic rise. If the momentum of the particles is not measured, as in Fig. 3-5, then most of the contribution to the spectrum comes from the relativistic rise range, and all particles beyond the turnover point are simply referred to as minimum-ionizing-particles or MIP’s.

When the absorbing material is thin and the number of collisions small, fluctuations cause the distribution of energy loss to be skewed towards higher values: even though the probability diminishes for large energy transfers in single collisions, the maximum allowed energy transfer in a single collision is taken to be infinite in the limit of an infinitesimally thin absorber. Landau[111] derived the probability distribution in this (unrealistic²) limiting case; the calculation was extended to a realistically thin absorber by Vavilov[112] by introducing a kinematic limit on the maximum transferable energy in a single collision. A further simplifying assumption was that the energy transfer to electrons in the material are large enough for them to be treated as free. Shulek *et al*[113] improved the calculation by including binding effects of the atomic electrons. The distribution of energy loss ϵ derived by Shulek can be expressed as the convolution of a Gaussian component with the Landau-Vavilov distribution:

$$f_S(\epsilon, \xi) = \frac{1}{\sqrt{2\pi\delta_2}} \int_{-\infty}^{\infty} d\epsilon' f_{LV}(\epsilon', \xi) e^{-\frac{(\xi-\epsilon')^2}{2\delta_2}} \quad (3.5)$$

where ξ is the mean energy loss in the Gaussian (Bethe-Bloch) limit. $f_{LV}(\epsilon, \xi)$ is the Landau-Vavilov distribution. It’s mathematical form is not particularly illuminating (cf. Appendix B); it is characterized by a significance parameter $\kappa = \xi/T_{max}$ and a ‘most-

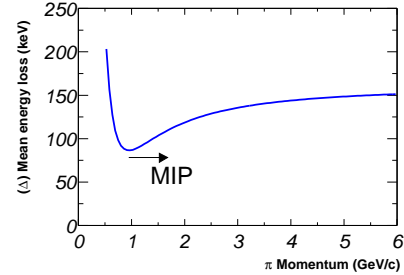


Figure 3-6: Mean E_{loss} for π 's in Si from Bethe-Bloch equation incorporating δ -rays[109]

²Due to the aforementioned limit of infinite energy loss allowed in a single collision, the average value obtained from a Landau distribution is also infinite!

probable' energy loss which represents the peak of the distribution. In the $\kappa \rightarrow 0$ limit, the distribution tends to the Landau distribution, and as $\kappa \rightarrow \infty$, it approximates a Gaussian. δ_2 is the Shulek correction parameter which can in principle be calculated[114] with knowledge of the electronic shell structure of the absorbing material. It depends on the momentum, mass and charge of the incident particle, and has been measured in a PHOBOS testbeam experiment for π 's and K 's. A parametrized form of these measurements is used in the simulation.

The GEANT simulation uses the Landau-Vavilov distribution to assign energy losses to charged particles as they traverse the apparatus. A particle- and momentum-dependent parametrization of the Shulek correction is added to the energy loss. To this extent, GEANT simulates the energy deposited in an 'ideal' detector. Two practical limitations of this idealized simulation are a) finite step size while tracking particles in the large volume: care has to be taken to ensure that the step size is small enough to ensure adequate sampling accuracy and b) a low momentum cut-off in tracking charged particles: as the particles progressively lose energy during their passage, at low momenta ~ 100 keV/c the above calculations are no longer valid. The systematics of how this low-momentum cutoff affects the accuracy of the simulations and the multiplicity measurement are described in a subsequent chapter.

To connect this ideal simulation to the real-world detector performance, the GEANT output is augmented with detector-specific electronics noise in a procedure referred to as 'smearing'. Effectively, the inverse of Eqns(3.3,3.2,3.1) is applied to the energy deposited in each readout pixel of the silicon detectors, to obtain the simulated response in ADC units. Gaussian noise with width equal to the measured noise of each channel is added to the signal, and the response scaled according to the channel's measured gain. Common mode shifts are not applied to the simulated signal. Any channel with ADC response greater than 4095 (the maximum of 12-bit range) is set to 4095. Once the simulated output has been de-calibrated in this manner, the same calibration procedure is reapplied as in the case of signal processing of real detector signals described above. Channels with known bad noise or gain values are masked out.

Fig. 3-7 overlays the simulated energy loss distribution obtained from the GEANT+smearing procedure with the one measured in a multiplicity detector module as seen in Fig. 3-5. The pedestal peak has been suppressed for clarity (the simulation uses the the same pedestals as the data), and the simulated distribution has been scaled such

that the most-probable values of the distributions coincide. This scaling takes care of the residual uncertainty in the absolute calibration of the data. The agreement in the widths of the distributions and the locations of secondary peaks from double hits in the same pad is very good. The GEANT detector simulation and smearing procedure together provide an excellent representation of the detector response.

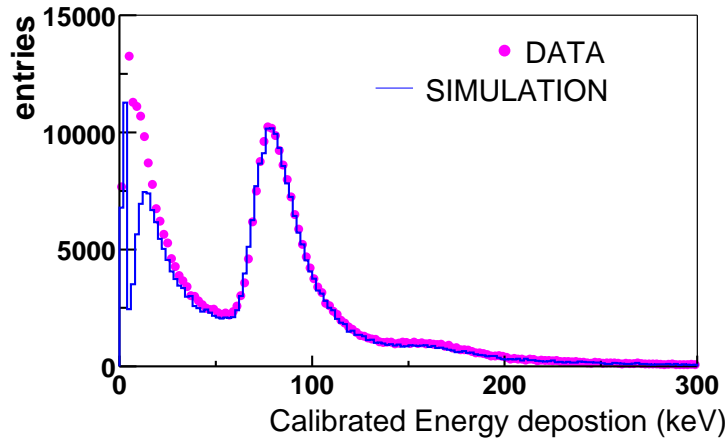


Figure 3-7: Comparison of energy loss spectrum in data and GEANT simulation. The dots indicate the same data as in Fig. 3-5. The lines are the simulated distribution including “smearing” to fold in the electronics response.

3.2.2 Trigger detector simulation

The paddle scintillators provide primary triggering for the experiment and a measure of the centrality or impact parameter of collisions. Both timing and pulse height information from these detectors is used, and therefore the response of these detectors needs to be well understood in the simulation.

As described in the previous chapter, each paddle counter’s geometrical acceptance is large, so a significant number of particles can traverse one scintillator. The photomultiplier tube attached to the scintillator generates a signal proportional to the scintillation light which is then amplified and digitized by a 12-bit ADC. The calibration procedure used to match the relative gains of the different photomultiplier tubes is slightly different from the one used for the silicon detectors. The relative gains of the tubes were determined *in situ*, by examining the signal distribution in data runs. By matching the pronounced 1-MIP peaks among the different paddle scintillators, relative gain factors were obtained. An approximate absolute calibration was also done in the pre-installation phase using a

collimated radiation source which yielded a relation of $1\text{-MIP}_{paddle} = 1.64 \text{ MeV}$ energy loss in the scintillator bulk[89]. The time matching between the signals was simply achieved by using pulsers and adjusting the cable lengths to ensure equal delays.

The GEANT simulation provides the energy deposition of single particles traversing the scintillators using the Landau-Vavilov distribution with parameters adjusted for the scintillator plastic. The light response of the photomultiplier tube is modelled by summing the energy losses of all particles traversing the corresponding slat and “de-calibrating” it into an ADC response:

$$ADC_{paddle} = \frac{\sum_{particles} E_{loss}}{MIP_{paddle}} * Gain_{paddle} + Noise_{paddle} \quad (3.6)$$

The noise is assumed to be Gaussian with a width of 10 ADC units. The total energy deposited in the slat is required to exceed 0.5 MIP’s, to match the discriminator energy cut-off used in the real detector to prevent triggering on noise. At the other extreme, if ADC_{paddle} exceeds 4095 for any paddle, it is set to 16383, indicating overflow as seen in the data.

The timing for each paddle detector is also simulated by assigning it to the scintillator hit by the particle(s) with the fastest traverse time. A Gaussian jitter is added to the timing, and the value is digitized to simulate the 25 ps timing resolution of the TDC’s used to measure the timing.

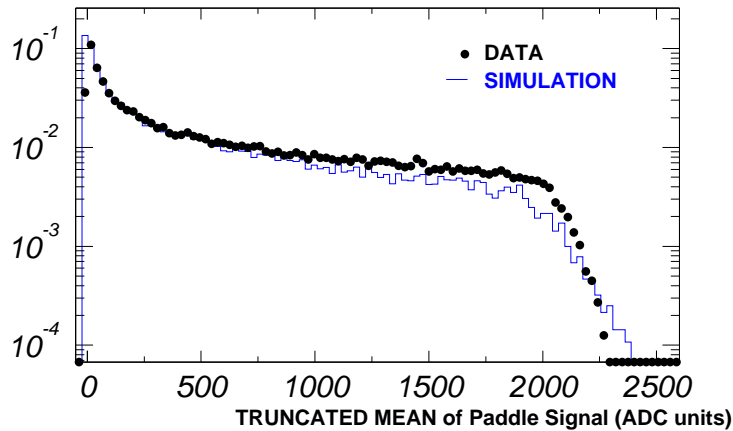


Figure 3-8: Comparison of the truncated mean paddle response in ADC units, between data and simulation for $\sqrt{s_{NN}} = 200 \text{ GeV}$ collisions triggered with the minimum-bias trigger.

Fig. 3-8 shows a comparison of the simulated trigger response to the measured one. A

truncated mean of signals in ADC units from the paddles on each side of the interaction region is used to exclude overflows and fluctuations from long Landau tails. Unfortunately, due to the large acceptance of the paddles, the simulated response depends significantly on the assumptions of number of charged particles hitting the detector. In this case, the HIJING model has been used to simulate particle production in Au+Au collisions; the produced particles are propagated through the detector volume using GEANT. In relating the measured mean paddle response to the *a priori* known impact parameter of the simulated collision, this model dependence is a source of systematic uncertainty as described in the following chapter.

Chapter 4

Event selection and Centrality determination

The PHOBOS trigger detectors serve a dual purpose: signalling the DAQ to start detector readout when a collision occurs, and providing an estimate of collision centrality. Both these functions are discussed in detail in the following sections. Apart from an online trigger selection to reject beam-gas related background events, the only other criterion used to select events for analysis is a valid reconstructed vertex, which is also described below.

4.1 Minimum bias trigger

Fig. 4-1 shows the logical layout of the PHOBOS trigger system. Timing and pulse height information from the paddle scintillators is used to trigger on ‘physics’ events: inelastic collisions of Au+Au ions near the nominal PHOBOS vertex position. The trigger logic has been designed to minimize any bias in selecting such collisions. A general feature of the design is to make realtime trigger decisions based solely on the timing information - all information regarding the pulse heights is stored for offline analysis.

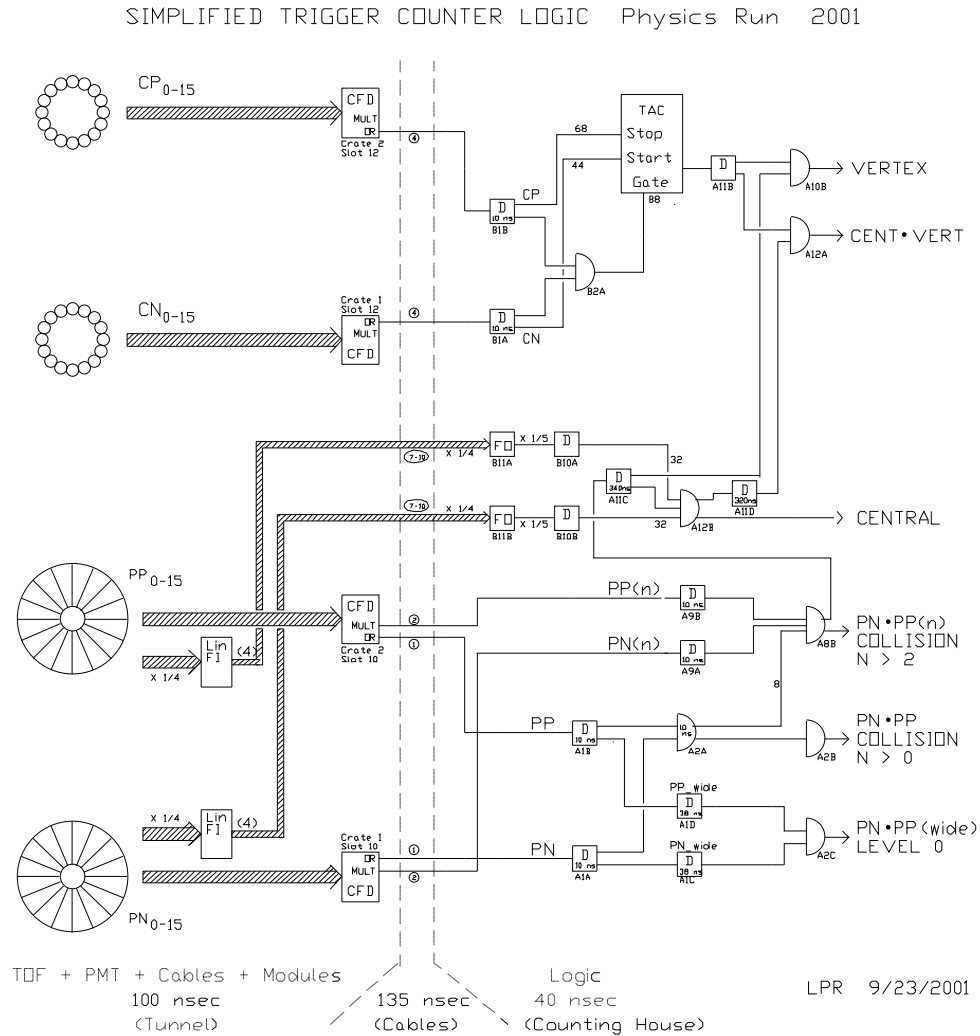


Figure 4-1: PHOBOS trigger logic: Relevant triggers PP.PN, PP.PN_{narrow} and PP(2).PN(2)_{narrow} are discussed in detail in the text. Cerenkov detectors provide a trigger sensitive to the vertex position with a coarse resolution of 5 cm. Additional fast scintillators (T0 counters) were installed for PR01 to provide a finer online vertex resolution and start-timing for the TOF detectors. The Cerenkov and T0 detectors were not used for the data presented here.

Signals from the 16 paddle scintillators on either side of the interaction vertex (P and N) are applied to constant fraction discriminators (CFD) set to a threshold of 0.5 MIP to reject noise. A ‘hit’ in at least one of the paddles on each side within a 76 ns time window produces a PP.PN trigger. This Level-0 trigger captures Au+Au collisions as well as background events caused by beam-gas interactions. The scintillators have equal response to incident charged particles from both sides; a beam gas interaction in the $\pm \hat{z}$ direction outside the the interaction region produces a ‘spray’ of particles that hit one set of paddles from behind, and

after 22 ns, the opposite set. The rate of these beam-gas type triggers is primarily dependent on the intensity of beams circulating in RHIC, while the collision triggers scale with the luminosity. In initial running periods, the `PP.PN` Level-0 trigger provided a vital diagnostic in calibrating the timing and signal response of the scintillators. For physics data-taking during high luminosity runs, this trigger was scaled down significantly to minimize DAQ dead-time.

A narrower coincidence of the CFD OR'ed output `PP.PNnarrow` rejects a large fraction of the background: only particles originating near the interaction region can fire this trigger. Since the time of flight from nominal $z = 0$ to the paddle detectors is 10.5 ns, and the time resolution of the CFD OR'ed output is 2 ns[89] a narrow coincidence window of 8 ns was chosen to capture collision-type events originating over a broad range of $\sim |z| < 2.5$ m.

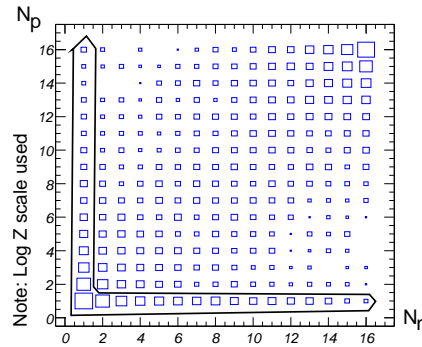


Figure 4-2: N v/s P side distribution of number of ‘hit’ paddle scintillators in a data run with `PP.PNnarrow` as primary trigger. Asymmetric events are rejected by requiring the `PP(2).PN(2)narrow` trigger

Analysis of early data showed that a large fraction of events captured by the `PP.PNnarrow` trigger had a peculiar P-N asymmetry: only one paddle on one side registered a hit, while a large number of paddles on the opposite side were hit (Fig. 4-2). Signals recorded in the silicon pixel detectors for the corresponding events yielded no discernible vertex, and the zero degree calorimeters (ZDC’s) didn’t provide any timing or energy information for such events. A tentative hypothesis is that these events are triggered by beam ‘halo’ particles travelling around RHIC in phase with the Au ion bunches, depositing large energy in one set of paddles in random coincidence with single hits in the opposite set. Although the rate of asymmetric events increases in proportion to the beam intensity lending some credibility to this hypothesis, it was not verified directly.

Requiring at least *two* paddles on each side to be hit within the same narrow coincidence window ($PP(2) \cdot PN(2)_{narrow}$ trigger), such uninteresting events can be excluded. This also excludes ultra-peripheral Au+Au collisions that fire only one paddle scintillator on each side; so care needs to be taken in estimating the fraction of cross section lost. This is discussed further in the following section on centrality determination. All data presented in this thesis have been recorded with $PP(2) \cdot PN(2)_{narrow}$ as the primary Level-1 trigger, with $PP \cdot PN_{narrow}$ being scaled down by 8 at Level-1.

4.1.1 Offline cuts

Since timing and signal information from the paddle detectors and ZDC's is digitized and recorded in the data, it is possible to apply offline cuts to further reject background events, as listed below:

1. Fig. 4-3 shows the distribution of the time difference between the earliest hit paddle on each side of the interaction region ($\delta t = |t_{Pd}^N - t_{Pd}^P|$). Clear peaks around $\delta t \sim \pm 22$ ns from beam-gas interaction triggers and around $\delta t \sim 0$ ns from collision events can be distinguished. δt provides a crude estimate of the collision vertex (with $\sigma_z \sim 30$ cm), so requiring $\delta t < 4$ ns rejects events with vertices beyond $z \sim \pm 1.2$ m that are well outside the acceptance of the silicon detectors.

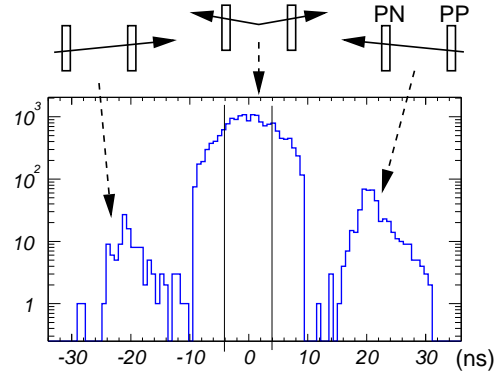


Figure 4-3: Distribution of δt_{Pd}

2. The anti-correlation between signals from ZDC's and paddle detectors is shown in Fig. 4-4a. For increasingly central collisions involving large overlap of nuclei, there are few spectators and hence forward going neutrons leading to small signal in the ZDC. This is accompanied by large signal in the paddles due to higher charge particle production. For very peripheral collisions however, most of the spectator matter produces massive charged fragments that are swept away from the aperture of the ZDC's, causing the distribution of ZDC signals to turn over. There is a class of events (highlighted in Fig. 4-4a) which does not obey this relationship. Closer analysis of the timing from ZDC modules for these events (Fig. 4-4b) and the lack of any discernable vertex tracks in the silicon detectors indicates them to be beam-gas background events. They can be cleanly rejected by requiring good timing for

the ZDC's restricted to a narrow region around $t_{zdc}^N \sim t_{zdc}^P \sim 600$ ns (Fig. 4-4b).

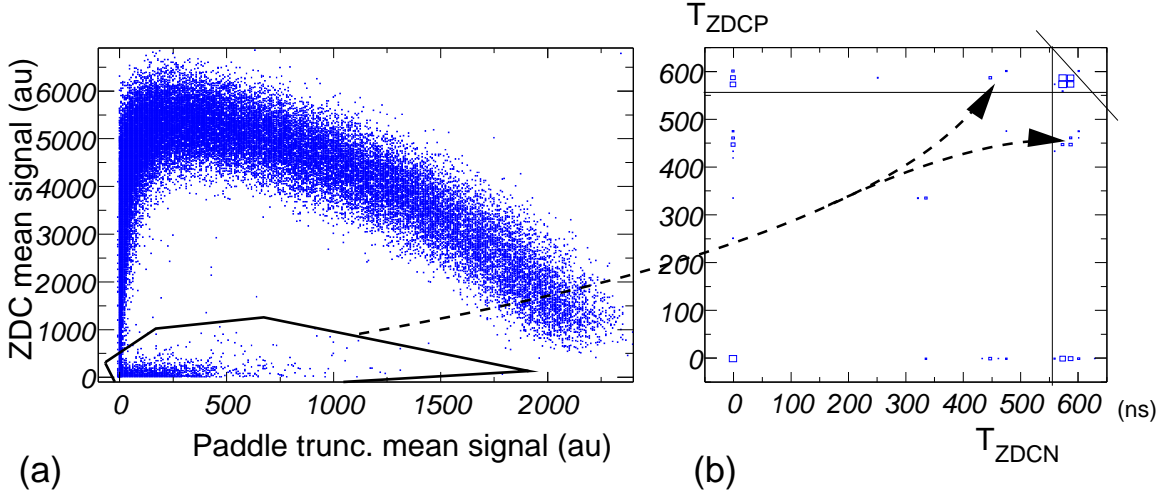


Figure 4-4: a) Correlation between mean signals from the ZDC and paddle detectors with no offline cuts applied. b) Correlation of timing from the positive and negative ZDC modules. The lines correspond to the GoodZDCTiming cut explained in the text

3. The ZDC timing cut applied above is suitable for rejecting beam-gas backgrounds, but if used by itself, it biases the data by rejecting very central collisions which do not have many neutrons going forward. Large energy deposition in the paddle scintillators for central collisions is OR'ed with the ZDC cut to remove this bias.

The following table summarizes the aforementioned offline cuts. The numbers shown are different for the data sets at two energies due to different calibrations of the electronics.

Trigger Cut Name	Value for $\sqrt{s_{NN}} = 130$ GeV	Value for $\sqrt{s_{NN}} = 200$ GeV
GoodPaddleTiming	$ t_{Pdl}^N - t_{Pdl}^P < 4ns$	$ t_{Pdl}^N - t_{Pdl}^P < 4 ns$
GoodZDCN	$t_{zdc}^N > 552 ns$	$t_{zdc}^N > 520 ns$
GoodZDCP	$t_{zdc}^P > 560 ns$	$t_{zdc}^P > 520 ns$
GoodZDCSum	$(t_{zdc}^P + t_{zdc}^N) < 1240 ns$	$(t_{zdc}^P + t_{zdc}^N) < 1240 ns$
GoodZDCTiming	(GoodZDCP · GoodZDCN · GoodZDCSum)	
VeryCentral	$PdlSum^P > 2500 \cdot PdlSum^N > 2500$	$PdlSum^P > 1500 \cdot PdlSum^N > 1500$
Collision	GoodPaddleTiming · (GoodZDCTiming + VeryCentral)	

Table 4.1: Summary of cuts applied in offline analysis to select “collision” events. (·) signifies logical AND, (+) signifies logical OR

4.2 Centrality determination

There are two reasons for categorizing events by their centrality, loosely defined as the geometrical overlap of the two colliding nuclei whose centers are separated by ‘impact parameter’ b :

For the $dN_{ch}/d\eta$ analysis presented in the following chapter, it is important to separate events into classes that exhibit roughly equal detector occupancy¹ in each class. By definition, detector occupancy scales with the total number of charged particles traversing the detector which in turn, depends monotonically on the impact parameter: greater overlap implies increased particle production.

Secondly, in order to interpret $dN_{ch}/d\eta$ distributions as described in chapter 1, it is useful to express the results as a function of the number of participating nucleons (N_{part}). Although the ZDC’s were originally designed to indirectly measure N_{part} by counting the forward-going spectator neutrons, in practice this turned out to be unfeasible. As seen in Fig. 4-4a, signal response of the ZDC’s is double-valued due to most of the charged fragments in peripheral collisions being swept away from the ZDC’s by the DX magnets. In addition, detailed simulation studies performed on the response of the ZDC’s[46] indicated that the resolution of the signals was not sufficient to allow reliable event classification based on the response of the ZDC’s alone: the errors grew dramatically for peripheral collisions, reaching up to 40% in the lowest usable bin. It is thus necessary to consider another quantity that monotonically tracks the collision geometry (and therefore N_{part}).

The truncated mean of signals from the paddle detector modules provides a suitable variable that can be translated into N_{part} by simulation. The energy loss in a thin scintillator has large tails, following a Landau distribution. Due to the large acceptance of individual paddles, it is also quite likely to register multiple charged particles in each, leading to larger signals and possibly even saturation. The effect of long tails on estimating the average energy loss can be avoided by selecting only 12 lowest of the 16 signals on each side and averaging them. This quantity is called the *truncated mean* and used as the main estimator of collision centrality.

¹‘Occupancy’ is defined as the fraction of pads that have a signal above the noise threshold

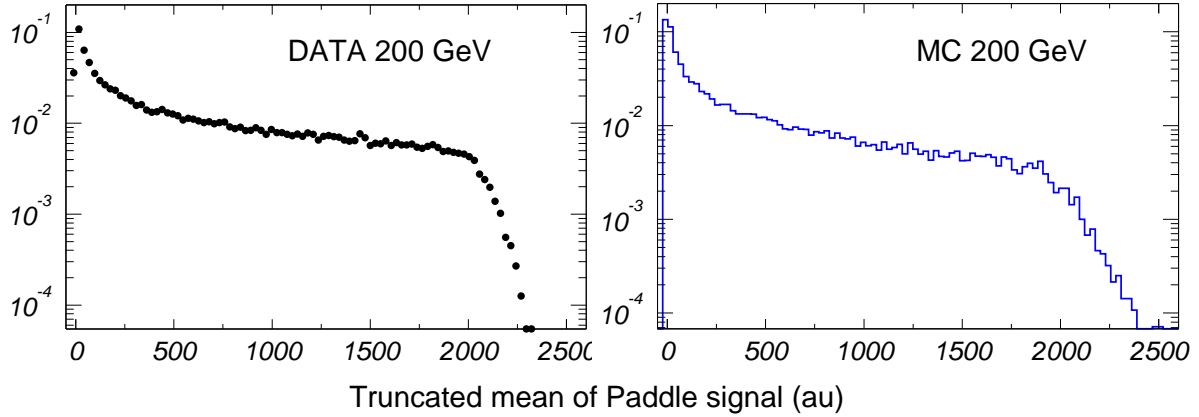


Figure 4-5: Distribution of truncated means of signals from paddle detectors. Data(a) and MC(b) have been normalized to same total number of events.

Fig. 4-5a shows a normalized distribution of the truncated mean of signals from the paddle scintillators for all events collected at $\sqrt{s_{NN}} = 200$ GeV. The characteristic shape of the distribution results from the dependence of the differential cross section on geometric overlap of the colliding nuclei[115]. For the purpose of event classification, it is sufficient to integrate this distribution (accounting for the ‘missing’ cross section at ultra-peripheral events), and divide the ensemble into ‘slices’ or centrality ‘bins’ populating each bin with approximately equal number of events.

The number of participants in a collision N_{part} is estimated from the simulated distribution of the paddle signal truncated mean as shown in Fig. 4-5b. The Monte Carlo (MC) simulation process has been described earlier in chapter 3. For MC events, N_{part} is known *a priori*, so assigning an $\langle N_{part} \rangle$ to each centrality slice would be straight-forward if the distributions for data and MC were alike. The problem is that these distributions are similar, but not alike. Although every effort has been made in the MC to model the response of individual paddle scintillators by convoluting the ideal deposited energy with detector noise and calibrations, there remains the underlying assumption of the number of charged particles produced as a function of b specific to the model used: HIJING. As pointed out below, the errors on the estimation of N_{part} are composed from both the ‘smearing’ procedure and the model assumptions. The dominant source of error, however, turns out to be the estimate of missing cross section.

4.2.1 Trigger efficiency and the ‘missing’ cross section

Ultra peripheral collisions producing a small number of charged particles fail to satisfy the $PN(2) \cdot PP(2)_{narrow}$ trigger requirement leading to a trigger inefficiency for such collisions. It is possible to estimate this efficiency by comparing the truncated mean distributions for data and MC (Fig. 4-5a,b) to account for the missing cross section at low paddle signal.

To accomplish this in a more or less model independent manner, a much simpler approach is adopted. A ‘hit’ paddle is defined as one with at least one particle traversing it and depositing a signal above the noise threshold (set at 0.5 MIP for data and MC). Then the distribution of $(N_n + N_p)$, the number of hit paddles on both sides of $z = 0$, can be used to compare data and MC, without worrying about the detailed scintillator response or the model assumptions on number of charged particles produced. This distribution is demonstrated in Fig. 4-6 for data and MC. The two distributions are normalized by scaling the plateau region between $(N_n + N_p) = 17$ and 22. For MC events, a ‘simulated’ trigger of $N_n \geq 2 \cdot N_p \geq 2$ provides an equivalent ensemble to the data distribution.

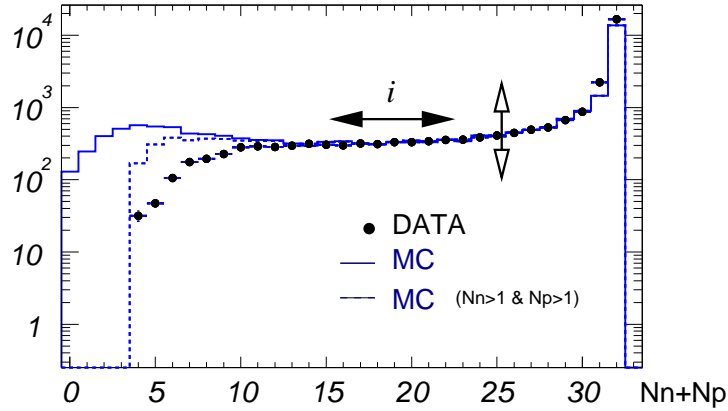


Figure 4-6: Distribution of number of hit paddles $(N_n + N_p)$ for data and MC (Shaded area = δI)

If the area under the data and MC histograms from 0 up to a bin i ($17 < i < 22$) is denoted as I_{DATA}^i and I_{MC}^i respectively, then the difference $\delta I = I_{MC}^i - I_{DATA}^i$ provides an estimate of the trigger efficiency:

$$\epsilon = \frac{I_{DATA}^{full}}{I_{DATA}^{full} + \delta I}$$

where I_{DATA}^{full} denotes the full integral of the data distribution proportional to the uncor-

rected cross section.

Using this procedure, the trigger efficiency ϵ was determined to be $(86\pm 3)\%$ for the $\sqrt{s_{NN}} = 130$ GeV data set, and $(88\pm 3)\%$ for the $\sqrt{s_{NN}} = 200$ GeV data set. The systematic error of 3% on ϵ was estimated by varying i , the upper limit of integration, and the normalization of the data and MC distributions.

4.2.2 Determination of $\langle N_{part} \rangle$ and error analysis

The simulated paddle truncated mean distribution shown in Fig. 4-5b, is divided into 18 slices containing approximately equal number of events per slice, *i.e.*, fractions of the total cross section. Fig. 4-7a,b demonstrates the top five of these 18 centrality ‘bins’ for clarity. The data distribution, after correcting for the missing cross section due to trigger inefficiency, is also divided into the corresponding 18 centrality bins. For MC, N_{part} is an input to the simulation. Fig. 4-7c shows the distribution of N_{part} for events belonging to each centrality bin in the MC. Based on this, a mean number of participants $\langle N_{part} \rangle$ can be assigned to each centrality bin as listed in Table 4.2

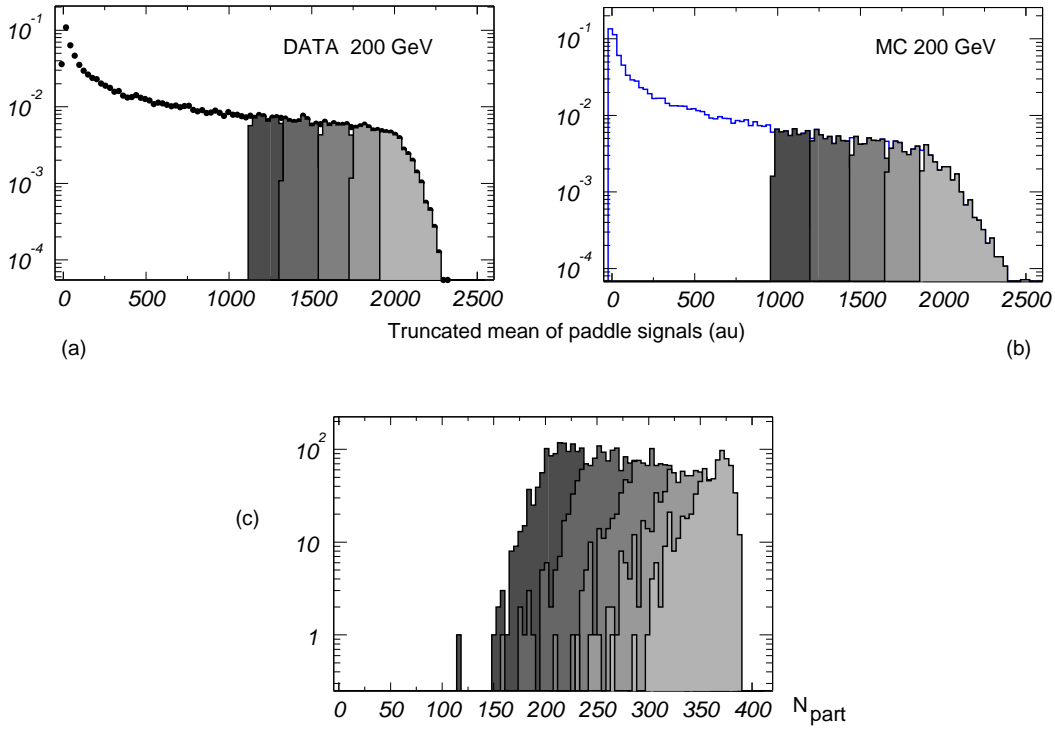


Figure 4-7: Distribution of truncated mean of paddle signals for data(a) and MC(b), with top five centrality bins shown. c) N_{part} distribution for each corresponding centrality bin

Bin	% of σ_{tot}	$\langle N_{part}^{130} \rangle$	$\langle N_{part}^{200} \rangle$	
0	80%-100%	4.1±0.8	4.1±0.8	(Most Peripheral)
1	75%-80%	9.7±1.4	10.7±1.4	
2	70%-75%	14.3±1.8	15.3±1.9	
3	65%-70%	20.3±2.3	21.1±2.3	
4	60%-65%	27.9±2.8	28.9±2.9	
5	55%-60%	37.0±3.3	38.7±3.3	
6	50%-55%	48.8±3.8	50.5±3.9	
7	45%-50%	63.1±4.2	65.3±4.2	
8	40%-45%	79.8±4.6	83.1±4.6	
9	35%-40%	99.8±4.8	102.7±4.9	
10	30%-35%	122.1±5.0	124.4±5.0	
11	25%-30%	148.4±5.0	152.2±4.9	
12	20%-25%	178.9±4.7	182.7±4.6	
13	15%-20%	213.6±4.2	216.5±4.2	
14	10%-15%	254.0±3.3	255.9±3.2	
15	6%-10%	295.3±2.5	297.7±2.5	
16	3%-6%	329.6±1.8	330.6±1.7	
17	0%-3%	355.5±5.4	358.4±5.4	(Most Central)

Table 4.2: Centrality bins with their corresponding percentage cross-sections and $\langle N_{part} \rangle$ for two energies. The systematic errors are discussed in the text

The systematic error on assigning $\langle N_{part} \rangle$ to centrality bins in the data arises from three independent sources:

(1) **Trigger Efficiency:** The effect of uncertainty in the efficiency ϵ of the trigger on the calculated $\langle N_{part} \rangle$ was studied by using simulations. The total cross section used in MC was deliberately underestimated by 1%, 3% and 6% to reflect the 3% uncertainty on ϵ . Practically, this is realized by lowering the percentage bin in column 2 of Table 4.2 by 1%,3%,6% and computing the error in $\langle N_{part} \rangle$ of the resulting centrality bins. Fig. 4-8 shows the percentage error in calculating $\langle N_{part} \rangle$ when underestimating the cross section, as a function of the true number of participants. The error is quite large (up to 20% for the most peripheral data), and decreases with increasing centrality since N_{part} is bounded from above.

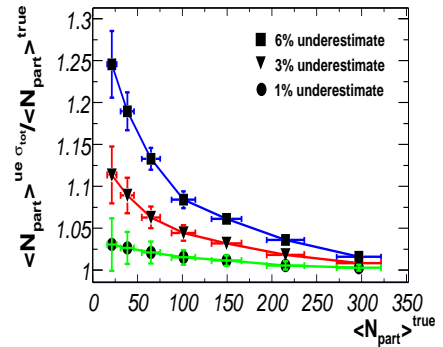


Figure 4-8: Effect of underestimating the total cross section on the error in $\langle N_{part} \rangle$

(2) Simulation of paddle scintillator and electronics response:

The simulated paddle mean distribution (Fig. 4-7) used to arrive at $\langle N_{part} \rangle$ is subject to the details of modeling the scintillator and photo-multiplier electronics response. Fig. 4-9 demonstrates the relative difference between the number of participants obtained from this ‘smeared’ distribution and the true $\langle N_{part} \rangle$ encoded in the simulated events. The true $\langle N_{part} \rangle$ per centrality bin can be calculated by binning the total cross section in percentage slices of N_{part} rather than percentage slice of smeared paddle mean. The smeared result slightly overestimates the number of participants for peripheral events: Gaussian noise tends to push events into higher centrality classes. At the other extreme of central collisions, it underestimates the true number of participants due to the upper bound on N_{part} . This systematic deviation of $\langle N_{part} \rangle$ determined after the smearing procedure from the true $\langle N_{part} \rangle$ values, instead of being corrected (the correction would be model dependent), is included as a source of systematic error in the estimation of $\langle N_{part} \rangle$.

(3) Model assumptions: The third and least understood component of the systematic error on N_{part} is the role played by assumptions of the underlying model of particle production (HIJING). Fig. 4-10 shows the $\langle N_{part} \rangle$ values obtained from two different event generator models VENUS[72] and RQMD[70] for commensurate centrality slices. Since these models assume a total cross section of Au-Au collisions that is quite different from the one observed in data (which HIJING approximates to some extent Fig. 4-5), this last comparison was not used while combining systematic errors.

To summarize, the first two errors listed above are added in quadrature per centrality bin and listed as the systematic error on $\langle N_{part} \rangle$ in Table 4.2.

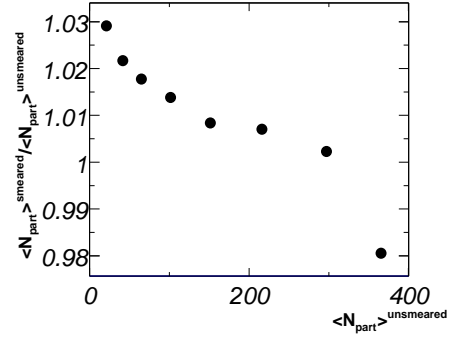


Figure 4-9: Effect of smearing of paddle signal response on error in $\langle N_{part} \rangle$

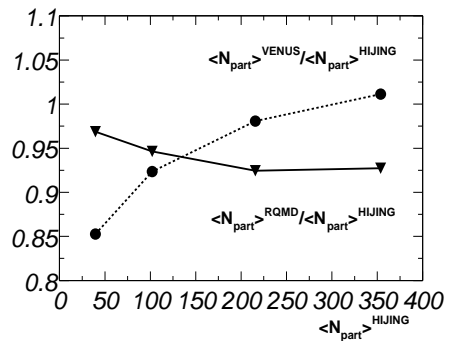


Figure 4-10: Ratios $\langle N_{part} \rangle$ values obtained from VENUS and RQMD compared with HIJING

4.3 Vertex reconstruction and selection

Apart from online and offline trigger cuts, the only other criterion used to select events for analysis is the reconstruction of an event vertex. The resolution of the reconstructed vertex feeds directly into the pseudo-rapidity η of reconstructed hits in the analysis presented in subsequent chapters, so rather strict constraints are placed on vertex reconstruction while ensuring that these constraints don't introduce undue bias in the event selection.

The trigger cuts outlined previously provide us with an ensemble of events with collision vertices over a broad range $-60 \text{ cm} < z < 60 \text{ cm}$. Five vertex reconstruction algorithms employing four silicon sub-detectors are used to calculate $(x_{vtx}, y_{vtx}, z_{vtx})$. These include the dedicated vertex detector, the first 6 planes of the spectrometer arms, the octagon detector itself and the paddle detector timing. Using multiple methods for vertex reconstruction provides a very useful cross-check for the consistency of the calculations in regions where the acceptance of the different sub-detectors overlap, and also serves to extend the total detector acceptance over which vertex reconstruction is possible.

Details of these algorithms can be found elsewhere[46]; their general design is based around pattern recognition of clusters of hit pads and correlation of these clusters to form tracks pointing back to a unique space point. The resolution of the reconstructed vertex in each spatial dimension is governed primarily by the segmentation of the sub-detector's pads in that dimension. The vertex detector consists of pads finely segmented along \hat{z} (typical pad size is $2.4 \text{ mm}(\hat{z}) \times 19 \text{ mm}(\hat{x})$ with 4 planes in the \hat{y} direction) and provides excellent $\sigma_z \sim 80 \mu\text{m}$, reasonable σ_y and poor σ_x over $|z_{vtx}| < 20 \text{ cm}$. The first few planes of the spectrometer have typical pad sizes of $1 \text{ mm} \times 1 \text{ mm}$ arranged in the $\hat{x} - \hat{z}$ plane oriented along \hat{y} farther away from the collision vertex. They provide $\sigma_x, \sigma_y, \sigma_z \sim 300 \mu\text{m}$ over a much larger range $-40 \text{ cm} < z_{vtx} < 10 \text{ cm}$. The vertices obtained from the octagon and paddle detectors have much coarser resolutions, albeit over the full $|z_{vtx}| < 60 \text{ cm}$ range, and are only used as a rough cross-check or for special studies like alignment of the other silicon detectors.

The results of the different vertexing algorithms are combined on an event-wise basis to form a composite 'best guess' vertex called *RMSSelVertex*. The event-wise analysis compares the different calculated vertices for consistency based on the known resolutions of each algorithm for each dimension and assigns them quality factors. These factors

have been obtained from an MC simulation with a known true vertex. Each vertexing algorithm is run on simulated events containing signals in the sub-detectors convoluted with noise and required to reconstruct the vertex. This provides a training set for the RMSSelVertex analysis module. In its learning mode, the RMSSelVertex module checks each returned vertex for consistency with the true vertex within the allowed resolution of each algorithm. Quality factors are calculated using all vertex pair combinations in each spatial dimension, taking into account the difference between the reconstructed and true vertex. In this manner, the RMSSelVertex analysis is able to achieve resolutions of $\sigma_x = 248 \pm 4 \mu m$, $\sigma_y = 182 \pm 2 \mu m$, $\sigma_z = 81 \pm 1 \mu m$.

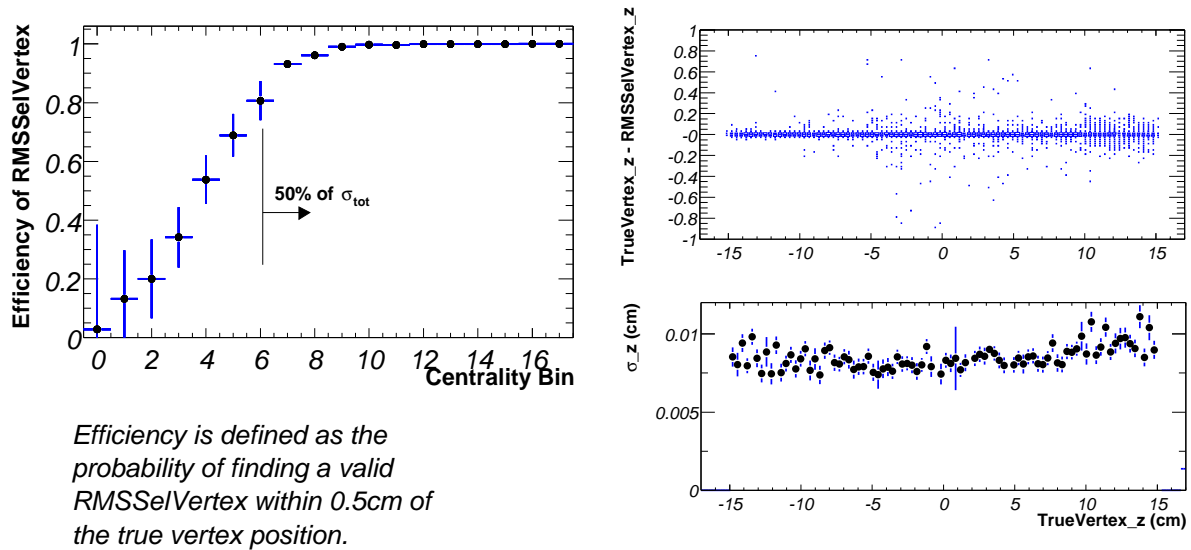


Figure 4-11: a) Efficiency of RMSSelVertex as a function of centrality bin b) σ_z of RMSSelVertex as a function of z_{vtx}

The value returned by RMSSelVertex is used for the analysis presented in the following chapters. It is important that this strict vertexing procedure does not reject events having too few or too many hits or tracks where the different algorithms may be inefficient. The RMSSelVertex analysis also returns a ‘validity’ flag calculated on the basis of known efficiencies of the algorithms as a function of centrality and vertex position. Only events with a valid RMSSelVertex are accepted for analysis.

Fig. 4-11a shows the efficiency of RMSSelVertex itself at finding valid vertices as a function of centrality bin. The efficiency is nearly constant at 100%, dropping to 85% for peripheral bins due to the small number of tracks in the vertex and spectrometer detectors.

Fig. 4-11b illustrates the resolution σ_z of RMSSelVertex across the range $|z_{vtx}| < 15 \text{ cm}$. It is seen to be nearly constant over $|z_{vtx}| < 10 \text{ cm}$, with a few outliers beginning to appear beyond that range. Based on these figures, a selection criteria of *Valid* $|z_{vtx}| < 10 \text{ cm}$ was applied while selecting events for subsequent analysis. In addition, events in the lowest five centrality bins should be regarded as suspect for multiplicity calculations due to the obvious bias introduced by requiring a valid vertex.

Chapter 5

Determination of charged particle multiplicity

Fig. 5-1 shows a typical distribution of energy in pads of the multiplicity detector in a Au+Au collision. Each pad is color-coded with the energy deposited as calculated from signal processing procedures described earlier in chapter 3. A large number of hits are clustered in the center, near $\theta = 90^\circ$ (*i.e.*, $\eta = 0$), where the density of charged particles is the highest.

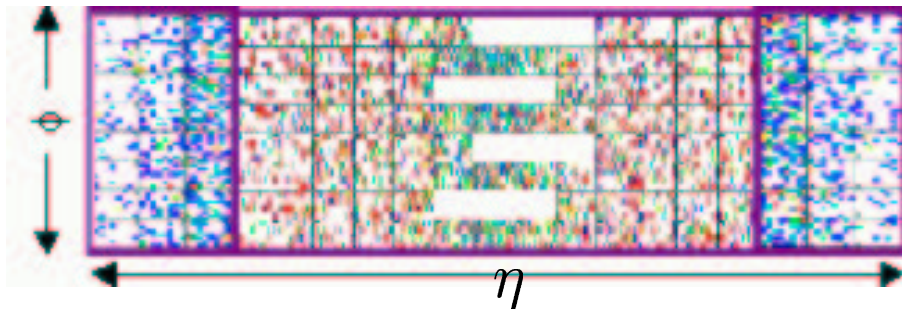


Figure 5-1: Event display of energy deposition in pads of the multiplicity detector.

The data analysis uses statistical methods to convert the observed distribution of hits into a measurement of charged particles traversing the detector as described in the following sections. The main steps involved are: merging of hits to account for energy sharing among pads, correcting for high occupancy and multiple hits-per-pad in the central regions of the detector, and accounting for gaps in the acceptance of the detector. A number of cross-checks and simulations are used to verify the applicability of these procedures.

5.1 Hit Merging

Due to the cylindrical geometry of the octagon detector, a particle traversing a silicon sensor will in general cross the sensor at an oblique angle. Electron-hole pairs created in the silicon by the ionizing particle will be collected on several adjacent pads, with a characteristic relationship of energies measured in each of the pads: the energy in each pad is proportional to the length of the particle's oblique path through the pad (see Fig. 5-2). In order to avoid over-counting hits, it is necessary to correctly reconstruct the deposited energy by merging the energy signals from adjacent pads.

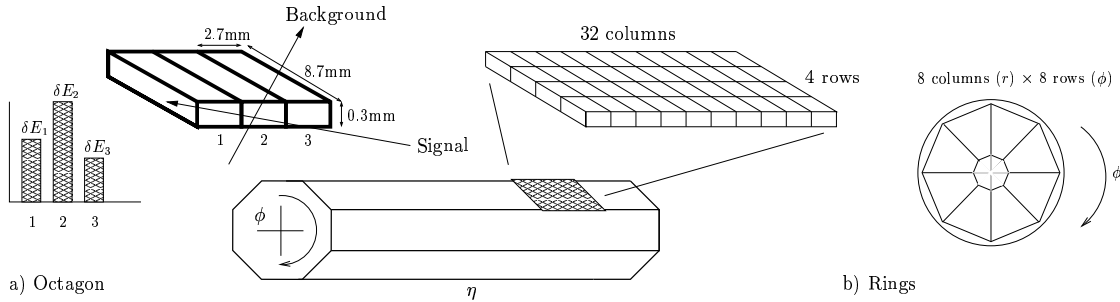


Figure 5-2: Geometry of energy deposition in pads of multiplicity detector

The algorithm developed for hit merging is based on certain common-sense assumptions regarding the geometry of the detector and the straight line paths followed by relativistic charged particles in a magnetic field-free volume. Since each pad of the octagon detector has a profile of $2.7\text{mm} \times 0.3\text{mm}$ and is located approximately 6cm from the beam pipe, a simple geometrical calculation shows that any particle originating at the vertex with an angle of less than $\sim 35^\circ$ to the $+\hat{z}$ axis has more than a 50% probability of traversing multiple pads along a column (the probability of sharing tracks among pads in adjacent rows *i.e.*, along ϕ is negligible). We therefore look for energy-sharing among multiple pads in the octagon detector only for $\theta < 35^\circ$ or equivalently, $|\eta| > 1$. In the mid-rapidity region near $\theta = 90^\circ$, most particles traverse the detector at near normal angles, and the density of hit pads is so high that multiple particles depositing energy in a single pad is the dominant factor. At more oblique angles of incidence, the length of the particles' track through silicon is significantly longer than just the thickness of the pads, leading to proportionately greater energy loss: this needs to be accounted for while merging the energies from adjacent pads. Given a collision vertex, and the known geometry of pads, we can estimate the number of pads a straight-line path at a given angle θ will traverse and use this hypothesis to reject

isolated hits in the outer regions of the octagon. A number of such isolated single-pad hits are observed with energy deposition at the 1 MIP level, with no commensurate shared energy in adjacent pads: these are presumably from secondary particles created in the beampipe directly below the sensor reaching the sensor at normal incidence. At the other extreme, there is a limit on the maximum path length of a track in a given pad (the diagonal of the $2.7\text{mm} \times 0.3\text{mm}$ profile). This gives us a maximum of 3 octagon pads that a particle can traverse before it leaves the sensor's active area - so shared energy is only searched for in groups of 3 pads.

Based on the above logic, the algorithm developed for merging hits is shown in Fig. 5-3. δE_{raw} is the raw energy deposited in a pad, δE_{corr} is the angle and thickness corrected energy. L_{track} is the length of a track originating at a specific z_{vtx} and passing through a given pad, calculated using the known geometry of the pad. L_{track}^{max} is the maximum length a track can have in a given sensor *i.e.*, the diagonal width of a pad.

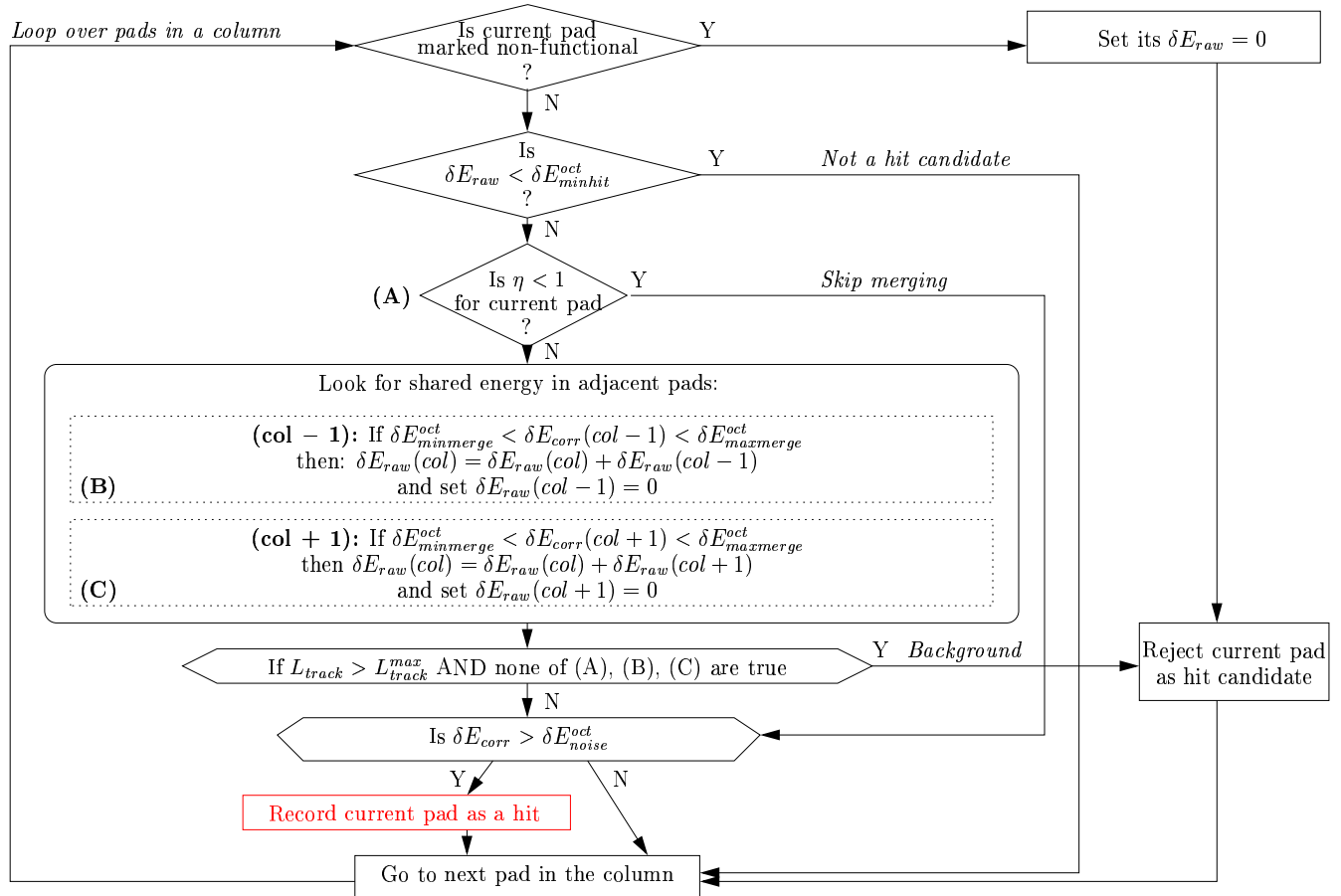


Figure 5-3: Algorithm for merging hits in adjacent pads

For the ring detectors, hits are not merged due to the near-normal incidence of charged particles on the sensors. If a pad registers an energy deposition δE_{raw} greater than a threshold δE_{noise}^{rings} , the pad is recorded as a hit.

In the merging algorithm, $\delta E_{minmerge}^{oct}$, $\delta E_{maxmerge}^{oct}$, δE_{noise}^{oct} , δE_{noise}^{rings} and δE_{minhit}^{oct} are parameters. Suitable values are assigned to these parameters by studying raw energy deposition information in data as follows:

5.1.1 Determination of δE_{minhit}^{oct}

As discussed earlier in chapter 3, the calibrated response of the octagon detectors indicates that a minimum ionizing particle (MIP) traversing a pad at near normal incidence would deposit 87 keV energy in the pad. When looking for a hit candidate in the high- η range where energy sharing among adjacent pads is a near certainty, and given the fact that at most three pads can share the total deposited energy, the cut for δE_{minhit}^{oct} is set at 30 keV, *i.e.*, at approximately $1/3^{rd}$ the value of a MIP's energy deposition. This ensures that pads with energy signals below 30 keV are skipped initially as possible noise (30 keV also happens to be three times the average electronic noise in the multiplicity detector) or as possible shared components of energy in the adjacent pad. Vice versa, pads containing energy signals above 30 keV are regarded as valid hit candidates and a search is performed in adjacent pads on either side in the same column for possible shared energy deposition.

5.1.2 Determination of $\delta E_{minmerge}^{oct}$, $\delta E_{maxmerge}^{oct}$

The two parameters $\delta E_{minmerge}^{oct}$ and $\delta E_{maxmerge}^{oct}$ determine the bounds within which the energy signal in a pad is considered as a shared component of the energy deposited in the adjacent pad. As such, $\delta E_{minmerge}^{oct}$, the minimum bound can be zero, and $\delta E_{maxmerge}^{oct}$, the maximum bound should be determined from the energy in the *adjacent* pad. Practically however, we have to take into account the electronics noise at the lower extreme, and the effect of fluctuations in energy loss at the upper extreme.

Fig. 5-4a shows a distribution of the raw energy signals δE_{raw} as a function of $(z_{pad} - z_{vtz})$ for all pads in the octagon detector. To determine $\delta E_{minmerge}^{oct}$, we need to remove all signals in the highlighted band caused by intrinsic electronic noise and statistical dispersion. A low cut-off of 3σ from the fitted peak around 0 is used to determine $\delta E_{minmerge}^{oct} = 19.5$ keV.

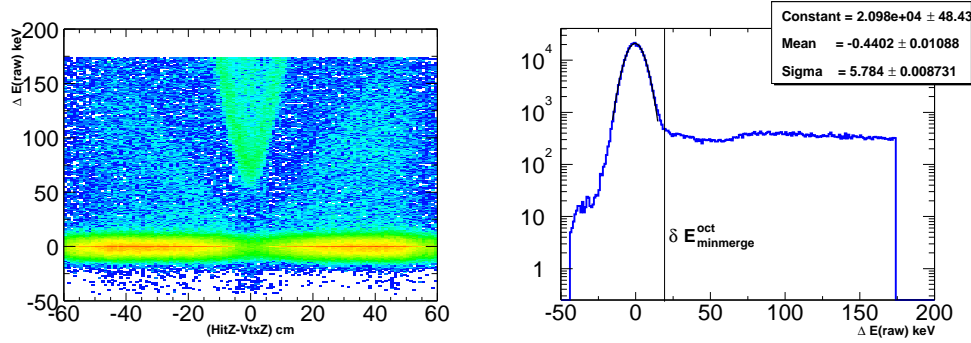


Figure 5-4: a) δE_{raw} distribution for different values of $(z_{pad} - z_{vtx})$. b) Profile of the distribution; the cut for $\delta E_{minmerge}^{oct}$ is shown.

To determine $\delta E_{maxmerge}^{oct}$, we need to look at the distribution of energy signals in single pads' δE_{corr} corrected for angle of incidence and thickness of the sensors as a function η , as shown in Fig. 5-5. In the mid-rapidity region, the separation between the noise peak near 0 on the vertical axis, and the first MIP peak near 87 keV is quite clear, since there is no sharing of the MIP's energy among different pads. Beyond $|\eta| > 1$ however, quite a few pads are observed to have energies uniformly distributed above the noise threshold all the way to the MIP peak position. At the upper end, it is important to place the $\delta E_{maxmerge}^{oct}$ cut such that a good separation is achieved between signals deposited by tracks going into one pad (the main MIP peak) and tracks traversing multiple pads leaving smaller signals in each pad (the 'fuzz' between the noise and the MIP peaks in Fig. 5-5). If this cut is placed too low, double hits coming from the same track will each be counted as single hits, leading to an over-counting of hits.

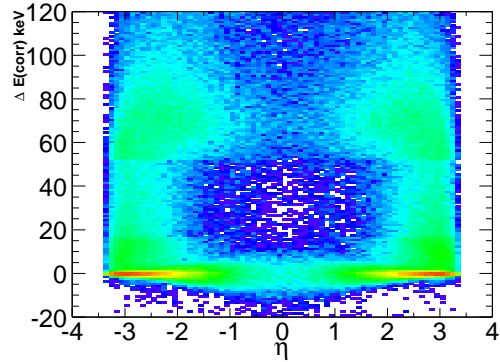


Figure 5-5: δE_{corr} as a function of η (before merging)

It is possible to resolve this issue by studying energy sharing between adjacent pads in the GEANT simulation discussed earlier in chapter 3. Fig. 5-6a,b show the distribution of angle-corrected energy deposition δE_{corr} in the simulation as a function of η for all cases of *unmerged* double hits where a single track traverses two pads. Fig. 5-6a shows the energy δE_1 deposited in the first pad and Fig. 5-6b shows the energy δE_2 deposited in the second pad. Fig. 5-6b shows the sum of the the two energies $\delta E = \delta E_1 + \delta E_2$ which we are

attempting to correctly reconstruct in the measured data (Fig. 5-5). A cut of the type

$$\delta E_{maxmerge}^{oct} = 8.75 \cdot |\eta| + E_0 \quad (5.1)$$

is indicated. The position of the cut on the energy scale (defined by E_0) cannot be ascertained from the simulation because of uncertainty in absolute calibration of energy scale between data and simulation as already discussed in chapter 3.

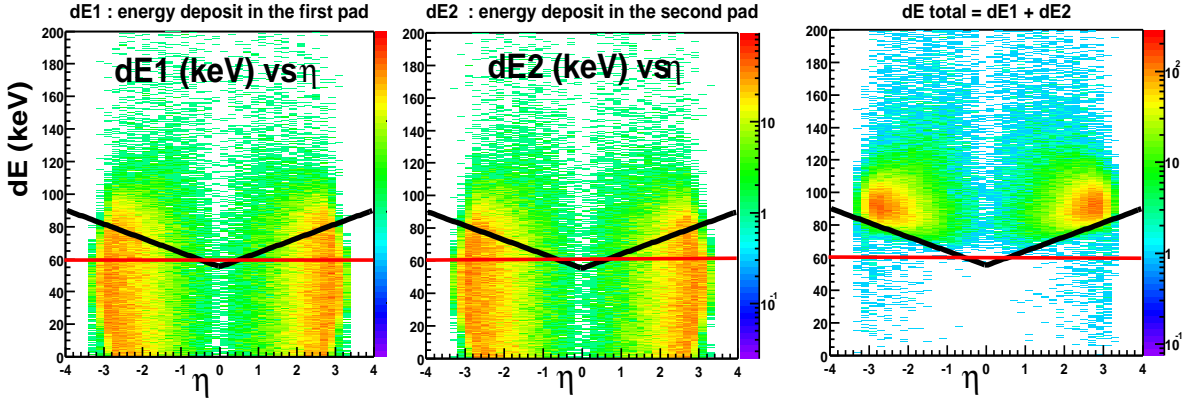


Figure 5-6: Distribution of shared energies in pads for all cases of double hits in the simulation. δE_1 (a) and δE_2 (b) are the energies deposited in the first and second pads respectively. See text for discussion of the cut $\delta E_{maxmerge}^{oct}$

Therefore, to reduce the dependence on calibration constants and the absolute normalization of the simulated hit distribution, the following technique is adopted: E_0 in Eqn. (5.1) is varied over a range from 30 keV (the 3σ noise threshold) to 80 keV (just below the MIP energy deposition), and the number of hits reconstructed from the hit merging procedure in *both* data and simulations using the cut Eqn. (5.1) is plotted as a function of E_0 for various positions along the η axis. Fig. 5-7 shows the variation of N_{hits} in data and simulation for three selected η positions in central events. A quasi plateau region in the middle corresponding to $E_0 \sim 55$ keV for all cases is observed, where the number of reconstructed hits is more or less insensitive to fine variations in the cut value. At the low extreme, the contribution of noise hits causes the count to increase. At the high extreme, we start approaching the single hit MIP peak and the count decreases due to multiple single hits being wrongly combined into a merged hit. Based on this study, a cut of $\delta E_{maxmerge}^{oct} = 8.75 \cdot |\eta| + 55$ keV was decided upon for the hit merging procedure.

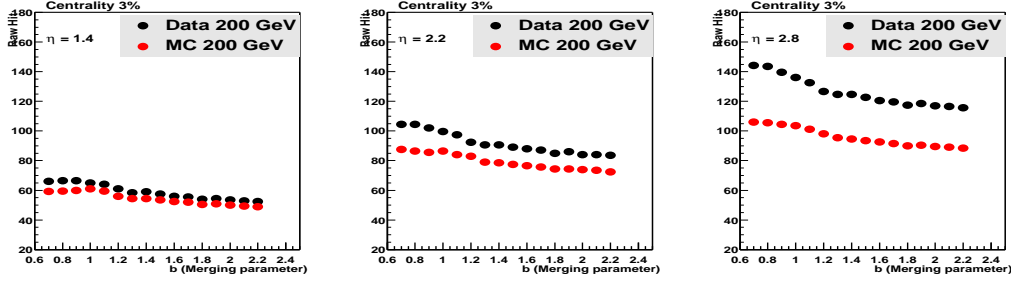


Figure 5-7: Variation of N_{hits} reconstructed in data and simulations at $\eta = 1.4$ (a), 2.2 (b) and 2.8 (c) in central events as E_0 defining the cut $\delta E_{maxmerge}^{oct}$ is varied. The x axis (b) represents variation of E_0 from 30 keV to 80 keV

5.1.3 Determination of δE_{noise}^{oct} , δE_{noise}^{rings}

$\delta E_{noise}^{oct} = \delta E_{noise}^{rings} = 30$ keV were set from the measured noise in each of these detector types. As shown earlier in chapter 3, the average measured noise in the octagon detector is ~ 8.5 keV, and that in the rings is ~ 10.6 keV. The noise cut is set at approximately 3 times this value.

To summarize, the cut parameters used in the merging procedure have been determined from detailed analysis of the signal distributions in recorded data, and comparison with simulations of the signal response. The parameter set is not unique however, and the distribution of reconstructed hits is sensitive to changes in some of the parameters. An estimate of the systematic uncertainty in the hit merging and reconstruction procedure can be gained by varying these parameters. By systematically varying all these parameters around the nominally chosen values outlined above, it was found that the number of reconstructed hit pads has the highest sensitivity (at the level of 6%) to the $\delta E_{maxmerge}^{oct}$ cut, which determines the threshold over which a pad is regarded as an independent hit rather than a shared part of a hit in the adjacent pad. This is discussed further in the estimation of systematic errors in the following chapter.

5.2 Correction for geometrical acceptance

The octagon and ring multiplicity detectors together provide coverage for measurement of charged particles out to $|\eta| < 5.4$. In the azimuthal angle ϕ however, the coverage is not complete: twelve sensors of the octagon detector have been removed to provide a clear path

for charged particles to reach the spectrometer and vertex detectors. These ‘holes’, along with the small amount of inactive areas between sensors, and at a lower level, between active pads on each sensor are taken into account by applying an acceptance correction to the measured distribution of hits.

The acceptance is calculated by a simple ray tracing algorithm: 3-vectors are drawn from a specified z_{vtx} with orientation drawn from a uniformly random distribution over $[|\eta| < 6, 0 < \phi < 2\pi]$. The intersection of a vector with a ‘box’-shaped sensor can be calculated accurately using the known geometry of the sensors. The ratio of number of vectors that intersect an active pad to the total thrown gives the acceptance as a function of (η, z_{vtx}) . Fig. 5-8a shows a contour plot of the acceptance obtained using this technique; the acceptance for $z_{vtx} = 0$ is shown in Fig. 5-8b. For the ring detectors, the acceptance is seen to be uniformly $\sim 97\%$ as per the design. For the octagon detector, the acceptance is close to 93% in the outer range of η , and falls to $\sim 50\%$ near $\eta = 0$ due to the aforementioned ‘missing’ sensors (upto four out of eight sensors in the azimuthal direction are missing).

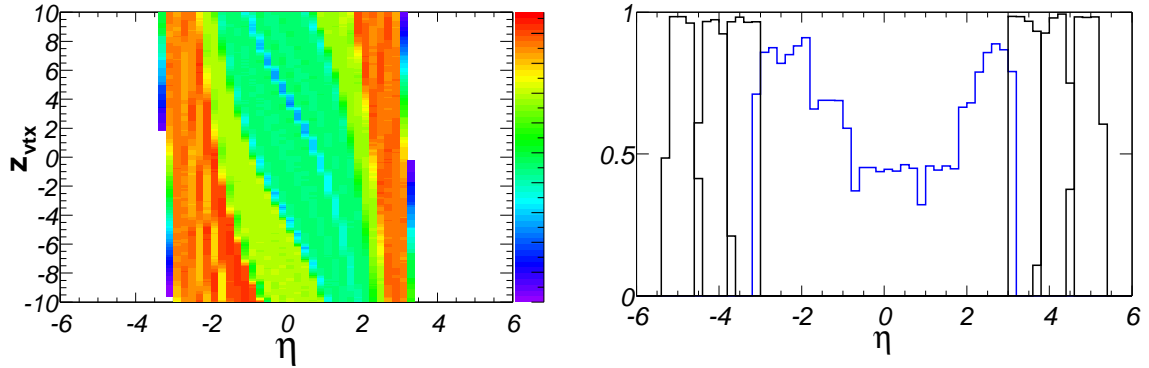


Figure 5-8: a) Geometrical acceptance of octagon detectors as function of η and z_{vtx} . b) Acceptance profile at $z_{vtx} = 0$ (octagon is shown in blue, rings in black)

An important consideration in the acceptance calculation is the fact that only *active, functional* pads are considered. A separate procedure is used to mark some pads in the multiplicity detectors as non-functional based on poor noise figures and other electronic pathologies. These ‘dead’ pads are removed from the analysis for both the acceptance calculation as well as the merging of signal hits as mentioned in the previous section. The procedure used to identify dead pads is described below.

5.2.1 Identifying and correcting for non-functional pads

The algorithm for determining whether a pad is correctly functioning over the period of data collection is based on the premise that its performance in terms of signal/noise should be commensurate with other pads in its vicinity. Since the overall fraction of defective pads in each detector during the initial installation phase was $< 2\%$, the procedure is quite reliable in locating pads whose performance has become flaky over the run period.

Since the event-by-event hit distribution has a characteristic shape along η which varies as a function of the vertex position z_{vtx} , the appropriate degree-of-freedom for comparing pad-wise performance is the azimuthal angle ϕ for a narrow range of z_{vtx} . Pads located at the same η position (and different ϕ positions) register on average, similar number of hits if they are functioning correctly. To obtain a reference for the performance of individual pads, the following hit profiles are created (a hit is simply defined as signal larger than a noise threshold, δE_{noise}^{oct} or δE_{noise}^{rings}):

1. For the octagon detector: A reference profile of hits as a function of z -position of pads, *i.e.*, integrated over all pixels in ϕ
2. For the ring detectors: A reference profile of hits as function of radial distance (r) from the beam line

Note that the z -position of pads for the octagon, and radial distance r of pads in case of rings, corresponds to η . z and r are chosen over η due to the projective geometry of the detectors, to ensure equal population of pads in each bin of the reference profile.

Once the profiles have been obtained, a search is performed over all the pads in the octagon and ring detectors: if the number of hits measured in any pad is greater than $N\sigma$ away from the profiled mean at its z (for octagon) or r (for rings) position, the pad is marked as non-functional. The procedure locates pads that have stopped producing signals during the run period as well as overly noisy or ‘hot’ channels

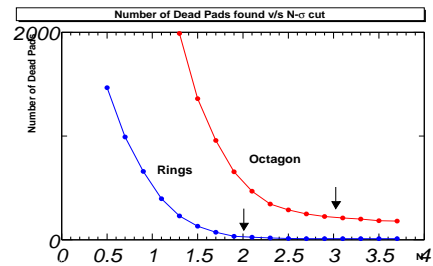


Figure 5-9: Number of dead pads as a function of $N\sigma$ cut

that produce too many hits. The parameter N was determined by choosing N large initially, and then decreasing it in steps to see how many ‘dead’ pads are located (Fig. 5-9). As N becomes small enough to start cutting into the statistical dispersion and intrinsic noise of

the detectors, the number of pads marked dead starts rising sharply. Accordingly, values of $N = 3$ (octagon) and $N = 2$ (rings) were chosen.

A further consideration in determining the health of silicon pads is anomalous gain as measured by the gain calibration procedure. Pads exhibiting less than 80% of the chip average gain over any part of the running period are also marked as non-functional and removed from the analysis. The combined dead pad map used while calculating the acceptance and also in the hit reconstruction procedure is exhibited in Fig. 5-10. It contains 338 out of a total of 11776 pads in the octagon detector marked dead (2.8%) and 95 out of 3072 pads in the ring detectors (3.1%). A substantial fraction of these pads is the same as those found in pre-installation bench tests of the detectors. The remainder are pads that developed pathologies during the running period.

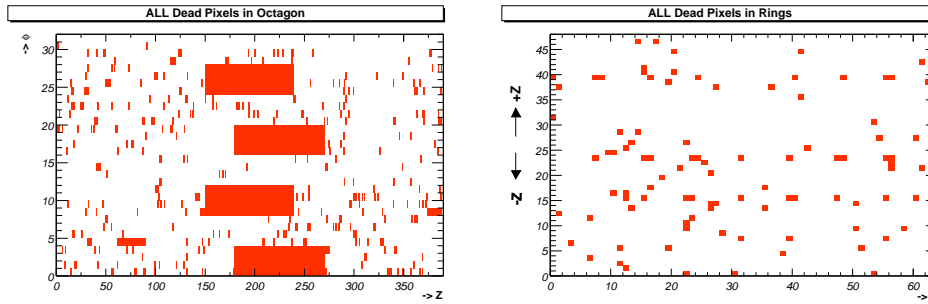


Figure 5-10: Map of dead pads in octagon and ring detectors

5.3 Correction for high occupancy in multiplicity detector

As shown in Fig. 5-1, the density of hit pads in the mid-rapidity region of the octagon is quite high. This density increases as a function of centrality of collisions (since the number of produced charged particles increases monotonically with centrality); in the most central events up to 80% of pads in the mid-rapidity region show large signals. As a result, the probability that a single pad contains energy deposition from more than one charged particle track becomes large enough that this high ‘occupancy’ needs to be corrected for in the analysis.

Let us define the mean number of particles traversing a pad $\mu \equiv \langle N_{ch}/N_{pads} \rangle$ as the true occupancy of the detector. The occupancy observed in the data is $\mu' \equiv N_{hitpads}/N_{pads}$. If we assume that the distribution of particle tracks is uniform in azimuth ϕ at a given η position for a given centrality class of events, then the number of tracks per pad is distributed

according to Poisson statistics: the probability of finding n tracks per pad is:

$$P(n) = \frac{\mu^n e^{-\mu}}{n!} \quad (5.2)$$

In particular the measured occupancy μ' is related:

$$\mu' = P(n > 0) = 1 - P(0) = 1 - e^{-\mu} \approx \mu \left(1 - \frac{\mu}{2}\right) + O(\mu^3) \quad (\mu \ll 1) \quad (5.3)$$

Thus, the measured occupancy is lower than the true occupancy. We would underestimate the true multiplicity quite drastically if we considered just the measured number of hit pads to be the actual charged particle multiplicity.

Two separate methods have been devised to correct for this effect and account for the high occupancy. They are both described in the following sections. It is important to reiterate that while calculating the occupancy corrections, events are separated into centrality classes, and the corrections calculated bin-wise in η , integrating over the azimuth ϕ , to satisfy the assumption stated above regarding uniform distribution of charged particle tracks over a set of pads.

5.3.1 Correction based on Poisson statistics

Given the hypothesis that the number of particle tracks per pad is distributed according to Poisson statistics, the probability of at least one particle hitting a given pad is

$$\sum_{n>0} P(n) = 1 - P(0) = 1 - e^{-\mu}$$

where the true occupancy μ is obtained from the measured occupancy by the inverse of Eqn. (5.3) *i.e.*, :

$$\mu = \ln(1 - \mu')^{-1} \quad \mu' \equiv \frac{N_{hitpads}}{N_{pads}} \quad (5.4)$$

The *mean* number of particles traversing a pad, given that the pad has been identified as a hit pad provides the sought for occupancy correction:

$$O = \frac{\sum_{n>0} n \times P(n)}{\sum_{n>0} P(n)} \quad (5.5)$$

$$= \frac{e^{-\mu}}{1 - e^{-\mu}} \left(\mu + \mu^2 + \frac{\mu^3}{2} + \frac{\mu^4}{6} + \dots \right) \quad (5.6)$$

$$= \frac{\mu}{1 - e^{-\mu}} \quad (5.7)$$

In practice, the occupancy correction O is determined as a function of η and centrality (b) by accumulating the number of hit pads per η -bin for all events belonging to the same centrality class and finding the ensemble average of true occupancy per pad using Eqn. (5.4). The occupancy correction $O(\eta, b)$ is then calculated from Eqn. (5.7) and applied as a multiplicative factor to the event-by-event hit distribution in the next pass over the data. Fig. 5-11a shows the dependence of $O(\eta, b)$ on the measured occupancy μ' . Fig. 5-11b shows the calculated occupancy corrections as a function of η for three centrality classes of events at $\sqrt{s_{NN}} = 200$ GeV. The correction reaches a maximum of 1.6 tracks per *hit* pad near mid-rapidity for the most central collisions corresponding to a measured occupancy of $\mu' \sim 80\%$ or a true occupancy of ~ 1.2 tracks per pad.

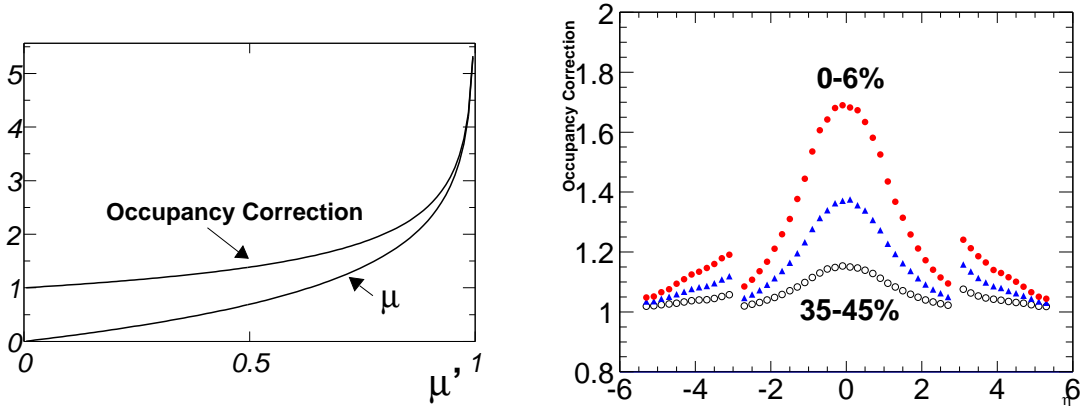


Figure 5-11: a) True occupancy μ and occupancy correction O as a function of measured occupancy μ' . b) Measured occupancy correction $O(\eta, b)$ at $\sqrt{s_{NN}} = 200$ GeV for centrality bins 9, 13 and 17.

5.3.2 Correction based on shape of energy loss distribution

A second method of correcting for high occupancy in the detector has been devised based on the observation that two or more particles traversing a single pad will deposit a proportionately larger signal in the pad than a single particle. Fig. 5-12 displays the distribution of energy signals measured in a set of pads near $\eta = 0$, for central collisions at $\sqrt{s_{NN}} = 200$ GeV. The large first peak corresponds to energy deposition by a single MIP traversing the pad; secondary and tertiary peaks can be seen from events where two or three MIP's deposited energy in the same pad. For regions of the detector where the occupancy is very low and

for peripheral events, the contributions from the second and third peaks are suppressed.

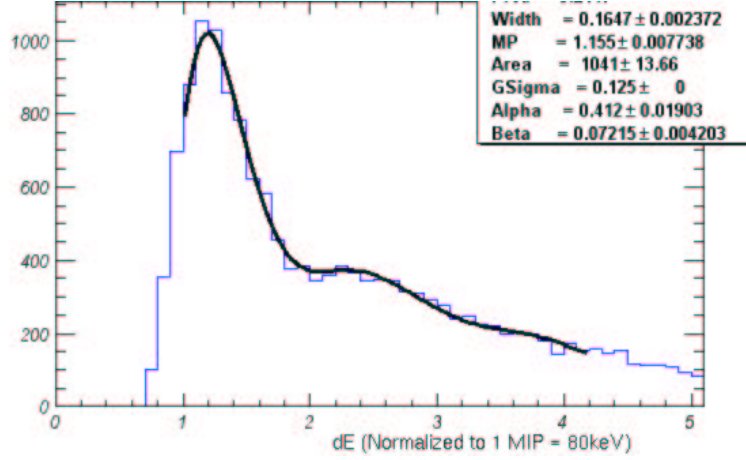


Figure 5-12: Distribution of energy signals measured in pads near $\eta = 0$ for central events

Given that an energy signal E is measured in a specific pad, the probability that a single particle deposited this energy is distributed according to the Shulek corrected Landau-Vavilov distribution ($f_S(E, \xi)$ of Eqn. (3.5)). In addition, we have to consider the possibilities of two particles depositing energies ($E - dE'$) and dE' , distributed as

$$f_S(E - dE', \xi') \times f_S(dE', \xi')$$

three particles depositing energies ($E - dE' - dE''$), dE' and dE'' distributed as

$$f_S(E - dE' - dE'', \xi'') \times f_S(dE', \xi') \times f_S(dE'', \xi'')$$

and so on. Each of these possibilities is subject to Gaussian electronic noise induced into the signal. The composite distribution of Fig. 5-12 can be fitted with a sum of functions, each of which is a convolution of multiple Landau-Vavilov distributions with an extra Gaussian component. The exact functional form used is:

$$f(E) = A \cdot [f_S(E) + \alpha \cdot f_S(E) \otimes f_S(E) + \beta \cdot f_S(E) \otimes f_S(E) \otimes f_S(E)] \otimes G(\sigma) \quad (5.8)$$

where \otimes represents a convolution, $G(\sigma)$ is a Gaussian distribution with width σ . The Landau-Vavilov-Shulek functions are characterised by two free parameters: a ‘most-probable

value' and a 'width'¹. A is an overall normalisation constant and α , β represent the contributions of the second and third MIP peaks to the overall distribution. If A_i denotes the contribution of the i 'th MIP peak to the total distribution, then the average occupancy correction, *i.e.*, the average number of particles per hit pad is given as:

$$O = \frac{\sum_i i \cdot A_i}{\sum_i A_i} \quad (5.9)$$

$$= \frac{1 + 2\alpha + 3\beta + \dots}{1 + \alpha + \beta + \dots} \quad (5.10)$$

In practice, the series is only modelled up to the third peak since further peaks are barely evident in the measured distribution. Also, the computational complexity of fitting triply convolved functions to the distribution is significantly eased by the realisation that a convolution of multiple identical Landau-Vavilov functions is also a Landau-Vavilov function whose width and most-probable value is analytically determined from the single function (cf. Appendix B). The six free parameters of the fit are therefore σ (constrained from the measured noise), width and most probable value of the single Landau peak, the normalisation A and most importantly, α and β . The distributions are obtained from signals in groups of pads at each η bin for each centrality class; they are then fitted with Eqn. (5.8) and the occupancy correction $O(\eta, b)$ calculated from the fit results α, β according to Eqn. (5.10). Fig. 5-13 displays the occupancy correction factors as a function of η for three centrality classes of events at $\sqrt{s_{NN}} = 200$ GeV.

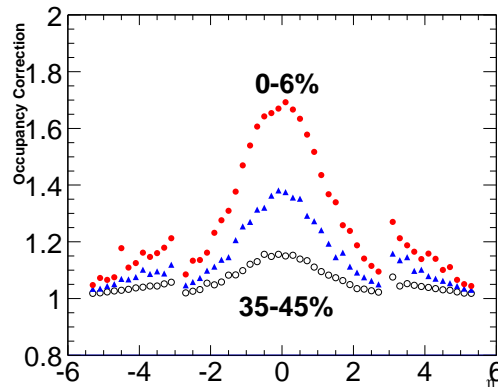


Figure 5-13: Occupancy corrections based on fitting the energy loss distribution

¹The form of this function is characterised by any two parameters; in the earlier discussion in chapter 3, the mean energy loss ξ and the Shulek correction factor δ_2 were used. The most-probable value and width are used here instead for computational ease

This method of deriving occupancy corrections from fitting the energy loss distributions to find contributions of second and third MIP peaks is inherently flawed by truncation at the third peak. It is also subject to the quality of fits and assumes that all particle hits arise from MIP's. Nevertheless, it provides an invaluable cross-check to the corrections derived from assumption of Poisson statistics in the previous section. The close agreement of corrections obtained from the two methods (Fig. 5-11 and Fig. 5-13) provides ample proof that the assumption of Poisson statistics is indeed justified. The fitted contribution of second and third peaks represented by α , β is simply related to the mean occupancy of tracks per pad μ :

$$\begin{aligned} A = P(n = 1) &= \mu \cdot e^{-\mu} \\ A \cdot \alpha = P(n = 2) &= \mu^2 \cdot \frac{e^{-\mu}}{2} \\ A \cdot \beta = P(n = 3) &= \mu^3 \cdot \frac{e^{-\mu}}{6} \end{aligned}$$

and therefore $\mu = 2\alpha = \sqrt{6\beta}$. This relationship is indeed borne out by the fit results over the full range of η and centrality of events.

5.4 Correction for hits from secondary particles

After correcting the distribution of hits for the geometrical acceptance of the detector, and high occupancy in certain regions, we are still faced with the question of what fraction of these hits are produced by primary particles produced in the Au+Au collision. A number of effects, such as the production of secondary particles away from the primary vertex, absorption of particles in the beam pipe and backgrounds produced in various intervening parts of the apparatus are difficult to estimate from the data alone.

To examine the effect of such processes on the multiplicity measurement, we resort to the GEANT based detector simulation discussed earlier in chapter 3. An event generator (HIJING) is used to generate a primary charged particle distribution. The passage of these particles through the detector volume is simulated using GEANT with secondary effects like weak decays of particles and production of knock-on δ -rays turned on, and the noise response of the detector electronics is convoluted in to the deposited energy in active pads of the silicon sensors.

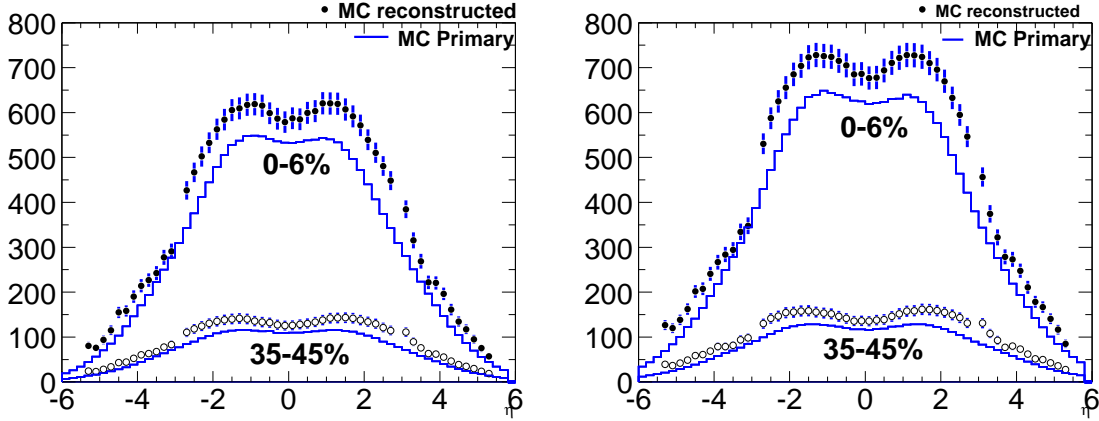


Figure 5-14: Comparison of reconstructed $dN_{ch}/d\eta$ in MC simulation (markers) to the ‘true’ primary particle input (line) in $\sqrt{s_{NN}} = 130$ GeV (left) and $\sqrt{s_{NN}} = 200$ GeV (right) collisions. Central (0-6%) and Peripheral (35-45%) collisions are shown.

The output events of the Monte Carlo simulation are then analyzed in precisely the same fashion as the real data: hit merging is performed on the pad signals using identical threshold cuts, the occupancy corrections are derived from the reconstructed hits in the simulation itself. After applying the geometrical acceptance factors to the occupancy corrected hit distribution, a reconstructed multiplicity distribution $dN_{ch}/d\eta$ is obtained from the simulation.

This can be compared to the primary particle input of the simulation as shown in Fig. 5-14. The number of reconstructed charged particles is systematically slightly higher than the input primary particles indicating that the remainder are secondary particles produced away from the primary vertex. The ratio of the two distributions as a function of η and centrality provides the final ‘background’ correction $B(\eta, b)$ to be applied to the data in reconstructing $dN_{ch}/d\eta$

$$B(\eta, b) = \frac{dN_{ch}/d\eta|_{MCtrue}}{dN_{ch}/d\eta|_{MCreconstructed}} \quad (5.11)$$

It is important to ensure that this background correction is not biased in any way by the choice of primary particle input, *i.e.*, the event generator used. A first hint that this is not the case is offered by Fig. 5-15 which shows the background correction as a function of η for three centrality classes of events at $\sqrt{s_{NN}} = 200$ GeV. If the excess of reconstructed charged particles over the primary input is really from secondary particle production, then given the

fact that the number of produced secondaries is proportional to the number of primaries, the *ratio* of the two should remain constant as the number of primary particles increases. This is indeed borne out by Fig. 5-15: at a given η value, the ratio of the reconstructed simulation output to the primary particle number remains constant over all the centrality classes (the mean number of primary particles at $\eta = 0$ for the three centrality bins shown are 120, 350 and 550 respectively).

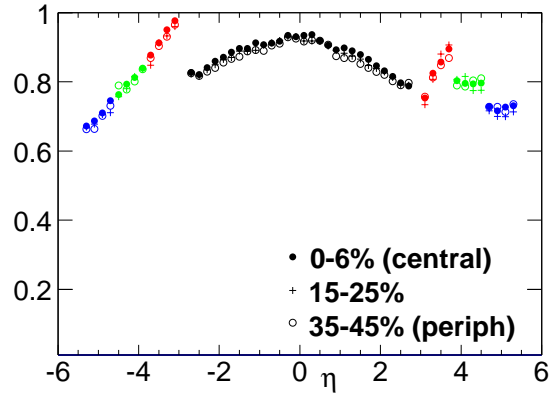


Figure 5-15: Background corrections derived from HIJING simulations for three centrality classes

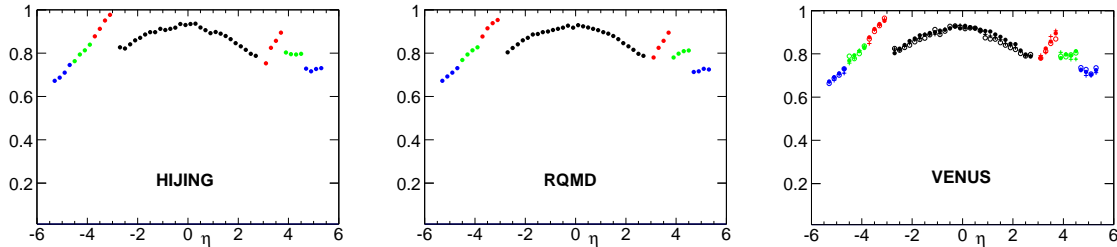


Figure 5-16: Background corrections derived from three different simulations using (a) HIJING, (b) RQMD, and (c) VENUS event generators. Note that equivalent centrality classes defined for the three event generators are based on dividing the cross section as measured by the total number of hits into equal slices (cf. Appendix C for details)

A further cross-check on the robustness of the background correction factors has been performed by using different event generators (RQMD and VENUS) to provide an input primary particle distribution to the GEANT simulation. Each of these generators has different particle composition and momentum distributions for the primary particles. In particular the number of primary particles produced at $\eta = 0$ by HIJING, RQMD and VENUS for the most central events is 550, 450 and 1200 respectively. The reconstructed

multiplicity distributions from each of these simulations is divided into its primary particle input to obtain the background correction factors in like manner (cf. Appendix C for details). The factors derived from these different simulations show remarkable agreement as seen in Fig. 5-16.

5.5 Summary of applied corrections

To summarize, the equation used to reconstruct $dN_{ch}/d\eta$ from the measured merged hit distributions N_{hits} is:

$$\left\langle \frac{dN_{ch}}{d\eta}(\eta, b) \right\rangle = \left\langle \frac{N_{hits}(\eta, b) \times O(\eta, b)}{\Delta\eta \times A(\eta, z_{vtx})} \times B(\eta, b) \right\rangle \quad (5.12)$$

where $\langle \dots \rangle$ denotes an ensemble average over all events belonging to the same centrality class (b). In a preliminary pass over the data and simulation, hit merging is done to obtain the distribution of average number of reconstructed hits $N_{hits}(\eta, b)$ as a function of η and centrality b , binned in units of $\Delta\eta = 0.2$. The average occupancy correction $O(\eta, b)$ is then calculated based on the ratio of hit pads to total pads per $\Delta\eta$ bin as discussed in section 5.3. In a second pass over the MC simulation output, the acceptance $A(\eta, z_{vtx})$ and occupancy corrections are applied to the event-by-event N_{hit} distribution, and the reconstructed output compared to the input primary particle distribution to obtain the correction for secondaries $B(\eta, b)$ as discussed in section 5.4. Finally, in a last pass through the data set, the calculated occupancy, acceptance and background correction factors are applied event-by-event to obtain an event-by-event reconstructed $dN_{ch}/d\eta$ distribution which is then averaged over events belonging to the same centrality bin to arrive at the final $\langle dN_{ch}/d\eta \rangle$ distribution as a function of η and centrality.

The results of this analysis are presented in the following chapter, and various sources of possible systematic error in the procedure are discussed.

Chapter 6

Results and Conclusions

Table 6.1 provides a detailed listing of data and simulation runs which were analysed to determine the charged particle distributions presented in this chapter. The $\sqrt{s_{NN}} = 130$ GeV data was from the PR00 running period, and the $\sqrt{s_{NN}} = 200$ GeV data was from the PR01 running period (cf. Table 2.1).

The geometry of the multiplicity detector remained identical over these two run periods, though the spectrometer was upgraded in the intervening gap. The triggering scheme as described in chapter 4 was also kept unchanged. The specific cuts used in the analysis, along with the versions of signal processing employed, are listed in Table 6.1. As a general principle, the number of simulation events used to extract background corrections was kept at roughly double the number of data events available for analysis, in order to reduce statistical spread in the corrections.

$\sqrt{s_{NN}}$	List of DATA Runs (Number of Events)	List of MC Runs (Number of Events)	Trigger Cuts
130 GeV	5365, 5366, 5367, 5372, 5373, 5374, 5379, 5380, 5381, 5383, 5384 ONLV_1.2.9 (14,214)	5191, 5192, 5193, 5194 SMV0_4 (33,786)	TrgCuts_PR00_130Pre_BZ
200 GeV	7267, 7269, 7284, 7293, 7294,7295, 7301 ONLV_2.1.6 (6,849)	5141, 5142, 5143 SMV1_4 (20,303)	TrgCuts_PR01_200_BZ

Table 6.1: Summary of Data and Simulation Runs used for analysis.

In the following sections, we present results on the charged particle multiplicity measurements, starting with the pseudo-rapidity distributions at $\sqrt{s_{NN}} = 130$ GeV and $\sqrt{s_{NN}} = 200$ GeV for different classes of centrality. The trends observed in the fragmentation region and the central rapidity region are discussed, and comparisons are made with earlier $p + p$, $p + A$ and $A + A$ data. The possible systematic effects in these measurements are described in detail and the method of evaluating systematic errors is presented. Finally a comparison is made with predictions from various models, and conclusions regarding the possible particle production mechanisms in heavy ion collisions are summarised.

6.1 Results

6.1.1 Pseudo-rapidity distributions of charged particles

The data from runs listed in Table 6.1 were analyzed using the procedures explained in chapters 3,4,5. Events with a valid RMSSelVertex in the range $-10\text{cm} < z_{vtx} < +10\text{cm}$ were sorted into centrality bins numbering 0 to 17, with bin 17 corresponding to the most central collisions (top 0-3% of the cross section) and bin 0 corresponding to the most peripheral (95-100% of the cross section). For each centrality class, the occupancy corrections assuming Poisson statistics were determined from a first pass over the data. The detector signals in simulated events were ‘smeared’ with noise and de-calibrated to make them look similar to real data, and analysed in a similar manner. A comparison was made with the true primary particle input to obtain η and centrality dependent background corrections. In a second pass over the data, the occupancy, background and acceptance corrections were applied to the reconstructed hit distributions, as per Eqn. (5.12), to obtain the average $dN_{ch}/d\eta$ as a function of η for each centrality bin.

The results are shown all together in Fig. 6-1, and in Fig. 6-2 and Fig. 6-3 for $\sqrt{s_{NN}} = 130$ GeV and $\sqrt{s_{NN}} = 200$ GeV respectively. For clarity, the results from two centrality bins are combined and displayed in all the figures in this chapter, thus the centrality bins indicated are 0—6%(most central), 6—15%, 15—25%, 25—35%, 35—45% and 45—55%(most peripheral). The statistical error is computed from the merged hit distribution $N_{hits}(\eta, b)$, and then propagated through the multiplicative correction factors in Eqn. (5.12). The statistical errors thus obtained are very small, and although shown in Fig. 6-2 and Fig. 6-3, are smaller than the size of markers used for each data point. Also

shown are grey bands indicating the best estimate of systematic error on the measurements; the estimation procedure is discussed in the following section.

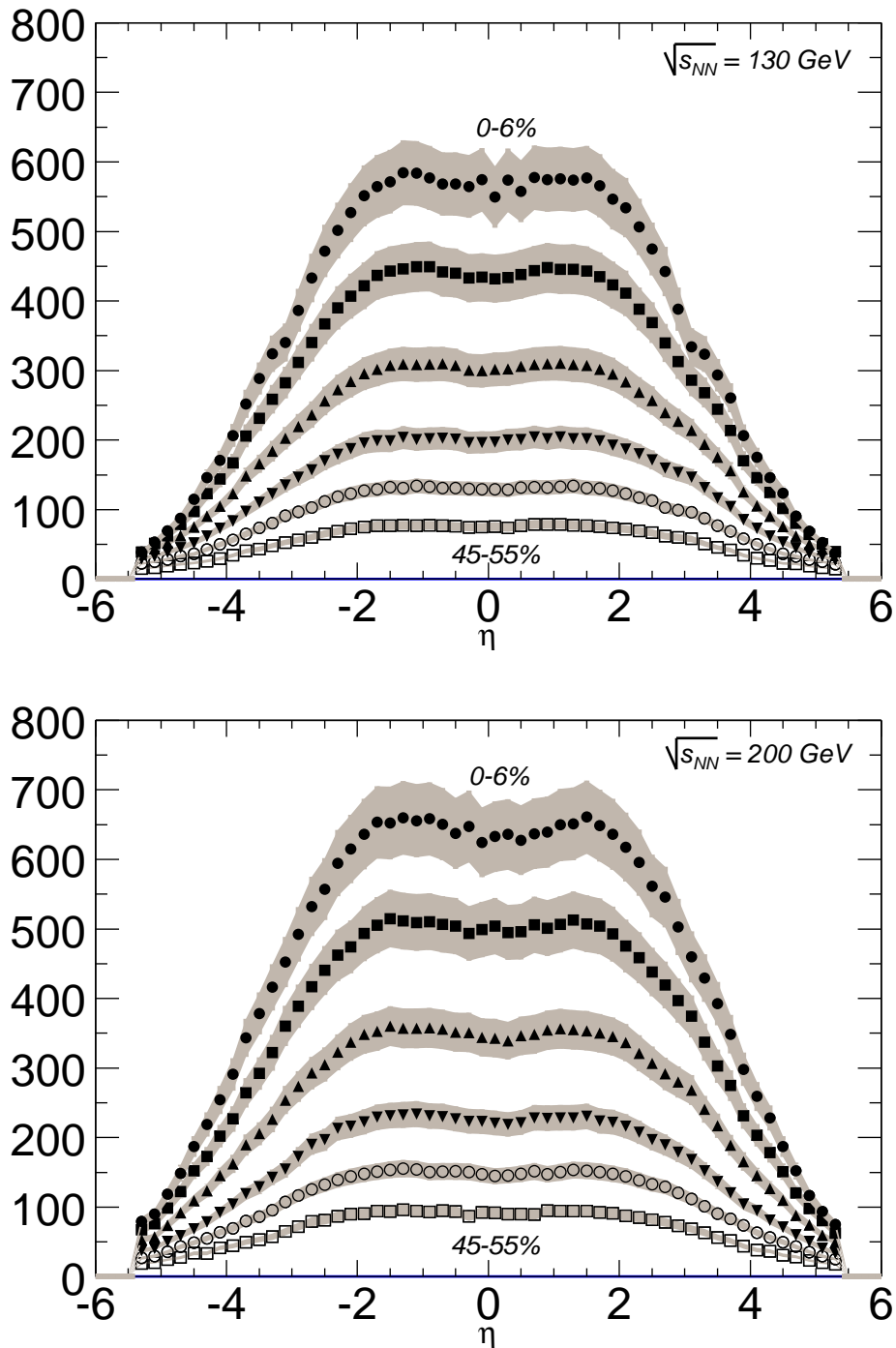


Figure 6-1: $dN_{ch}/d\eta$ as a function of η for $\sqrt{s_{NN}} = 130 \text{ GeV}$ (top) and $\sqrt{s_{NN}} = 200 \text{ GeV}$ (bottom). All centrality bins shown together.

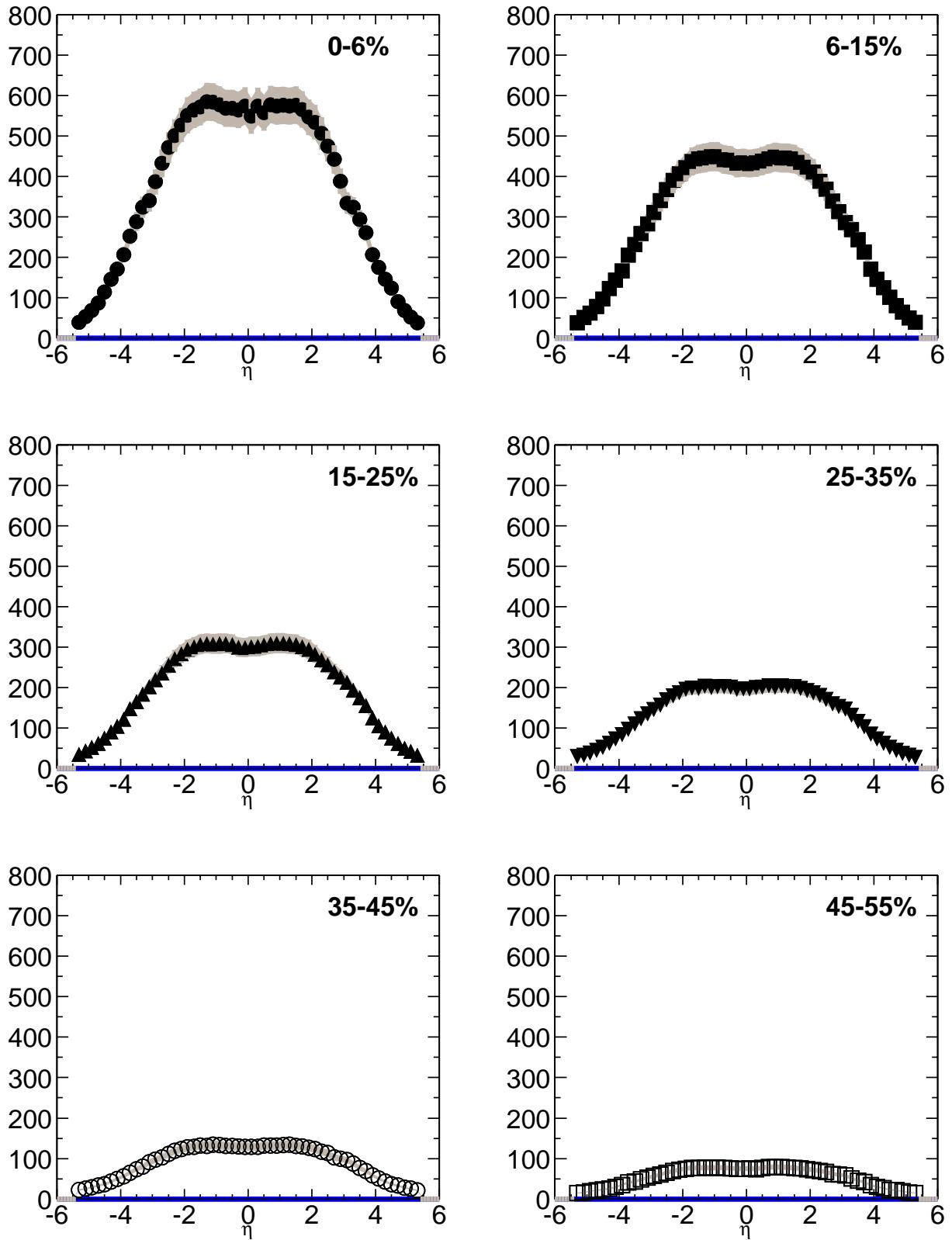


Figure 6-2: $dN_{ch}/d\eta$ as a function of η for $\sqrt{s_{NN}} = 130$ GeV. Data for different centrality bins, ranging from the most central 0-6% to peripheral 45-55% is shown separately.

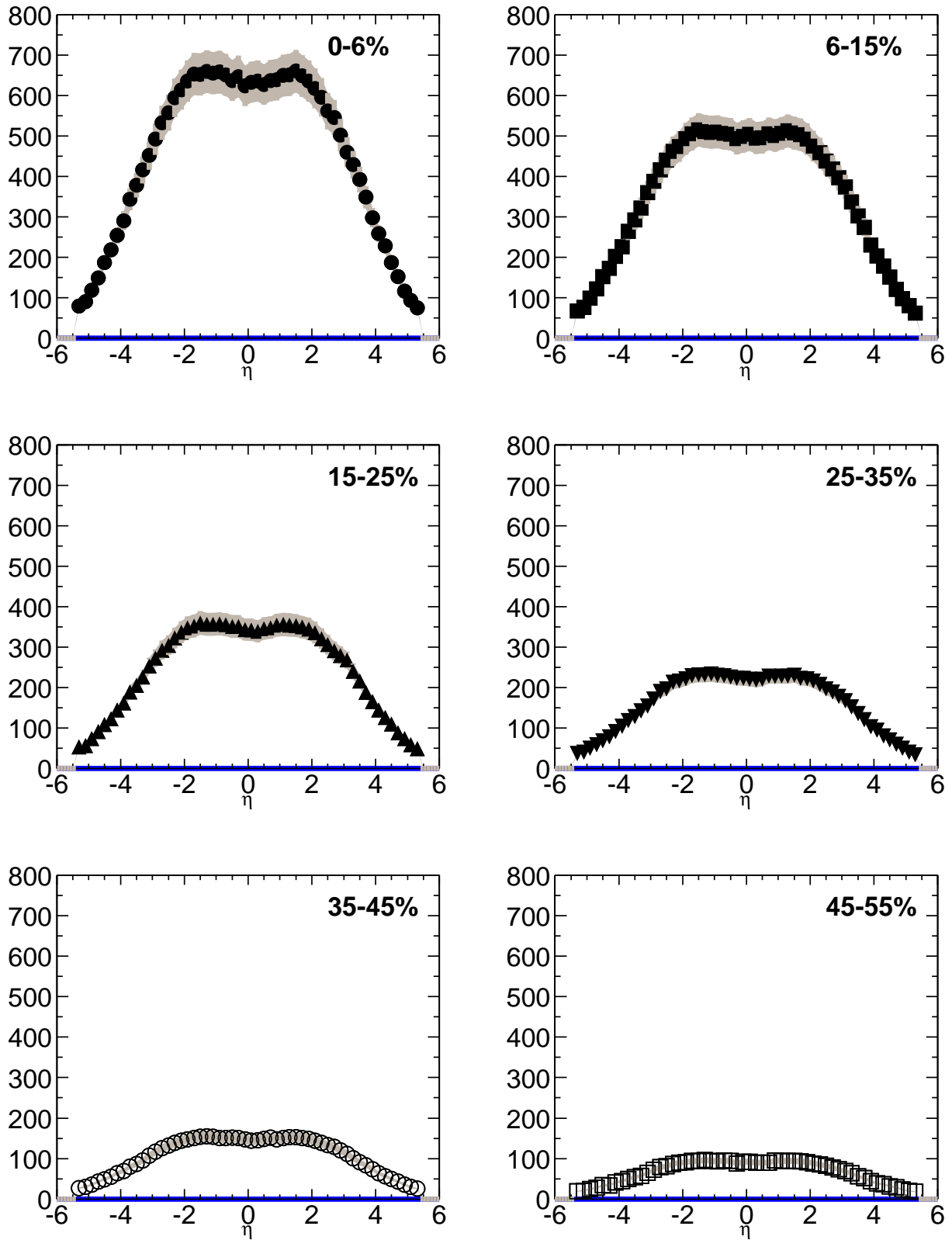


Figure 6-3: $dN_{ch}/d\eta$ as a function of η for $\sqrt{s_{NN}} = 200$ GeV. Data for different centrality bins, ranging from the most central 0-6% to peripheral 45-55% is shown separately.

We focus our discussion on the results of the previous two pages by considering two kinematically separate regions of pseudo-rapidity, where striking features of the measured $dN_{ch}/d\eta$ emerge.

6.1.2 Fragmentation region

As noted previously in chapter 1, with increasing $\sqrt{s_{NN}}$, there is a trivial kinematic broadening of the $dN_{ch}/d\eta$ distribution due to the increasing rapidity $y = \pm \ln\sqrt{s}/m$ of the colliding nuclei. In order to reveal more interesting dynamic features, it is useful to transform to the rest frame of one of the colliding nuclei, and look at how the number of produced particles varies with beam energy and centrality in this fragmentation regime. For this purpose, a boost invariant quantity like the rapidity y is necessary. To investigate the fragmentation regime, we are interested primarily in the behaviour at large y , where the difference between y and η is nearly negligible[46]. We therefore use a pseudo transformation to a variable $\eta' = (\eta - y_{beam})$, and normalize the results of $dN_{ch}/d\eta$ at two energies in such a way that $\eta' = 0$ corresponds to the rest frame of either nucleus.

Fig. 6-4a shows the shifted distributions $dN_{ch}/d\eta'/\langle N_{part}/2 \rangle$ for central Au+Au collisions at the two energies. The distributions have been scaled by $\langle N_{part}/2 \rangle$ to take out the first order effect of number of participating nucleons in determining particle production. Further, they are folded around mid-rapidity, *i.e.*, positive and negative η bins are averaged. The distributions at two energies are observed to fall on the same limiting curve over a broad range $-2 < \eta' < 0$. This indicates that once the dependence on $\langle N_{part}/2 \rangle$ is factored out, the number of produced particles in the fragmentation region is *independent* of beam energy.

Similar behaviour of $dN_{ch}/d\eta'$ distributions has been observed earlier in $p + \bar{p}$ collisions[116] as indicated in Fig. 6-4b and was predicted as long ago as 1969 in a simple model for $p + \bar{p}$ collisions developed by Benecke, Chou and Yang[57]. They proposed an ansatz of “limiting fragmentation”, which states that at high enough energy of hadron-hadron collisions, both $d^2N/dydp_T$ and the mix of particle species reach a limiting value independent of beam energy for rapidity values corresponding to either target or project rapidity.

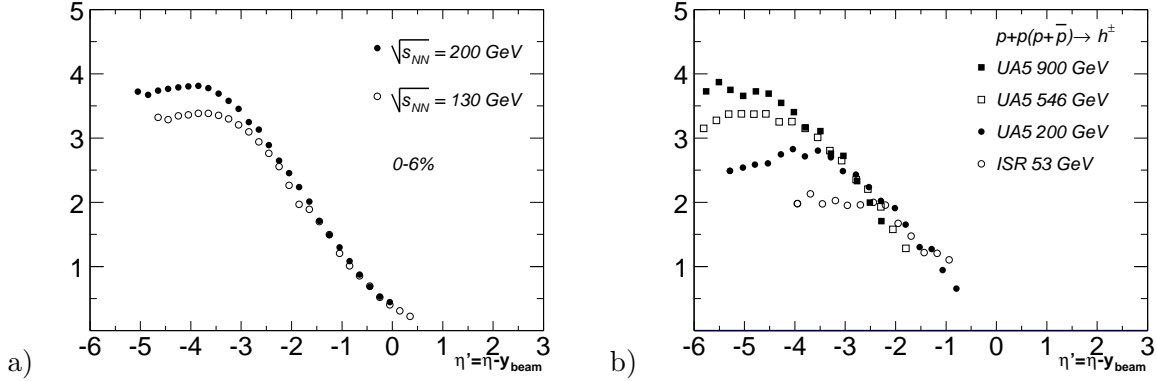


Figure 6-4: $dN_{ch}/d\eta'$ in (a) central Au+Au collisions at two energies, (b) in $p + \bar{p}$ collisions[116]

The physical picture of a $p + \bar{p}$ collision in the rest frame of one of the particles is illustrated in Fig. 6-5: at high energies, the target proton serves as an absorbing medium through which the incoming particle propagates as a wave. Due to Lorentz contraction, the incoming particle appears as a thin disk whose passage through the target is nearly instantaneous¹. The constancy of the total $p + \bar{p}$ cross section at high energies implies that the momentum and quantum-number exchange processes between “stuff” in the projectile and “stuff” in the target don’t change appreciably as the projectile is further Lorentz contracted at higher $\sqrt{s_{NN}}$.

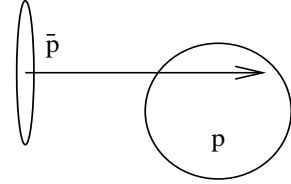


Figure 6-5: A $p + \bar{p}$ collision

In the framework of QCD, a modern picture of the collision takes into account the quark-gluon composition of the $p + \bar{p}$ system. In the rest frame of the target proton, the dominant wave-functions are those of valence quarks which are very dilute since they are at large x_F , where x_F is the Feynman scaling variable measuring the fraction of longitudinal momentum carried by a constituent parton. The oncoming projectile’s wavefunction is dominated by small x_F contributions (since only the *slowest* components of the projectile have time to interact), i.e. the oncoming projectile looks like a dense gluonic cloud. As the energy of the collision $\sqrt{s_{NN}}$ increases, larger x_F contributions are added to the projectiles wavefunction (a phenomenon called Feynman scaling [117]), which, as we have just seen, are unimportant for interactions in the target’s rest frame.

¹The target proton’s diameter is $\sim 0.7\text{fm}$, and the passage time at $\sqrt{s_{NN}} = 200\text{ GeV}$ is $\sim 0.02\text{ fm}/c$, much smaller than the formation time of any particles

Our measurement of Fig. 6-4a is the first verification of such limiting behaviour in $A + A$ collisions, and seems to indicate that puzzlingly, a simple picture of projectile and energy independent particle production in the fragmentation region applies to some extent even in the complex environment of a fragmenting nucleus.

Two specific features of the limiting behavior seen in our data are noteworthy. Firstly, the limiting curve in Fig. 6-4a extends over 2 units of pseudo-rapidity. Particles produced at $\eta' \sim -2$ are travelling at only about half the velocity of the nucleus, and with average formation times of the order of 1 fm/c, must be produced far outside the nucleus. The fact that the production of such particles far from the original beam rapidity lies on a limiting curve seems to hint that this universal curve is an important feature of the overall interaction and not just a nuclear breakup effect.

The second aspect of our pseudo-rapidity data is exhibited in Fig. 6-6a, where we plot the measured $dN_{ch}/d\eta'/\langle N_{part}/2 \rangle$ for peripheral collisions (35-45% of the cross section). Similar limiting behaviour is again seen over a broad range in η' . At each energy $\sqrt{s_{NN}}$, if we compare the distributions in central to peripheral collisions, as shown in Fig. 6-6b,c, we observe that the shape of the limiting curve is *different* for central versus peripheral collisions.

This is further illustrated in Fig. 6-6d, which shows a ratio of the peripheral to central $dN_{ch}/d\eta'$ for each $\sqrt{s_{NN}}$. In taking the ratio, some of the systematic errors involved in each of the measurements partially cancel. The uncertainty on $\langle N_{part} \rangle$ in particular, is eliminated completely. Fig. 6-6d indicates that the scaled pseudo-rapidity density of charged particles in the $-1.5 < \eta' < 0$ region actually *grows* for peripheral collisions, to an extent independent of the energy of the collision. As the centrality of the collision increases, there is a pronounced narrowing of the pseudo-rapidity distribution: the yield in the fragmentation region decreases, accompanied by an increase in the mid-rapidity yields and a cross-over centered near $\eta' \sim -1.5$. Such behaviour has previously been observed in $p + A$ collisions[118] and Pb+Pb collisions at lower $\sqrt{s_{NN}}$ [119].

It has been speculated [59, 120] that such a narrowing of the overall distribution may be caused by:

- Dynamical effects like baryon stopping, or large baryon energy loss in a nuclear medium causing baryon number to be transported from the beam rapidities to the mid-rapidity region. While this scenario may have some applicability in lower en-

ergy A+A collisions, at $\sqrt{s_{NN}} = 200$ GeV, the net baryon number at mid-rapidity approaches zero² as measured by the ratio of anti-protons to protons near $\eta = 0$ [121].

- Kinematic effects such as a shift in η' , at a fixed y' , of the produced particles due to a change in the particle mixture (*i.e.*, the π^\pm/p ratio) as a function of centrality in A + A collisions. Such a shift would be a sharp contrast to earlier measurements in $p + A$ collisions[122]. A measurement of the π^\pm/p ratio at large rapidity values at RHIC would provide support for this hypothesis.

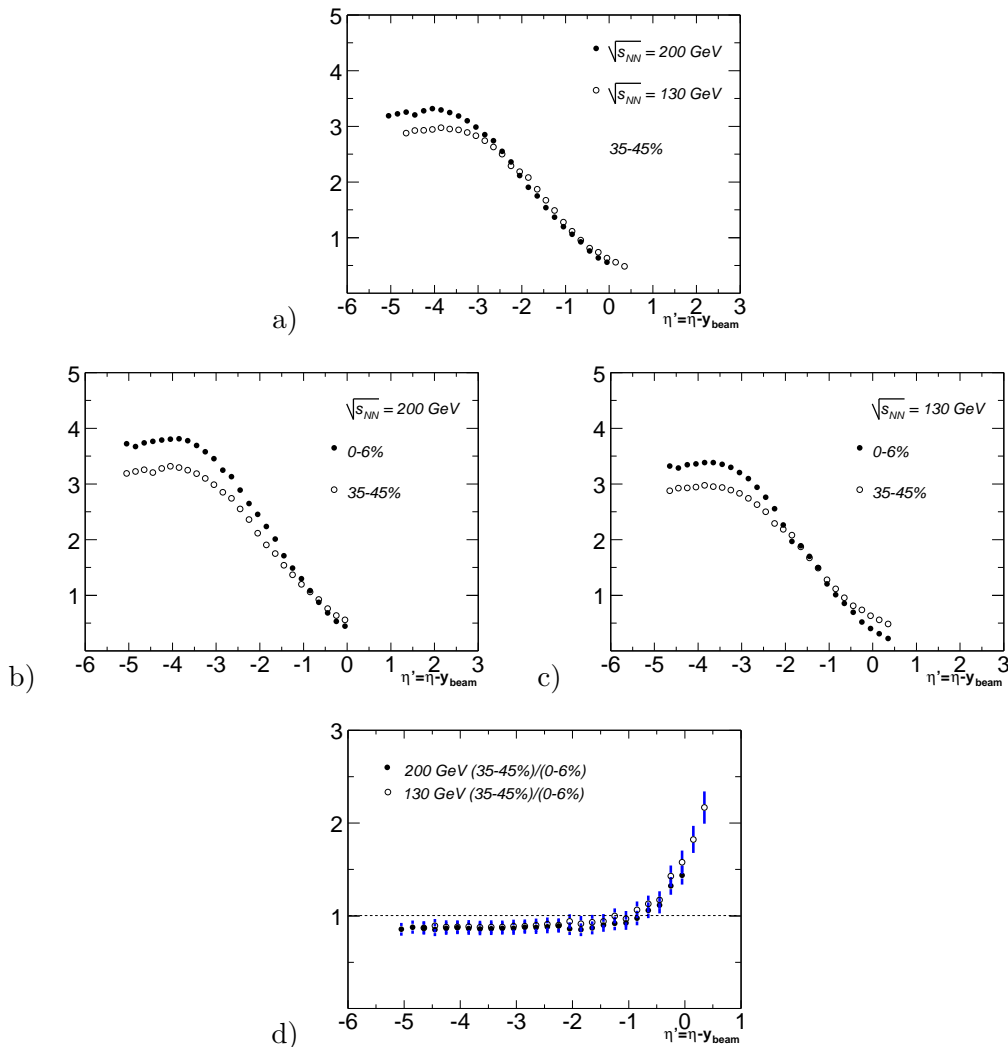


Figure 6-6: Comparison of $dN_{ch}/d\eta'$ scaled by $\langle N_{part} \rangle / 2$ between central and peripheral collisions.

See text for discussion

²Referring back to the discussion of baryon rapidity loss in chapter 1, since beam rapidity at $\sqrt{s_{NN}} = 200$ GeV is $y = 5.4$, the average rapidity loss of 2 units for baryons is insufficient to cause significant baryon number transport down to $y = 0$.

6.1.3 Central rapidity region

$dN_{ch}/d\eta$ in the central rapidity region is an important measure of the amount of entropy produced in a Au+Au collision. In the center of mass system, $y = 0$ corresponds to a region of space where, before the collision occurs, only pure vacuum exists. During the collision, the two highly Lorentz contracted nuclei overlap very briefly in position space, depositing large energy in the vacuum and the heated vacuum then cools by producing particles.

Fig. 6-7 shows our measurement of the scaled charged particle yield $dN_{ch}/d\eta/\langle N_{part}/2 \rangle$ at $\eta = 0$, as a function of collision energy for central collisions (a), and as a function of centrality for the two different collision energies (b). Also shown in these figures are measurements on $dN_{ch}/d\eta$ in $A + A$ collisions at lower $\sqrt{s_{NN}}$ from CERN SPS and AGS experiments, and $p + p$ and $p + \bar{p}$ collisions over a broad range of energy. In comparing to results from lower energy $A + A$ collisions, we note that all of those experiments were fixed target experiments and their results on the distribution of charged particles need to be first transformed to the center of mass system, in order to make a meaningful comparison with our collider based data. Experiment NA49 at the CERN SPS and E866/E917 at AGS both measure dN/dy distributions and $\langle p_T \rangle$ for identified particles, which allows us to consistently convert their results into $dN_{ch}/d\eta$ via the relation:

$$\frac{dN_{ch}}{d\eta} = \sqrt{1 - \frac{m_0^2}{m_T^2 \cosh^2 y}} \frac{dN_{ch}}{dy}$$

The WA98 experiment at CERN SPS however, measures only $dN_{ch}/d\eta$ in the lab system without particle identification and $\langle p_T \rangle$ information. To transform their results to the center of mass frame, we are forced to apply an *ad hoc* scale factor of 1.18, based on the assumption that $\langle p_T \rangle$ doesn't change much from the NA49 results at the same energy and the net result of consistent transformation of the NA49 results from lab frame to center of mass frame was an increase by 1.18 in $dN_{ch}/d\eta$ at $\eta = 0$.

Fig. 6-7a shows that the scaled charged particle yield at $\eta = 0$ seems to evolve smoothly from that at lower $\sqrt{s_{NN}}$; the hoped for sudden increase in the yield of charged particles due to liberation of quark gluon degrees of freedom is noticeably absent. This does not mean however, that $A + A$ collisions at these energies can be regarded as simple superpositions of elementary NN collisions either, since the yield scaled by $\langle N_{part}/2 \rangle$ is much larger than that observed in $p + p$ collisions at similar energies: $A + A$ collisions at $\sqrt{s_{NN}} = 200$ GeV

produce on average 55% more charged particles at mid-rapidity compared to $p + p$ collisions at a similar energy.

Further insight into the possible particle production processes in heavy ion collisions is provided by Fig. 6-7b, where the centrality dependence of the scaled charged particle yield $dN_{ch}/d\eta$ at $\eta = 0$ is shown as a function of $\langle N_{part} \rangle$ for both $\sqrt{s_{NN}} = 130$ GeV and $\sqrt{s_{NN}} = 200$ GeV. Also shown in open symbols is the yield in $p + \bar{p}$ at the the two energies. The $p + \bar{p}$ yield at $\sqrt{s_{NN}} = 200$ GeV is a direct measurement by the UA5 experiment at CERN SPS[116], but the yield at $\sqrt{s_{NN}} = 130$ GeV is an interpolation from yields at other energies (cf. Fig. 6-7a), since there are no direct measurements in $p + \bar{p}$ collisions at $\sqrt{s_{NN}} = 130$ GeV.

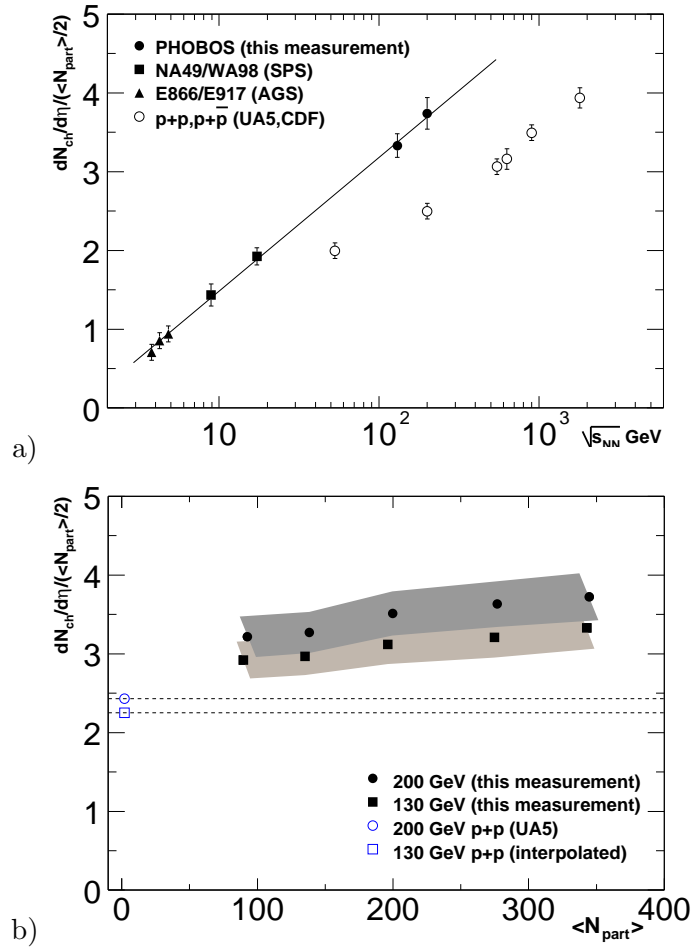


Figure 6-7: $dN_{ch}/d\eta / \langle N_{part} \rangle / 2$ at $\eta = 0$: (a) as a function of $\sqrt{s_{NN}}$ for central (0-6%) collisions, including measurements in $A + A$ collisions at lower energy[61, 62] and $p + p$ [123] and $p + \bar{p}$ collisions[124, 125]. Straight line is drawn to guide the eye. (b) as a function of $\langle N_{part} \rangle$ for $\sqrt{s_{NN}} = 130$ GeV and $\sqrt{s_{NN}} = 200$ GeV

The impact parameter, or equivalently, N_{part} dependence of the yields provides a very sensitive handle on the interplay of soft and hard processes in the collision, since the former scale directly with N_{part} , while the latter scale with the number of binary collisions N_{coll} which, in turn has a power dependence $\propto N_{part}^\alpha$ in the Glauber picture of nuclear collisions. The baseline on this dependence is set by the yield in $p + \bar{p}$ collisions, which our results systematically exceed. The ratio of the yield in Au+Au collisions to that in $p + \bar{p}$ grows larger for central collisions and reaches up to an excess of 55% in the most central collisions at $\sqrt{s_{NN}} = 200$ GeV as shown in Fig. 6-7b. While this broadly points to the increasing importance of hard processes in central Au+Au collisions which scale faster than N_{part} , further conclusions have to await comparison with phenomenological models in section 6.3.

6.1.4 Total N_{ch}

Fig. 6-8 shows the scaled pseudo-rapidity distributions $dN_{ch}/d\eta'/\langle N_{part}/2 \rangle$ in central Au+Au collisions, in comparison to the NA49 measurement[126] in Pb+Pb collisions at a lower $\sqrt{s_{NN}} = 17$ GeV³. The excellent agreement in the fragmentation region, along with the limiting curve behaviour already discussed, allows us to smoothly extrapolate our measured $dN_{ch}/d\eta$ distribution out beyond the $|\eta| < 5.4$ limit of the acceptance of our apparatus. We do this by a constrained fit of a Woods-Saxon function⁴ to the $dN_{ch}/d\eta'/\langle N_{part}/2 \rangle$ and thereby extract the integrated charged multiplicity distribution.

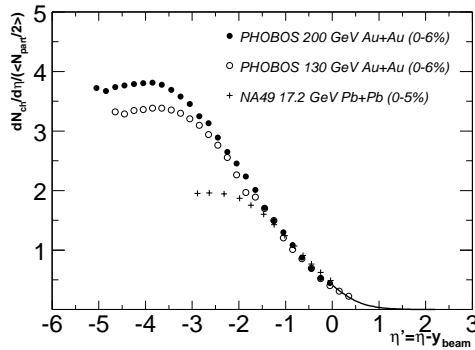


Figure 6-8: Comparison of scaled $dN_{ch}/d\eta'$ with NA49 measurements at $\sqrt{s_{NN}} = 17$ GeV. Woods-Saxon fit is also shown.

³The PHOBOS experiment has also measured $dN_{ch}/d\eta$ in Au+Au collisions at $\sqrt{s_{NN}} = 19.6$ GeV during a brief running period at the end of PR01. The result is consistent with that of NA49, but is not included in this comparison since it was not performed by the author and is still preliminary at the time of writing this thesis

⁴The Woods-Saxon function is used here without any physical justification, merely as convenient functional form that seems to describe the data well

The value of N_{ch} obtained by this procedure, scaled by $\langle N_{part}/2 \rangle$, is plotted in Fig. 6-9, again as a function of $\sqrt{s_{NN}}$ for central Au+Au collisions(a), and as a function of centrality at $\sqrt{s_{NN}} = 130$ GeV and $\sqrt{s_{NN}} = 200$ GeV(b). The data from lower energy A + A, $p + p$ and $p + \bar{p}$ collisions is also displayed in a manner similar to the one used earlier in Fig. 6-7.

Fig. 6-9a indicates that like the mid-rapidity yields, the total yield of charged particles per participating nucleon evolves smoothly as a function of $\ln\sqrt{s}$ from A + A collisions at lower center of mass energies, but shows a significant excess from $p + p$ results at similar energies. No significant increase in $N_{ch}/\langle N_{part}/2 \rangle$ due to liberation of quark gluon degrees in a phase transition to the QGP phase at a threshold $\sqrt{s_{NN}}$ is observed.

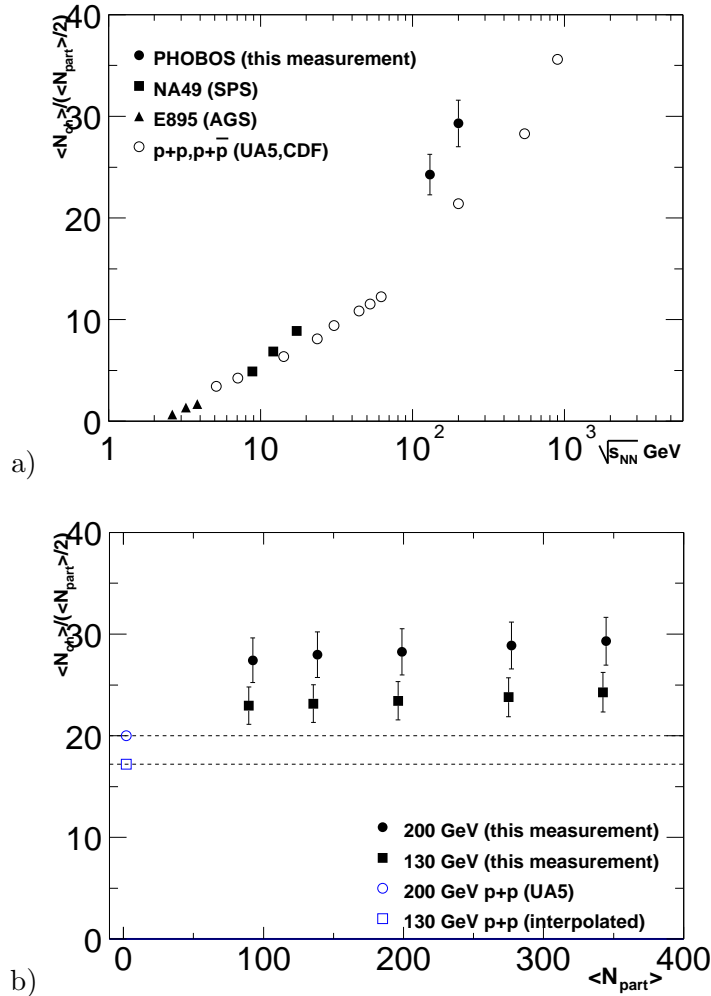


Figure 6-9: The integrated N_{ch} yield, scaled by $\langle N_{part}/2 \rangle$. (a) as a function of $\sqrt{s_{NN}}$ in central (0-6%) collisions, including data from other experiments[61, 62] and (b) as a function of centrality (N_{part}), including a comparison to the integrated yield in $p + \bar{p}$ [49] collisions at the two energies

Surprisingly, we find that $N_{ch}/\langle N_{part}/2 \rangle$ approximately scales with N_{part} , as indicated in Fig. 6-9b. The integrated charged particle yield per participating nucleon pair in Au+Au collisions, after jumping up from its value in $p + \bar{p}$ collisions, seems to remain nearly constant as a function of impact parameter. This is especially puzzling in light of the faster-than- N_{part} scaling observed in the mid-rapidity charged particle yields (Fig. 6-7b). It is hard to imagine physical processes in heavy ion collisions extending over twelve units of rapidity space ($-6 \lesssim y \lesssim 6$) that cause the scaled pseudo-rapidity distribution to evolve smoothly with variation in impact parameter, in such a way that the fast rise in the mid-rapidity yield is somehow compensated by a reduction of yields at forward rapidities and the total integral N_{ch} per participant pair remains approximately constant as a function of centrality!

6.2 Systematic Checks

It is important to ensure that the interesting features observed in our pseudo-rapidity distributions are not artifacts of some systematic effect in the analysis. This section aims to convince the reader that such is not the case, and provides details of how the systematic error bands seen on figures in the previous section are computed.

The systematic error on the measurement of the mean number of participants $\langle N_{part} \rangle$ for each centrality bin has already been presented earlier in chapter 4, and will not be discussed further here, except in noting that wherever distributions are scaled by $\langle N_{part}/2 \rangle$, the error on $\langle N_{part} \rangle$ is added in quadrature to the total systematic error, which is shown as a band around the data points to take into account the systematic error on the horizontal scale.

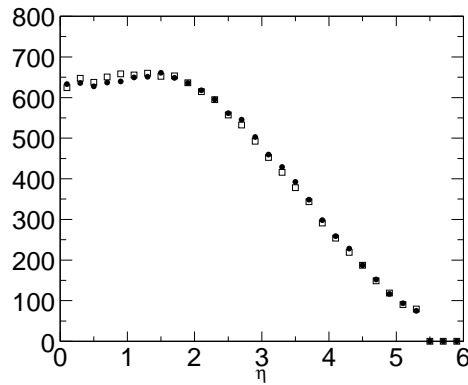


Figure 6-10: $dN_{ch}/d\eta$ for $\eta > 0$ (\bullet) versus $\eta < 0$ (\square) reflected about $\eta = 0$ in central Au+Au collisions at $\sqrt{s_{NN}} = 200$ GeV. Data for other centrality bins and $\sqrt{s_{NN}} = 130$ GeV is similar.

Due to the nearly 4π coverage of the PHOBOS multiplicity detector and the fact that for an Au+Au collision at RHIC the laboratory system is the same as the center of mass system, we have the luxury of coverage for measurement of charged particles extending over nearly eleven units of pseudo-rapidity $-5.4 < \eta < +5.4$. In particular, this allows us to compare results obtained for $\eta < 0$ with $\eta > 0$ in the same apparatus as shown in Fig. 6-10. Although such a comparison of $dN_{ch}/d\eta$ provides no new information, and hence cannot be used as an input in the systematic error estimation, it does assure that we have not made any gross mistakes in the analysis. The distribution of secondary-producing dead material in the apparatus is assymmetric around $\eta = 0$ since the bulk of the PHOBOS magnet is located over $0 < \eta < 1$. Fig. 6-10 indicates that our background correction factors take this asymmetry into account.

With this preliminary observation, we next consider three possible sources of systematic error in the analysis.

6.2.1 Detector effects

Baseline Shifts:

A possible source of systematic bias is the occurrence of baseline shifts in the multiplicity sensors, discussed earlier in chapter 3. The shifts are caused by large signal in a single pad being capacitively coupled to most of the other pads in the same row over which the trace line carrying the signal runs. This leads to the baseline in the adjacent pads being shifted by a finite amount, which is corrected for in the offline signal processing. The frequency of such baseline shifts, and the efficiency with which the signal processing corrects for them depends on the flux of charged particles traversing the sensor.

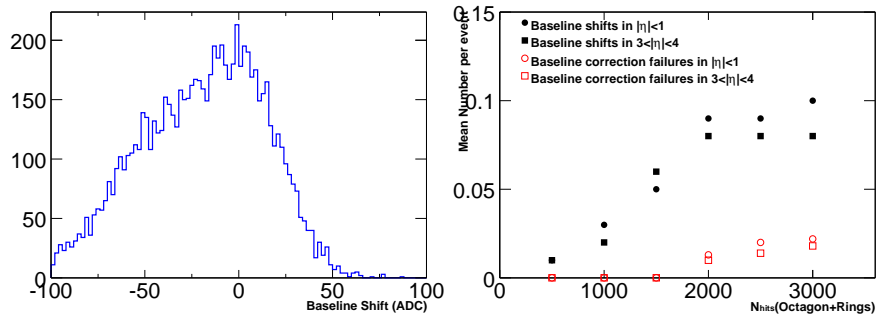


Figure 6-11: (a) Frequency distribution of baseline. (b) Mean number of baseline shifts per event as a function of N_{hits} . Data is for the high occupancy regions $-1 < \eta < 1$ and $3 < |\eta| < 4$ at $\sqrt{s_{NN}} = 200$ GeV

Fig. 6-11 shows the number of such shifts found and corrected by the signal processing as a function of total N_{hits} at $\sqrt{s_{NN}} = 200$ GeV at $-1 < \eta < 1$ (central part of the octagon) and at $3 < |\eta| < 4$ (first ring detectors), where detector occupancy is at a maximum. Also shown is the number of *unsuccessful* cases where the signal processing returned an indefinite answer, *i.e.*, where the number of empty channels in the row was insufficient to correct for the baseline shift. Baseline shift correction is straightforward in other regions of the detector, where occupancy is lower and the hit-merging procedure provides additional discrimination against such ‘lit-up’ rows.

In the normal multiplicity analysis, all events containing baseline-shifted rows of the latter type are discarded, since we are not limited by statistics and it would be much harder to remove the specific row and account for the changed acceptance on an event-wise basis. From Fig. 6-11 it is clear that even in the worst case scenario of central Au+Au collisions, we have on average 0.1 baseline shifts in the high occupancy region per event. Since baseline shifts are caused by a hardware effect that cannot be modelled in the simulation, it is difficult to estimate the true efficiency of the signal processing analysis in trapping all such shifts.

In order to estimate how these baseline shifts affect our measurement of $dN_{ch}/d\eta$, we have compared the distributions of hit-pads $dN_{hits}/d\eta$ in the two regions $-1 < \eta < 1$ and $3 < |\eta| < 4$ obtained from events in the normal data sample, to one which *includes* also events where the signal processing returned an unsuccessful flag. We find that the resulting $dN_{hits}/d\eta$ distribution changes by less than 2%; this change is commensurate with the point-to-point scatter in the distribution itself. The observed frequency of baseline shifts in the central rapidity region, combined with the fact that in averaging our distribution over ϕ , we are including at least 4 sensors \times 4 rows/sensor, implies that a baseline shift in any one row would be statistically suppressed, if we were to include such events in our analysis.

Gain Calibration:

In principle, systematic errors in the gain calibration of individual pads in the detector could cause the measured energy response in such pads to introduce spurious counts into the number of hit pads. We have reasons to assert that this is not the case. The gain calibration procedure has been described earlier in chapter 3, and although the response of detector pads shows some signs of saturation when it gets into the high (> 60 MIP) range, it is very linear near the 1 MIP range, where all our threshold cuts are placed. Further, any

pads not conforming to such a linear gain response, including pads that have high intrinsic electronic noise, are explicitly marked non-functional, taken out of the detector acceptance and removed from the analysis. Of the remaining functional, calibrated channels, if some develop pathologies that are not accounted for in the dead pad map over the data taking period, then the averaging over many pads distributed in azimuth ϕ in the reconstruction of $dN_{hits}/d\eta$ ensures that such pads become statistically insignificant (there are at least ~ 48 pads per $\delta\eta = 0.2$ bin near $\eta = 0$).

Given the fact that less than 5% of pads in the installed multiplicity detector had pathologies to begin with (that were masked out by the dead pad map), and frequent gain and noise calibration runs performed during the running period indicated that this fraction remained nearly constant, we have estimated the effect of systematic error due to gain miscalibration of individual pads by running different subsets of the analysis with the wrong dead pad maps (Dead pad map for $\sqrt{s_{NN}} = 130$ GeV data applied to the $\sqrt{s_{NN}} = 200$ GeV analysis and vice versa, etc) and found that the reconstructed $dN_{hits}/d\eta$ distribution changes by less than 1%.

A separate issue regarding gain calibrations, is that of the absolute calibration of the MIP energy scale in the data. It has very little direct connection to this measurement, since we rely on the *relative* calibration among an ensemble of pads in the hit counting procedure to decide which pads have hits. We have noted earlier in chapter 3 a discrepancy at the level of 10% between the measured location of the MIP peak in data-derived Landau distributions (calibrated with the electronics response of our front end electronics) and the corresponding MIP peak location provided by GEANT based MC simulations. The simulations use the Bethe-Bloch parameterization of energy loss by charged particles in a thin layer of silicon. Such a discrepancy, while being immaterial to this measurement, could become problematic for other measurements relying on an accurate dE/dx measurement in the silicon, accompanied by MC simulations to determine corrections.

Hit merging and Hit pad counting

As discussed in chapter 5, the multiplicity reconstruction relies on a system of threshold cuts to identify hit pads in the multiplicity detector. The values of these threshold cuts are arrived at through detailed consistency checks within the data, as well as through comparison with GEANT simulations of the detector response. We have varied all the cut parameters around their nominally set value to determine their effect on the reconstructed

$dN_{hits}/d\eta$ distribution.

Of the various cut parameters described in chapter 5, we find that the hit reconstruction procedure has the highest sensitivity to $\delta E_{maxmerge}^{oct}$ which determines the threshold over which a pad is regarded as an independent hit rather than a shared part of a hit in the adjacent pad. By varying its value from 40 keV to 70 keV (the nominal value is 55 keV), we find that the $dN_{hits}/d\eta$ distribution changes systematically by 6%. At the low extreme, the contribution of noise hits causes the count to increase. At the high extreme, we start approaching the single hit MIP peak and the count decreases due to multiple single hits being wrongly combined into a merged hit. Beyond a quasi-plateau behaviour in $dN_{hits}/d\eta$ over this range of variation in $\delta E_{maxmerge}^{oct}$, the results diverge rapidly. In addition, the $dN_{hits}/d\eta$ distributions are affected at less than 1% level by variations in any of the other cut parameters, keeping the $\delta E_{maxmerge}^{oct}$ cut fixed at 55 keV.

As a result of these studies, we assign a combined systematic error of 6% arising from dependence on hit merging and hit pad counting parameters; this turns out to be the dominant source of systematic error in our measurement of $dN_{ch}/d\eta$.

6.2.2 Occupancy effects

It is possible that in case of very high detector occupancy the assumption of Poisson statistics in the calculation of occupancy corrections stops being valid. We have demonstrated in chapter 5 that the highest occupancy reached in the central part of the octagon detector at $\sqrt{s_{NN}} = 200$ GeV is still not enough to saturate the number of hit pads: $\sim 20\%$ of the pads on average remain without hits and are useful in determining the Poisson statistics-based occupancy correction. As a cross-check, we evaluate the occupancy correction by fitting contributions to the Landau spectrum of energy signals in individual pads from second and third MIP peaks caused by double and single hits in the same pad.

The difference in the corrections derived from these two separate methods is of the order of 3%, over most of the centrality and η range, though corrections derived from the latter method are prone to occasional jumps (see Fig. 5-13) due to unstable fit results.

6.2.3 Secondary particles and Decays

The main drawback of performing a multiplicity measurement using a single layered detector like the PHOBOS multiplicity array is the loss of discriminatory power against secondary

particles not produced in the the primary collision. In a tracking detector like the spectrometer or vertex detector, a substantial reduction of such secondary tracks can be achieved by requiring the reconstructed tracks to point back to the primary collision vertex. In our measurement, we effectively integrate over the Landau distribution of energy signals measured in the multiplicity detector pixels, and rely on sub-MIP threshold cuts on the distribution to discriminate against the background particles originating far from the vertex (mostly in the beam-pipe). An indirect estimate of secondary particles left-over after this procedure is obtained by applying the reconstruction algorithm to a HIJING+GEANT Monte Carlo simulation, and comparing the reconstructed pseudo-rapidity distribution to the input primary particle distribution. It is therefore necessary to check that such an indirect background estimation yields sensible results, and calculate the systematic error introduced by this procedure.

In checking the consistency of the multiplicity reconstruction procedure purely within the simulation, we merely need to check that the algorithm scales linearly with the number of primary particles input to the simulation. Given a p_T distribution of primary particles,

$$\left. \frac{dN_{ch}}{d\eta} \right|_{reconstructed}^{MC} \propto \left. \frac{dN_{ch}}{d\eta} \right|_{primary}^{MC}$$

To estimate a systematic error, we need to first ensure that the above proportionality relation is obeyed by our GEANT based simulation of the detector's response. Further, secondary particle production in the beam pipe, while primarily dependent on the number of primaries, may also depend on the p_T distribution of the primaries: a disproportionately large number of low p_T primaries, for example, would produce a larger number of secondaries through multiple scattering and hence affect the value of the proportionality constant in the above relationship.

The first of these checks is shown in Fig. 6-12, where we have plotted the reconstructed $dN_{ch}/d\eta$ distribution in HIJING+GEANT simulations against the primary particle input $dN_{ch}/d\eta$ from HIJING. The plots show a linear relationship between the two quantities for different η values corresponding to different sections of the detector with different quantities of intervening back-ground producing dead material, thus verifying the above proportionality.

A second check on the role of particular p_T distribution assumptions from HIJING, is

made by performing a similar reconstruction procedure on input from other event generator models. RQMD and VENUS are used; these models have vastly different primary particle yields and p_T distributions from those in HIJING. The results of these comparisons with different event generator models has already been exhibited in Fig. 5-16. We find a maximum of 5% variation in the proportionality factors derived from these three simulations, which serves as a conservative systematic error estimate from this aspect of the reconstruction procedure.

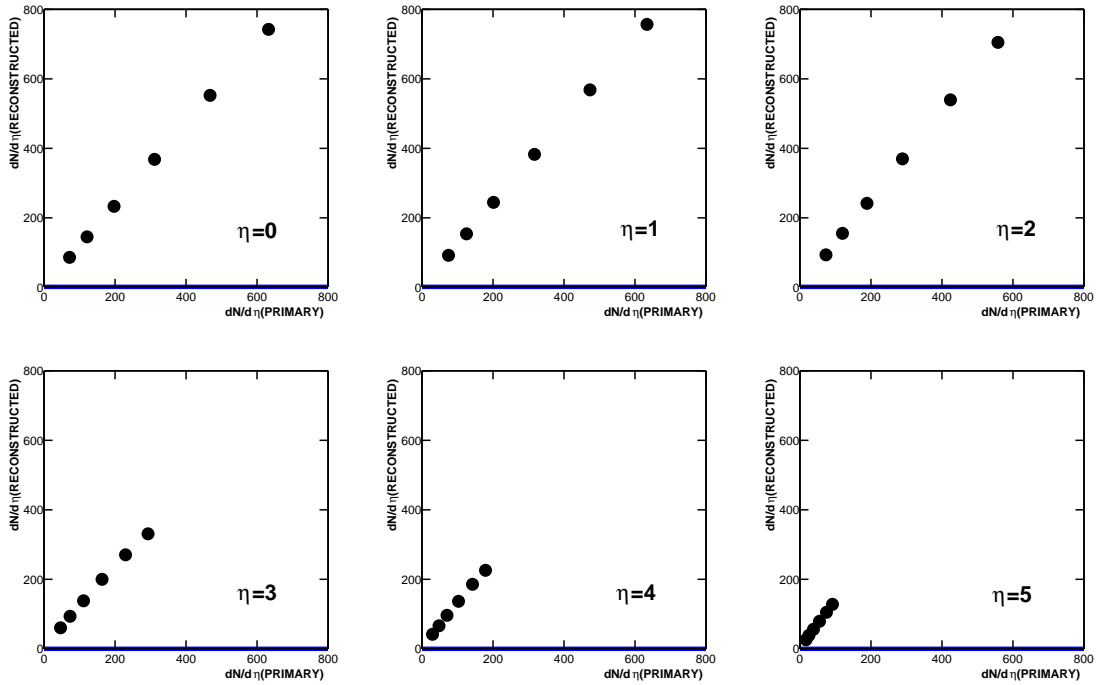


Figure 6-12: Comparison of $dN_{ch}/d\eta^{\text{reconstructed}}$ to $dN_{ch}/d\eta^{\text{primary}}$ from HIJING, for different values of η to demonstrate linear proportionality. $+(-)\eta$ results are averaged for each η value indicated.

6.2.4 Summary of systematic errors

Table 6.2 summarizes the systematic errors obtained in the previous sections, and provides the combined systematic error on the measurement. The numbers shown in this table are for central collisions at $\sqrt{s_{NN}} = 200$ GeV and represent a worst-case estimate. Some of the errors are lower for more peripheral collisions and at lower $\sqrt{s_{NN}}$, due to lower detector occupancy.

Further some the errors in Table 6.2 are correlated: the error from threshold cuts used in

the merging procedure is correlated with the one from the MC background estimation, since the MC reconstruction uses the same threshold cuts. Similarly the occupancy correction is multiplied into the N_{hits} determined from the hit merging procedure. The errors are here added in quadrature to preserve the worst-case scenario.

Effect	Systematic Error
Baseline shifts	2%
Gain Calibration	<1%
Hit Merging threshold cuts	6%
Occupancy corrections	3%
Background correction from MC	5%
Total	8%

Table 6.2: Summary of systematic errors from various sources for central Au+Au collisions at $\sqrt{s_{NN}} = 200$ GeV. The errors at other centralities and at lower energy are similar.

6.3 Comparison with models

In order to gain further insight into the relative importance of different types of physical processes involved in a relativistic heavy ion collisions, it is useful to compare our results with predictions from different models of the collision. A few such models have been described in the introductory chapter, we now perform a post-mortem of how their predictions hold up against our measurements.

6.3.1 HIJING

Fig. 6-13 shows the measured charged particle pseudo-rapidity distribution in central collisions at the two energies as points, overlaid on results predicted by the HIJING event generator code[127]. HIJING version 1.35 with default parameters is used.

As discussed in chapter 1, HIJING is a model of nuclear collisions ‘inspired’ by perturbative-QCD, which uses hadronic spectra in $p + p$ collisions as the baseline. $A + A$ collisions are modelled using primarily partonic degrees of freedom, with jet production and parton energy loss in a nuclear medium playing a central role. Each nucleon-nucleon collision produces mini-jets, with p_T or the order of a few GeV/c, which rapidly lose energy through multiple scattering in the dense surrounding nuclear medium. Such ‘jet quenching’

leads to modification of the moderate and high p_T spectrum of produced particles. Since jet quenching also converts hard partons into a number of softer partons, it leads to an enhancement of particle production in the mid-rapidity region, accompanied by a reduction of the yield in the fragmentation regions. Fig. 6-13 indicates that broad qualitative features of the measured pseudo-rapidity distribution are reproduced well by the HIJING model. At mid-rapidity in central collisions in particular, where perturbatively calculable hard processes are important, the agreement is quite good and becomes better at higher $\sqrt{s_{NN}}$. The measured distribution is slightly wider than that expected from HIJING.

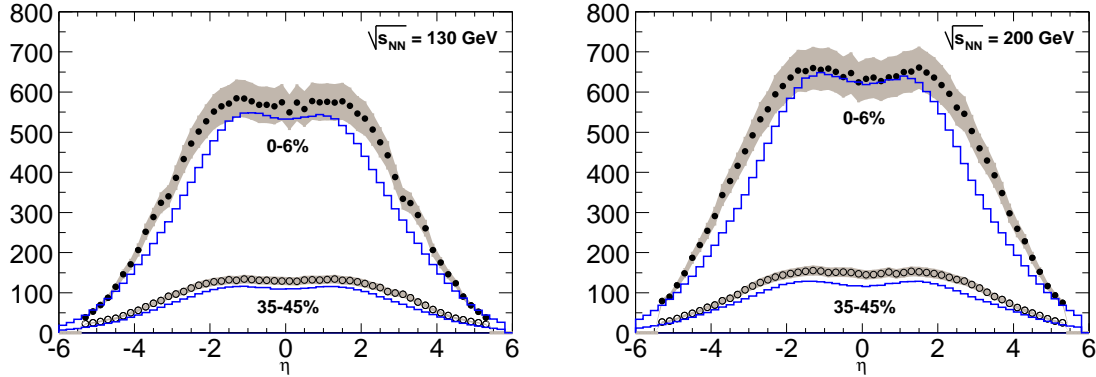


Figure 6-13: Comparison of measured $dN_{ch}/d\eta$ (symbols) to predictions from the HIJING model for (a) $\sqrt{s_{NN}} = 130$ GeV and (b) $\sqrt{s_{NN}} = 200$ GeV

Jet quenching in $A + A$ collisions in comparison to $p + p$ collisions is of interest because it provides information on final state interaction processes that may lead to thermal and chemical equilibrium of the produced dense partonic system. With increasing collision energy, hard processes are expected to become increasingly important for particle production near mid-rapidity. The mean parton energy loss in the nuclear medium dE/dz is a significant parameter of the model dynamics and comparison to the measured $dN_{ch}/d\eta$ distribution places constraints on the allowed values of dE/dz . The default parameter set of HIJING 1.35 as shown in Fig. 6-13 assumes $dE/dz = 2$ GeV/fm. In [128], it is argued that by increasing the parton energy loss dE/dz in the model, *i.e.*, by allowing the partons to lose more energy in a dense colored medium, the agreement to the measured mid-rapidity $dN_{ch}/d\eta$ yields is further improved.

There is a second parameter which plays a major role in determining the yields predicted by HIJING. This is the distribution of partons, and in particular, gluons in the nucleus in

the initial state. Parton dynamics in HIJING is modelled using the distribution functions of partons inside nucleons. In heavy ion collisions at high energy, these distribution functions can be significantly modified due to ‘shadowing’[129]. The term shadowing refers to a depletion of the gluon density at low x , where x is the fraction of longitudinal momentum carried by each gluon. At high energies, small x gluons have large wavelengths compared to the Lorentz contracted nucleus size. Therefore, small x gluons from different nucleons can spatially overlap and recombine into a higher x gluon. This leads to a depletion of the gluon density at small x , compared to the naïve expectation for the parton distribution function in a nucleus to be simply proportional to the one in a nucleon.

In terms of the effect on the charged particle yields, such nuclear shadowing has the opposite effect from minijet production and jet quenching: the latter tends to increase the number of produced particles in the final state through energy loss of partons, while the former reduces the number of partons in the initial state. The effect of these two opposing trends can be resolved by studying the p_T spectrum of the produced charged particles, at large values of p_T where the effect of minijets and jet energy loss can be seen unambiguously[130].

6.3.2 Two component fit: Hard versus soft processes

The measurement of $dN_{ch}/d\eta$ as a function of centrality of collisions as parametrised by N_{part} offers an important handle on the interplay of coherent soft or low momentum transfer parton collisions with incoherent hard processes involving large momentum transfers. The former are assumed to be proportional to the number of participating nucleons N_{part} , while the latter primarily scale with the number of binary collisions N_{coll} among the nucleons. In an eikonal approximation developed in [131], these two contributions can be treated as additive, and the data fitted with a function of the form:

$$\frac{dN_{ch}}{d\eta} = (1 - x) n_{pp} \frac{\langle N_{part} \rangle}{2} + x n_{pp} \langle N_{coll} \rangle \quad (6.1)$$

where x is the fraction of multiplicity n_{pp} measured in $p + p$ collisions due to hard processes and $(1 - x)$ is the remaining contribution due to soft processes. N_{part} and $N_{coll} \sim N_{part}^{\frac{4}{3}}$ are numerically calculated using the Glauber model of nuclear collisions[132]. x and n_{pp} are left as free parameters in the fit, with the expectation that the fitted n_{pp} agree with the

measured particle multiplicity in $p+p$ collisions. Fig. 6-14 shows the result of this fit against the measured $dN_{ch}/d\eta/\langle N_{part}/2 \rangle$ at $\eta = 0$ for $\sqrt{s_{NN}} = 130$ GeV and $\sqrt{s_{NN}} = 200$ GeV. The fitted values of n_{pp} agree quite well with the measured values of charged particle multiplicity in $p+p$ collisions.

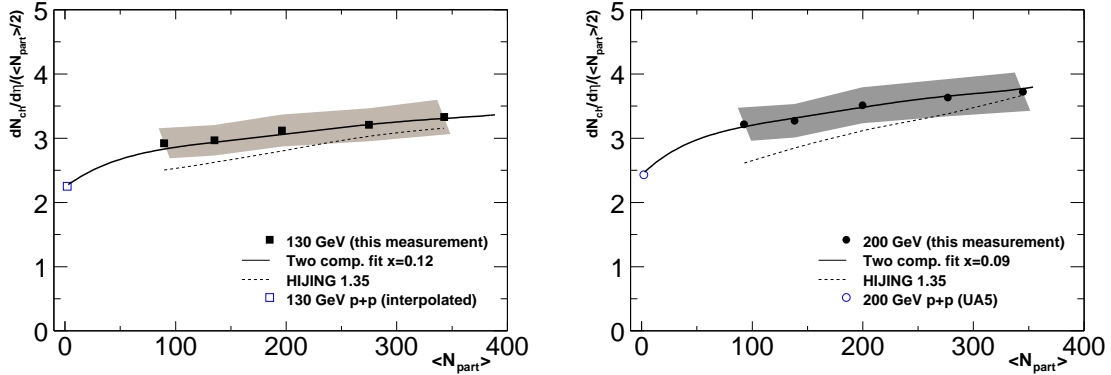


Figure 6-14: Measured $dN_{ch}/d\eta/\langle N_{part}/2 \rangle$ near $\eta = 0$ (symbols) fitted with the two-component fit function Eqn. (6.1) (lines) for (a) $\sqrt{s_{NN}} = 130$ GeV and (b) $\sqrt{s_{NN}} = 200$ GeV. Predictions from the HIJING simulation are also shown as dashed lines.

The values $x_{130} = 0.09$ and $x_{200} = 0.12$ obtained from the fit indicate that the contribution of hard processes to particle production is significant at these energies. The limit $x = 0$, corresponds to the ‘wounded nucleon’ model which has purely N_{part} scaling of particle production from predominantly soft processes. Our data on $dN_{ch}/d\eta/\langle N_{part}/2 \rangle$ near $\eta = 0$ shows a significant N_{coll} component to its N_{part} dependence, which could be interpreted[131] as an increasing contribution from hard processes at mid-rapidity at these high energies.

However, a strong conclusion like this requires comparison to the centrality dependence of $dN_{ch}/d\eta/\langle N_{part}/2 \rangle$ near $\eta = 0$ from lower energy A+A collisions, where hard processes presumably contribute little to the collision dynamics. In addition, it needs to be placed in context with the evolution of the full $dN_{ch}/d\eta/\langle N_{part}/2 \rangle$ distribution over $-5.4 < \eta < 5.4$, and in particular, the weak dependence on N_{part} shown by the integrated charged particle yield $\langle N_{ch} \rangle$ as discussed in Section 6.1.4.

The HIJING simulation discussed earlier, essentially measures the same balance between soft and hard processes using microscopic parton dynamics. Indeed, in [133], the authors identify particle production from hard processes with minijet cross sections and expect the

mid-rapidity charged particle yield to have a dependence:

$$\frac{dN_{ch}}{d\eta} = \langle n_{soft} \rangle \langle N_{part} \rangle + f \frac{\sigma_{jet}^{AA}(s)}{\sigma_{incl}^{NN}} \langle N_{coll} \rangle \quad (6.2)$$

which resembles Eqn. (6.1). The soft component $n_{soft} \sim 1.3$ arises from string fragmentation in HIJING, and hard processes like mini-jet production add the N_{coll} component. $\sigma_{jet}^{AA}(s)$ is the energy-dependent average inclusive minijet cross section per binary NN collision in an $A + A$ collision and $f \sim 1.2$. The predictions from HIJING simulation for the scaled mid-rapidity charged particle yield $dN_{ch}/d\eta/\langle N_{part}/2 \rangle$ is also shown in Fig. 6-14. Within systematic errors, it matches the qualitative features of N_{part} dependence in the data like the phenomenological two component fit, which is not surprising considering the strong resemblance between the scaling behaviour in Eqn. (6.1) and Eqn. (6.2).

6.3.3 Semi-classical QCD dynamics

The semi-classical QCD picture of multi-particle production in heavy ion collisions developed by Kharzeev and Nardi[80] has already been introduced in chapter 1. Such an approach is attractive because of its relative simplicity and lack of parameters. It relies on the basic idea that ultra-relativistic heavy ion collisions produce thousands of particles. Due to the high (saturated) densities of partons in the colliding nuclei, quantum fluctuations become insignificant and the system's evolution is governed primarily by the classical configuration of color fields.

The rapidity distribution of gluons, after taking into account their saturated phase space density is obtained to be:

$$\begin{aligned} \frac{dN_g}{dy} &= c N_{part} \left(\frac{s}{s_0} \right)^{\frac{\lambda}{2}} e^{-\lambda|y|} \left[\ln \left(\frac{Q_s^2}{\Lambda_{QCD}^2} \right) - \lambda|y| \right] \times \\ &\times \left[1 + \lambda|y| \left(1 - \frac{Q_s}{\sqrt{s}} e^{(1+\lambda/2)|y|} \right)^4 \right] \end{aligned}$$

where the saturation scale Q_s depends on the center of mass energy of the collision s : $Q_s^2(s) = Q_s^2(s_0) (s/s_0)^{\lambda/2}$. The exponent $\lambda = 0.25$, is extracted from the measured gluon distribution functions at HERA. Once the energy-independent constant $c \sim 1$ and $Q_s^2(s_0)$ are determined at some energy s_0 , the above equation is free of any parameters. The

final yield of charged particles is assumed to be simply proportional to the initial gluon distribution with no provision for final-state production. The pseudo-rapidity distribution is obtained by applying a Jacobian to the above equation.

Fig. 6-15 shows a comparison of the measured $dN_{ch}/d\eta$ distributions with predictions from this semi-classical approach at two energies $\sqrt{s_{NN}} = 130$ GeV and $\sqrt{s_{NN}} = 200$ GeV. The data show remarkable agreement with the predictions, out to $|\eta| \sim 4$.

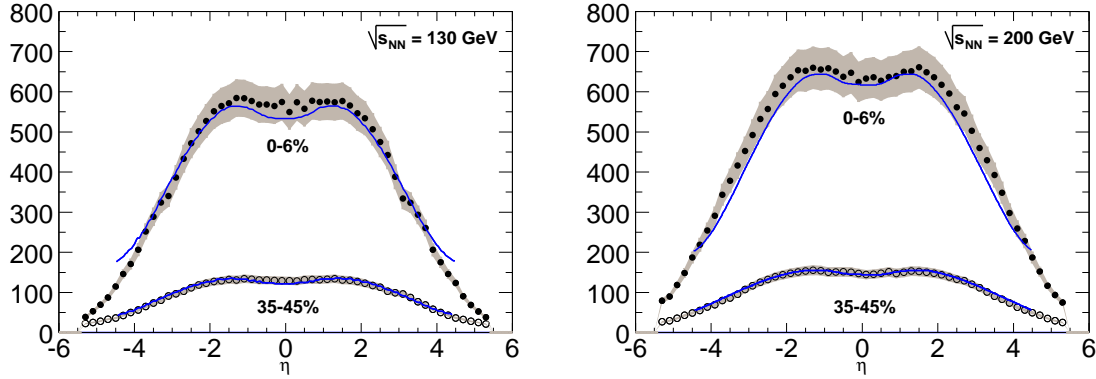


Figure 6-15: Comparison of measured $dN_{ch}/d\eta$ (symbols) to predictions from the semi-classical QCD based approach of Kharzeev et al (lines) for (a) $\sqrt{s_{NN}} = 130$ GeV and (b) $\sqrt{s_{NN}} = 200$ GeV

Also shown in Fig. 6-16 is a comparison of the scaled mid-rapidity charged particle yields with at $\sqrt{s_{NN}} = 130$ GeV and $\sqrt{s_{NN}} = 200$ GeV with that predicted in this approach. The agreement is again particularly striking, especially since at $y = 0$, the above equation for dN_g/dy reduces to a simple $\ln(Q_s^2/\Lambda_{QCD}^2)$ dependence. Hence the mid-rapidity charged particle yield in this approach is determined solely by the running of the QCD strong coupling constant α_S .

In view of the broad agreement with our data shown by both a semi-classical QCD approach using initial state gluon saturation, as well as a perturbative-QCD approach based on the interplay of soft and hard (minijet) processes, we have to think of further tests to distinguish which of these two radically different pictures is applicable in reality to the physics of heavy ion collisions.

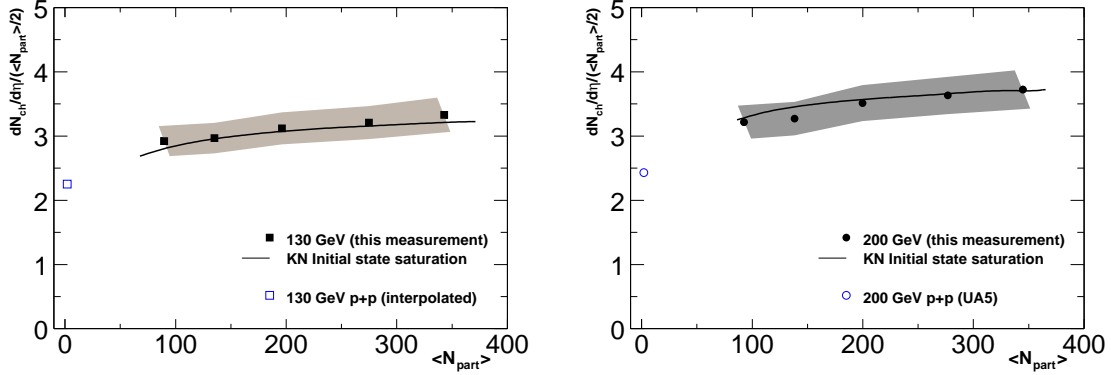


Figure 6-16: Measured $dN_{ch}/d\eta/\langle N_{part}/2 \rangle$ near $\eta = 0$ (symbols) compared with predictions from the semi-classical QCD approach of Kharzeev et al (lines) for (a) $\sqrt{s_{NN}} = 130$ GeV and (b) $\sqrt{s_{NN}} = 200$ GeV.

The main feature of the classical emission is that it is coherent up to the transverse momenta of the order of the saturation scale Q_s ($\simeq 1 - 2$ GeV/c for central Au+Au collisions). This implies that if we look at the centrality dependence of particle multiplicities above a certain transverse momentum, say, $p_T > 1$ GeV/c, it should be very similar to the dependence without the transverse momentum cut-off. On the other hand, in the two component “soft plus hard” model such a cut on the transverse momentum would strongly enhance the contribution of hard minijet production processes, since soft production mechanisms presumably do not contribute to particle production at high transverse momenta. At sufficiently large value of the p_T cut-off, all of the observed particles will originate from genuine hard processes, and the centrality dependence will become steeper, reflecting the scaling with the number of collisions.

6.4 Conclusions

We have presented results on the pseudo-rapidity distribution of charged particles in Au+Au collisions at $\sqrt{s_{NN}} = 130$ GeV and $\sqrt{s_{NN}} = 200$ GeV and discussed its dependence on the centrality of the collision. The density at mid-rapidity and the total number of charged particles both evolve smoothly as a function of centrality and beam energies without any sudden increase, and extrapolate well to earlier measurements in $A + A$ systems at lower $\sqrt{s_{NN}}$. The yields at $\eta = 0$ scaled by $\langle N_{part}/2 \rangle$ are significantly larger than those in $p + p$ and $p + \bar{p}$ collisions at similar energies, upto 55% at $\sqrt{s_{NN}} = 200$ GeV. A limiting

behaviour similar to limiting fragmentation is observed in the pseudo-rapidity distribution as a function of $\sqrt{s_{NN}}$: the yield near beam rapidity appears to approach a universal curve for each centrality class, extending over two units of rapidity. As we go from peripheral to central collisions, the pseudo-rapidity distribution appears to narrow, the yield in the fragmentation region decreases, with a commensurate increase in the yield at mid-rapidity such that the integrated yield N_{ch} remains nearly constant as a function of centrality.

The results were compared to three theoretical models, one of which is the microscopic model HIJING, which employs mini-jet production from partons and subsequent jet energy loss to predict charged particle yields. The second comparison was with a two-component fit inspired by HIJING, to extract the approximate fraction of soft processes (scaling with N_{part}) versus hard processes (scaling with N_{coll}). Both these are in broad agreement with the results on integrated yields and mid-rapidity $dN_{ch}/d\eta$ measurements, and seem to indicate that the contribution of hard processes to particle production in nuclear collisions increases with collision energy. We have also presented a comparison with the semi-classical QCD approach of Kharzeev and Nardi which employs initial state gluon saturation as the dominant dynamical effect in predicting the energy and centrality evolution of pseudo-rapidity distributions. We find our data to be in surprisingly good agreement with this approach.

In summary, the first two run periods at RHIC with Au+Au beams have yielded a rich set of data that, while not providing a ‘smoking gun’ signature of QGP formation through an explosive growth in charged particle multiplicity, nonetheless exhibit many puzzling and interesting new features that will keep the heavy ion physics community busy in the coming years.

Appendix A

The QCD Phase diagram

A.1 Chiral symmetry

The term ‘chirality’, often a source of much confusion and heartbreak in the mind of a beginning student of particle physics, originated with Lord Kelvin’s seemingly innocuous statement[134]:

“I call any geometrical figure, or group of points, chiral, and say it has chirality, if its image in a plane mirror, ideally realized, cannot be brought to coincide with itself.”

As a statement of geometry, this is illustrated in Fig. A-1 for a two dimensional system. In 2D, a plane mirror is represented as a line. An isosceles triangle (a right angled triangle with unequal sides), after reflection through such a mirror cannot be superimposed on itself by performing *any* 2D transformation like translation or rotation. It is therefore an ‘a-chiral’ object. An equilateral triangle, on the other hand, does not suffer the same fate after reflection and can be easily superimposed on itself: it is a ‘chiral’ object. In the following, we will explain how such a simple property becomes a cornerstone of strong interaction QCD *dynamics*.

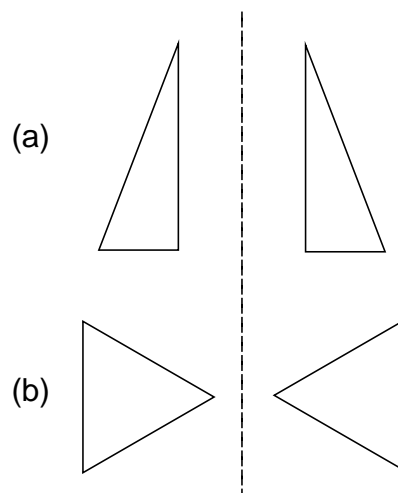


Figure A-1: Examples of (a) a-chirality and (b) chirality in 2D.

In the above example, it is easy to visualise the chirality of triangles. The difficulty in QCD is that we have to visualize the chirality of an *internal* quantum number of a particle: specifically its *isospin*. ‘Isotopic spin’ or isospin for short, is an internal quantum number assigned to each hadron, to signify the fact that the strong interaction does not distinguish, for example, between the proton and neutron which are therefore regarded as isospin partners. The quark constituents of the hadrons are also endowed with isospin values. The assigned values of isospin arise naturally from group theoretical arguments in the quark model, and happen to look very similar to *spin* quantum numbers. This does not mean, however, that the spin and isospin of a quark are in any way related, apart from both being *internal* properties of point particles¹. In fact, we will exploit this fact by using spin and isospin somewhat interchangeably in our discussion, simply because it is easier to visualize the spin of a particle than its isospin. The chirality of both spin and isospin have implications for the V-A theory of weak interactions, which will not be our concern here.

Our approach is as follows:

- Discuss the chirality of spin for quarks, and its relation to the quark’s mass; at the end of the discussion replace ‘spin’ with ‘iso-spin’ in all our pictures.
- Show how a massless quark’s iso-spin interacts with the chirally asymmetric QCD vacuum, and in doing so provides a dynamical mass to the quark.

Our goal is to answer the following questions:

- Why is the proton mass 1 GeV, when the current mass² of the three quarks inside it is only $\sim 5\text{-}7$ MeV?
- Why is the π meson so much lighter than any of the other hadrons?

In trying to answer these questions, we will studiously avoid employing onerous terms like projection operators, group theory and the σ -model. The answer to the second question, in particular, will lead us into discussion of the QCD phase diagram.

¹In the same sense that the number of holes in a donut is an internal, topological property of the donut (it’s genus). Even if the donut were to be shrunk down to a point, it would retain its genus.

²The current mass in the QCD context is strictly zero. A non-zero value is acquired dynamically through interaction with the asymmetric Higgs vacuum, in a manner bearing some similarity to what we will discuss, but that is all we have to say about the current mass.

A.1.1 Spin and its relation to the mass of a particle

Consider a *massless* particle with spin $\frac{1}{2}$. Since the particle is massless, it travels at the speed of light c . The component of the particle's spin (\vec{S}) along its momentum (\vec{k}) defines its *helicity*:

$$h = \frac{\vec{S} \cdot \vec{k}}{|\vec{k}|} \quad (\text{A.1})$$

Since the spin \vec{S} is $\frac{1}{2}$, its component along the direction of motion, and hence the helicity can have two values: $+\frac{1}{2}$ and $-\frac{1}{2}$. Fig. A-2 depicts one way of visualising the helicity. Circular motion in a plane transverse to the particle's velocity can be either clockwise or counter-clockwise, looking in the direction of the velocity, corresponding to the helicity states $+\frac{1}{2}$ and $-\frac{1}{2}$ respectively. It is important to remember that this is purely a graphical picture derived from a traditional visualisation of angular momentum. The spin is usually described as an 'internal angular momentum' of the particle, which also leads to the two helicity states being referred to as right-handed and left-handed respectively.

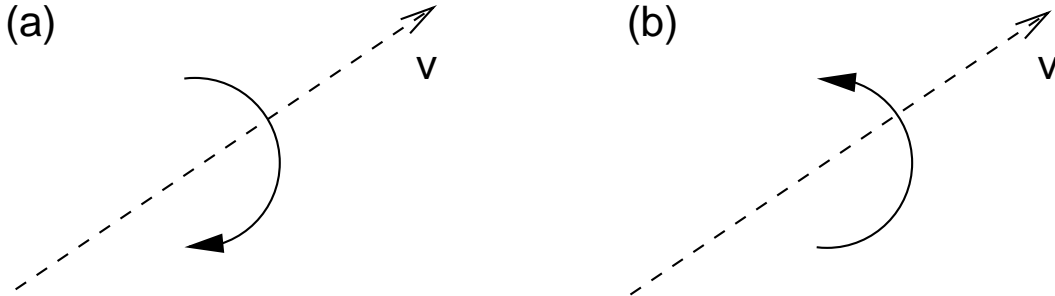


Figure A-2: (a) Helicity = $+\frac{1}{2}$. (b) Helicity = $-\frac{1}{2}$.

Due to the particle being massless, it can only be in one of the two helicity states. The Lagrangian for particles of this type can be written as:

$$\mathcal{L} = \bar{\psi} \not{D} \psi \quad (\text{A.2})$$

where $\psi = \psi_R + \psi_L$ is the particle's wavefunction, and \not{D} is the gauge-covariant derivative. Due to the absence of a mass term, the Lagrangian Eqn. (A.2) can be decomposed into separate right- and left-handed components. The number of right-handed particles N_R , and of left-handed ones N_L are therefore separately conserved ('good') quantum numbers.

If we now endow our hypothetical particle with a mass m , the Lagrangian becomes:

$$\mathcal{L}' = \bar{\psi}(\not{D} - m)\psi \quad (\text{A.3})$$

in which, N_R and N_L are no longer good quantum numbers (although the total number of particles $N_R + N_L$ is still good). We are therefore forced to abandon ψ_R and ψ_L as the basis eigenstates and consider instead the superposition $\psi_R + \psi_L$. Physically, what happens is very clear as expressed in Fig. A-3. Since the particle is now massive, it no longer travels at the speed of light. It is therefore possible to transform to a frame moving faster than the particle's speed. In such a transformed frame, the particle's helicity appears to be opposite from that in a frame at rest. In fact, the particle's mass quantifies how 'easy' it is to flip the measured helicity in this manner. The larger the particle's mass, the slower its velocity. The amount of phase space available to perform such a helicity flipping Lorentz transformation is therefore larger for a more massive particle.

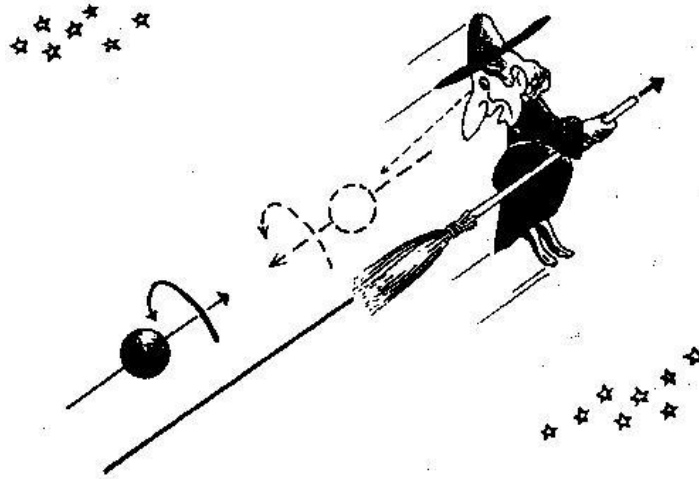


Figure A-3: Helicity flip of a massive particle by Lorentz transformation. Picture is from [11]

The concept of chiral symmetry thus arises naturally from Fig. A-3. The Lagrangian Eqn. (A.2) has a built-in chiral symmetry since it doesn't care about spin helicity states. In the Lagrangian of Eqn. (A.3), however, this chiral symmetry has been explicitly broken by the introduction of a mass term, and particles need to be taken as being in a superposition of left- and right-handed states. The value of the mass term quantifies how badly chiral symmetry is broken.

A.1.2 Quark interactions and isospin

So far, we have been dealing with a hypothetical, massless spin- $\frac{1}{2}$ particle. If we identify this particle as an *a priori* massless quark and replace ‘spin’ with ‘isospin’ in the above discussion,³ we are forced immediately to take into account the quark’s strong interactions in the so-far interaction-less Lagrangian Eqn. (A.2).

The problem is of course that the strong interaction is indeed very strong! The force between a q and \bar{q} is so strong that the ground state of the QCD Lagrangian, usually referred to as the ‘vacuum’ state, is not empty. It is unstable to the spontaneous formation of tightly bound $q\bar{q}$ pairs called the ‘vacuum condensate’. The term condensate is due to the similarity with the phenomenon of Bose–Einstein condensation. In superfluid He, for example, the lowest allowed quantum ground state actually requires pairing of atoms.

Quantitatively, the vacuum condensate has a non-zero expectation value⁴:

$$\langle 0 | \bar{\psi} \psi | 0 \rangle \approx (250 \text{ MeV})^3 \neq 0 \quad (\text{A.4})$$

where $\bar{\psi}$ and ψ are now second-quantized (field-valued) creation and annihilation operators. $\bar{\psi}$ acting on the vacuum creates a quark, and ψ , acting on a 1-quark state, destroys the quark. Both these operators can be decomposed into left- and right-handed components ($\psi_L + \psi_R$) and ($\bar{\psi}_L + \bar{\psi}_R$), and the vacuum condensate can be re-written as:

$$\langle 0 | \bar{\psi}_L \psi_R + \bar{\psi}_R \psi_L | 0 \rangle \neq 0 \quad (\text{A.5})$$

where we have dropped the straight terms ($\bar{\psi}_L \psi_L$ and $\psi_R \bar{\psi}_R$) because they don’t lead to any interesting dynamics. The non-zero expectation value of the condensate indicates that for a left-handed quark going along in vacuum, there is a finite probability of being acted on by ($\bar{\psi}_L \psi_R + \bar{\psi}_R \psi_L$). ψ_L destroys the left-handed quark and $\bar{\psi}_R$ then creates a right-handed one! The quark has thus flipped its helicity purely by interacting with the QCD vacuum.

Connecting this to the idea to the one of helicity-mass relation in the previous section, we arrive at the conclusion that the *a priori* massless quark has acquired a *dynamical* mass through interacting with the vacuum. The rate of such interactions, and hence the value

³The quark’s *spin* plays no role in the chiral dynamics we are about to discuss

⁴The value $(250 \text{ MeV})^3$ is obtained from lattice QCD calculations.

of the quark's acquired mass is governed by the calculable expectation value in Eqn. (A.4). The mass obtained in this manner is called the 'constituent' quark mass. For the u and d quarks, its value is 311–315 MeV/ c^2 which then adds up to the 938 MeV/ c^2 measured mass of the proton, after correcting for the binding energy released in confining three such quarks into the proton.

Due to such 'spontaneous' flipping of quark helicity through interactions with the QCD vacuum condensate, quarks are to be regarded as being in a superposition of two helicity states. Chiral isospin symmetry of the QCD Lagrangian is thus 'spontaneously' broken: in the limit of quark current masses being set to zero, there are no explicit symmetry breaking terms in the QCD Lagrangian (*a lá* Eqn. (A.3)), but the ground state of the theory is chirally asymmetric. Goldstone's theorem guarantees the appearance of a massless boson every time a continuous symmetry is spontaneously broken. For the (u,d) quark generation, the π -meson proves to be the near-massless Goldstone boson⁵. It is very light, with the small mass arising mostly from the current quark masses and loop self-energy contributions.

Having thus understood the dynamical origin of hadron masses, we now need to place it in context with the restoration of chiral symmetry at high temperatures. Lattice QCD calculations indicate (cf. Fig. 1-6, page 21) that the expectation value of the quark condensate $\langle\psi\bar{\psi}\rangle$ vanishes at high temperature. Phenomenologically, this can be understood as follows: at high temperatures, there is a large amount of energy available for pair production in vacuum. Therefore, the number of $q\bar{q}$ pairs condensing out of the vacuum rises rapidly and the color force between individual quarks starts getting screened. In addition the density of colored gluons in such a medium also rises rapidly. The net result of such 'deconfinement' of colored quarks and gluons is that newer $q\bar{q}$ pairs are prevented from condensing in the vacuum. Hence, the expectation value of $\langle\psi\bar{\psi}\rangle$ goes to zero and chiral symmetry is restored.

To clarify things even further, consider the analogy with the tried-and-trusted classical anharmonic oscillator potential[135] shown in Fig. A-4. At zero temperature, the spontaneously broken symmetry of the potential is represented by a non-zero expectation value

⁵We have restricted our discussion to the u and d quarks and the proton,neutron and π mesons, for the sake of simplicity. After including higher quark flavors and their respective constituent masses, one finds similar explanations for masses of the higher baryon resonances, and corresponding meson multiplets with one light meson playing the role of the Goldstone boson. However, due to much higher current quark masses of the heavier quark flavors, explicit chiral symmetry breaking dominates over the spontaneous symmetry breaking discussed above. A similar analysis can also be applied to the vector meson case, and used to explain the lightness of ρ meson compared to the a_1 .

for the order parameter $x \sim \langle \psi \bar{\psi} \rangle$. At high temperatures however, the system has sufficient energy to probe large values of x , and so the small anharmonic term $g^2 x^4$ causing the ground state asymmetry becomes relatively unimportant. g^2 is a direct measure of the asymmetry of the ground state, and in the limit that the $g^2 x^4$ term becomes relatively small, the symmetry of the ground state is restored: $\langle x \rangle \rightarrow 0$.

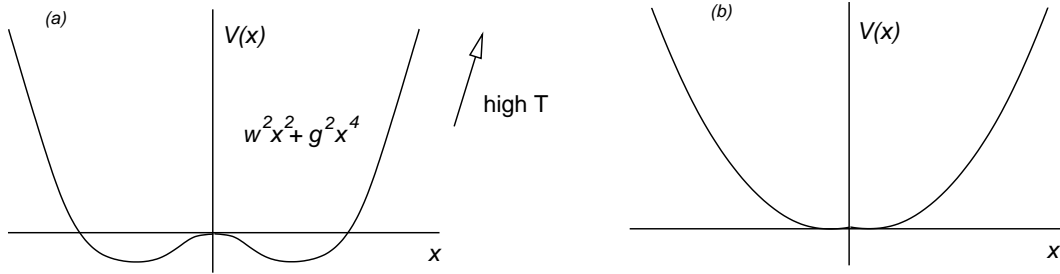


Figure A-4: Classical anharmonic oscillator potential. (a) At zero temperature, ground state is asymmetric due to the anharmonic term $g^2 x^4$. (b) At high temperature, the asymmetry tends to zero, as the system can probe large values of x .

We have thus demonstrated how the process of deconfinement should naturally lead to chiral symmetry restoration. However, it is not clear from detailed QCD arguments[136] whether the reverse requirement is a necessary one. In other words, there is no fundamental argument that these two *a priori* distinct phenomena should occur at the same transition temperature, even though numerical results from lattice QCD indicate that such is the case (cf. Fig. 1-6 on page 21).

A.2 QCD phase diagram

The dynamical processes arising from spontaneously broken chiral symmetry and confinement discussed above lead to the QCD phase diagram illustrated in Fig. A-5. The phase diagram serves as a useful summary of the properties of a many-body system of interacting quarks and gluons. In parallel with condensed matter physics, these properties can be characterised as *thermodynamic* properties, since they describe the collective behavior of a system of *many* particles, responding to external control parameters.

In the QCD case, the relevant control parameters are the temperature T , and the baryochemical potential μ_B . We will describe general arguments arising from QCD theory, experiment and common sense to explain qualitatively some of the features depicted in Fig. A-5.

Quantitative details like the orders of the phase transition and values of control parameters for which they are expected to occur suffer from large uncertainty. Data from experiments involving many-body QCD dynamics, for example, ultra-relativistic heavy ion collisions, would hopefully clarify some of the quantitative details.

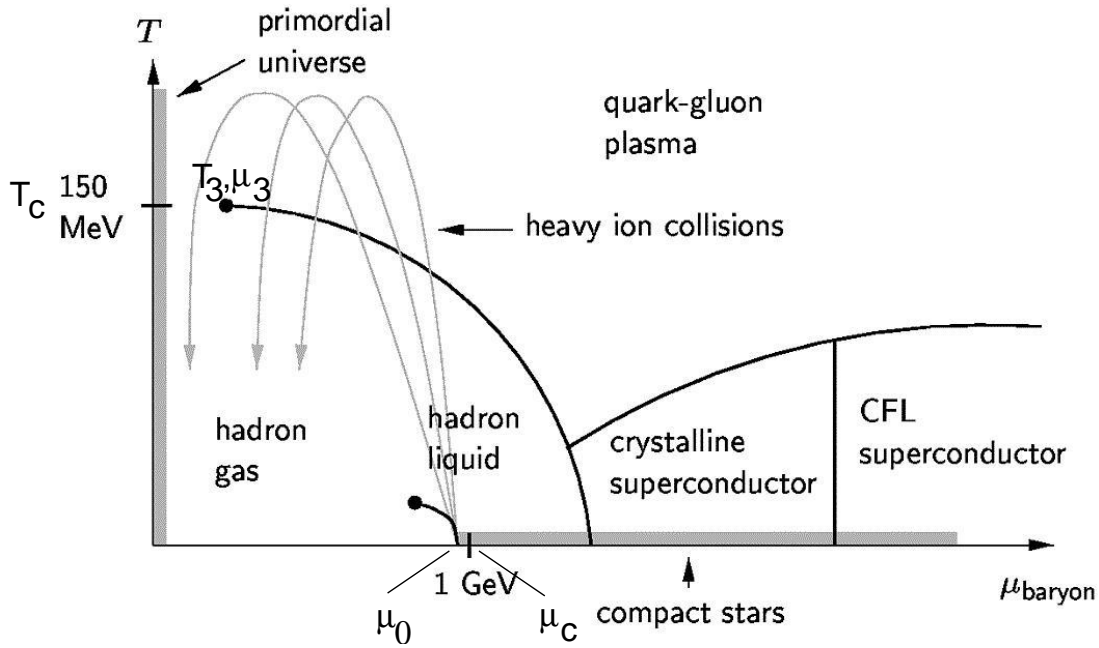


Figure A-5: Proposed QCD phase diagram. See text for discussion

In the bottom left-hand corner of the phase diagram where T and μ_B are both small, the thermodynamic behaviour of QCD can be described in terms of a vapor of hadrons, which are composite states of quarks and/or anti-quarks. In this regime, $T \sim 25 \text{ meV}$ (room temperature) and $\mu_B \ll \mu_N$ where μ_N is the baryo-chemical potential of normal nuclear matter. The principal task in this region is to classify and quantify the bound states; in a sense this traditional domain of particle physics can be caricatured as “relativistic atomic physics”. A crucial property of QCD in this domain is the confinement of color charge (as described in chapter 1). Although the quark constituents of hadrons carry color charge, the observed hadrons are all color-neutral objects. Probing the sub-structure of hadrons with high-energy probes (for example deep inelastic scattering of e^- on p) reveals the strongly interacting partonic constituents, but the many-body phase at these low temperatures and densities is a ‘vapor’ because the force between the color-neutral hadrons is a very weak second-order effect akin to Van der Waal’s forces between neutral atoms.

Two regimes of dynamical interest to us in understanding QCD are:

- $T \rightarrow \infty, \mu_B = 0$ (the y-axis in Fig. A-5), and
- $T = 0, \mu_B \rightarrow \infty$ (the x-axis).

Keeping $\mu_B = 0$, as T increases, lattice QCD calculations indicate that the hadron gas must undergo a phase transition to a deconfined colored ‘soup’ of quarks and gluons at a critical temperature $T_c \sim 150$ MeV ($\sim 10^{12}$ K). This process is akin to the ionization of atoms in a QED plasma at high temperature, hence the name ‘quark gluon plasma’. An important order parameter for this phase transition is the chiral quark condensate $\langle \bar{\psi}\psi \rangle$ discussed in the previous section. The lattice calculations at $\mu_B = 0$ seem to indicate that the phase transition along the y-axis is at least second order, and depending on the number of higher quark flavors included, may even be a smooth crossover. A general argument[137] appealing to the relation of $SU(2)_L \times SU(2)_R$ chiral symmetry to the universality class of $O(4)$ spin models in three dimensions supports this expectation of a second order phase transition. It should be noted that the early universe evolved from a high-temperature, net baryon-free (*i.e.*, $\mu_B = 0$) Big Bang epoch, and in the process of cooling, presumably underwent the reverse phase transition from a primordial quark gluon plasma into a hadron gas. Although this regime is net baryon-free, it is still at high matter density at high temperatures, since the energy densities are sufficient to cause copious production of $q + \bar{q}$ pairs and gluons.

Along the x-axis in Fig. A-5 the dynamics are quite different. A good order parameter in this regime is the net baryon number density $N(\mu_B)$, measured by its conjugate thermodynamical parameter, the net baryo-chemical potential μ_B . Since μ_B is defined as the energy required to add a single baryon, in the vacuum ground state at $T = 0$, for $\mu_B < \mu_0$, the order parameter is identically zero: $N(\mu_B) = 0$. At a critical value of $\mu_0 \sim m_N - 16$ MeV, the baryon number density jumps up abruptly from zero to its value for normal nuclear matter: ~ 0.16 fm⁻³. This is indicated by the first short line rising up from the x-axis in Fig. A-5. For T slightly above zero, continuity ensures that the transition remains of first order, ending in a critical point, as probed in nuclear multi-fragmentation processes[138]. As μ_B is increased further, the utility of $N(\mu_B)$ as an order parameter is lost, as it is only expected to increase monotonically. For example, at the core of compact stars, we expect to find a close to Fermi-degenerate sea of baryons (mostly neutrons produced by electrons

recombining with protons in atoms due to gravitational collapse). We have to revert back to $\langle\bar{\psi}\psi\rangle$ as the signal for chiral symmetry restoration. At $\mu_B \sim \mu_C \gtrsim 1$ GeV corresponding to matter densities ~ 5 – 10 times nuclear matter density, chiral symmetry restoration occurs in the completely Fermi-degenerate sea of quarks. Various theoretical studies[139] seem to indicate that the phase transition in this regime is of first order. For slight temperature perturbations $T > 0$ in this Fermi-degenerate chirally symmetric phase, interesting dynamics like quark-quark pairing on the Fermi-surface is expected[140], leading to remarkable Cooper pair-like color superconductive dynamics. For our purposes, it is sufficient to note that since on the x-axis we have a first order phase transition and along the y-axis, there is a smooth crossover, by continuity it follows that somewhere in the middle at (T_3, μ_3) there must exist a tri-critical point, ending the line of first order transitions. This is indicated in Fig. A-5 and its location is a subject of current theoretical and experimental studies.

Appendix B

Response of silicon detectors and electronics

B.1 Equivalent noise model for single preamplifier channel

Fig. B-1 shows the schematic of a single detector channel, and an electronic equivalent for modelling the noise response from this channel. The symbols used are explained in Table B.1 where typical values for these quantities are also shown. As explained in Chapter 2, the silicon pixel detectors are placed under reverse bias voltage to ensure full depletion across the $300\mu\text{m}$ n-type active area. Since the charge collected by the pixels is capacitively coupled to the readout lines, the noise source in Fig. B-1 can be effectively modelled as a capacitor C in parallel with a current source I_{leak} representing leakage current across the capacitor, and a large resistance R_p due to the polysilicon layer. R_s represents the serial resistance of the readout lines carrying charge to the preamplifier input. C also includes the effects of readout-line-to-adjacent-pad parasitic capacitance. The numbers in Table B.1 are obtained from references [95, 96, 97, 98], [141] or [142]. and verified with test measurements in the laboratory.

The expectation of a signal consisting of 21,700 e^- -hole pairs arises from the fact that a MIP deposits 78 keV of energy per μm of silicon traversed, and the energy cost of creating one such pair is 3.6 eV. In addition to the ‘ideal’ detector noise estimate provided by the model in Fig. B-1, we measure about 460 e^- worth of Equivalent Noise Charge (ENC) from the front-end electronics, contributed by the input buffer and ADC in the FEC’s.

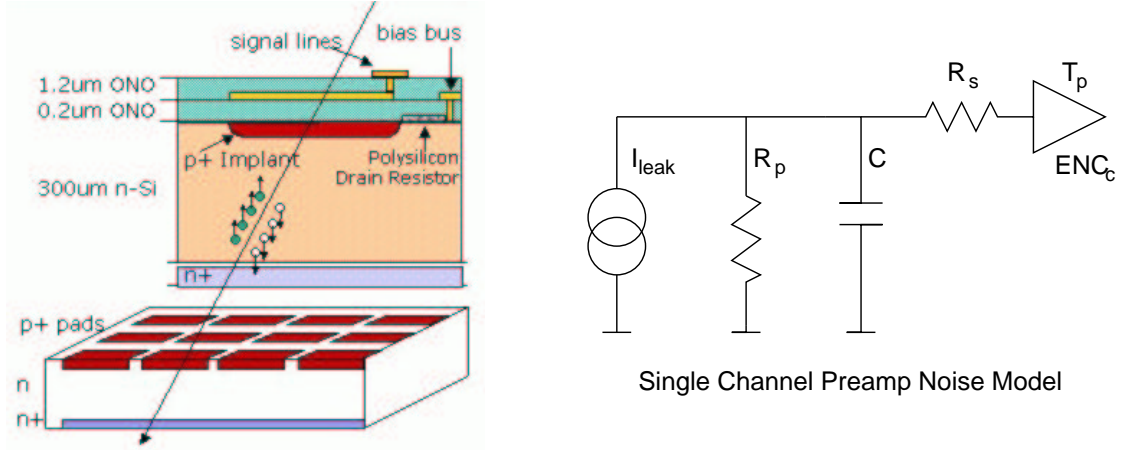


Figure B-1: Schematic of silicon sensor and equivalent noise model.

Quantity(Units)	Value					
Peaking Time T_p (μ s)	1.2					
Bias Resistor R_p ($M\Omega$)	1					
Leakage Current I_{leak} (nA/mm^2)	1.56					
Sensor Type \rightarrow	Type1	Type2	Ring (center)	Ring (edge)	Type5	Octagon
Pads	1540	512	64	64	256	128
Pad area A (mm^2)	1	2.55	25	100	13.3	11
Trace length L_s (cm)	3	3.36	9	4	6.5	11
Pad border B (cm)	0.4	12.85	20	4	2	1.44
Pad capacitance C_p (pF/ mm^2)	0.4	Multiplies A				
Trace capacitance C_t (pF/cm)	4.83	Multiplies L_s				
Interpad capacitance C_i (pF/cm)	1.5	Multiplies B				
Trace resistance (Ω/cm)	100	Multiplies L_s				
Total capacitance C (pF)	15.49	36.52	83.47	65.32	39.72	59.69
Total leakage/pad (nA)	1.56	3.98	39.06	156.25	20.78	17.19
Total R_s (Ω)	300	336	900	400	650	1100
ENC VA preamp constant K	913					
ENC VA preamp slope σ	5					
ENC C (e^-) = $K + C\sigma$	990	1095	1330	1239	1111	1211
ENC R_p (e^-) = $760\sqrt{T_p/R_p}$	830	830	830	830	830	830
ENC I_{leak} (e^-) = $106\sqrt{T_p I_{leak}}$	145	232	726	1451	529	481
ENC R_s (e^-) = $0.4C\sqrt{R_s/T_p}$	97	241	903	471	365	714
ENC total (e^-)	1304	1415	1950	2134	1529	1702
Signal (e^-)	21700					
Signal/Noise	17	5	11	10	14	13

Table B.1: Parameters for the equivalent noise model of a single preamplifier channel.

B.2 Landau distribution of charged particle's energy loss

The probability density $f(\Delta; \beta)$ for the ionization energy loss Δ of a charged particle when traversing a thick layer of matter was first derived by Landau [111], and is given by

$$f(\Delta; \beta) = \frac{1}{\xi} \phi(\lambda) \quad (\text{B.1})$$

where ξ is a parameter related to the properties of the material and the particle's velocity $\beta = v/c$, and $\phi(\lambda)$ is the probability density of the dimensionless variable λ . λ is related to the properties of the material, the velocity β , and most importantly, the energy loss Δ . The dependence is as follows:

$$\lambda = \frac{1}{\xi} [\Delta - \xi (\ln \frac{\xi}{\epsilon'} + 1 - \gamma_E)] \quad (\text{B.2})$$

$$\epsilon' = \frac{I^2 \exp(\beta^2)}{2m_e c^2 \beta^2 \gamma^2} \quad (\text{B.3})$$

$$\xi = \frac{2\pi N_A e^4 \rho Z}{m_e c^2 A} \frac{d}{\beta^2} \quad (\text{B.4})$$

where N_A is Avagadro's number, m_e and e are the mass and charge of the electron, Z and A are the sums of the atomic numbers and atomic weights of the molecular substance, ρ is its density, d is the thickness of the layer, $I = I_0 Z$ with $I_0 \approx 13.5$ eV is ionization energy characteristic of the material, and $\gamma_E = 0.5772\dots$ is Euler's constant.

For our analysis, the function $\phi(\lambda) \sim \phi(\Delta)$ is of primary interest:

$$\phi(\lambda) = \frac{1}{2\pi i} \int_{\epsilon - i\infty}^{\epsilon + i\infty} \exp(u \ln u + \lambda u) du \quad (\text{B.5})$$

where ϵ is an infinitesimal positive number. After a trivial transformation, we have:

$$\phi(\lambda) = \frac{1}{\pi} \int_0^\infty \exp(-u \ln u - \lambda u) \sin(\pi u) du \quad (\text{B.6})$$

From Eqn. (B.6) it is immediately obvious that the mean and all higher moments of the Landau distribution don't exist! The integral $\int_0^\infty \Delta^n \phi(\Delta) d\Delta$ diverges for $n \geq 1$. This is shown in Fig. B-2a where the energy loss distribution is plotted for several values of the velocity $\beta = v/c$. The distribution has long tails, indicating the divergent mean.

In most simple analyses, the distribution is truncated and the so-called truncated mean is used to characterize particle's velocity β [143]. However, as seen in Fig. B-2a, a much better measure of the particle's velocity is the most-probable value of energy loss Δ_{mp} , the maximum of the probability distribution function. As the particle's velocity increases, Δ_{mp} first falls rapidly, reaches a minimum (corresponding to the minimum ionizing particle or MIP) and then undergoes a slow relativistic rise for velocities close to c . This behaviour of Δ_{mp} is shown in Fig. B-2b and follows the typical "Bethe-Bloch" parametrization curve used as a basis for identifying charged particles via measurement of their ionization energy loss. The value of Δ_{mp} can be computed numerically from Eqn. (B.6), and is found to be[144]:

$$\Delta_{mp} = \xi \left[\ln \frac{\xi}{e'} + 0.198 \right] \quad (\text{B.7})$$

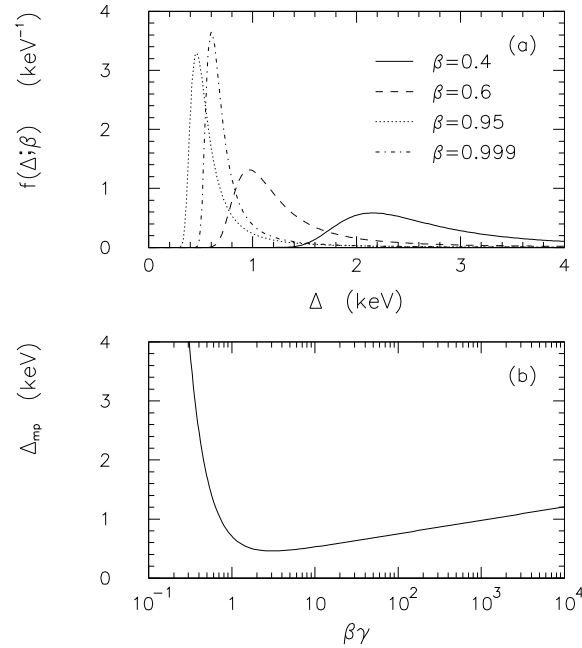


Figure B-2: (a) Landau probability density for energy loss Δ of charged particle traversing 4mm of argon gas for various values of velocity β . Note that for thin absorbers like 300 μm of silicon, the Landau-Vavilov distribution with Shulek corrections as discussed in chapter 3 is more appropriate. (b) The peak position Δ_{mp} of the above distribution as a function of $\beta\gamma$.

B.3 Convolution of multiple Landau distributions

The distribution of ionization energy loss measured in a single pad of a typical silicon sensor in the detector near $\eta = 0$ is shown in Fig. B-3. The first prominent peak corresponding MIP energy deposition is obviously seen at Δ_{mp} . In addition, second and third peaks located at approximately $2\Delta_{mp}$ and $3\Delta_{mp}$ are also observed; the latter correspond to two and three minimum ionizing particles traversing the same pad in an event. The observation of these two additional peaks at roughly proportionate locations hints at a numerical relationship derivable from the convolution of multiple Landau probability distribution functions. Indeed, a calculation due to [145], reproduced below, shows this to be the case.

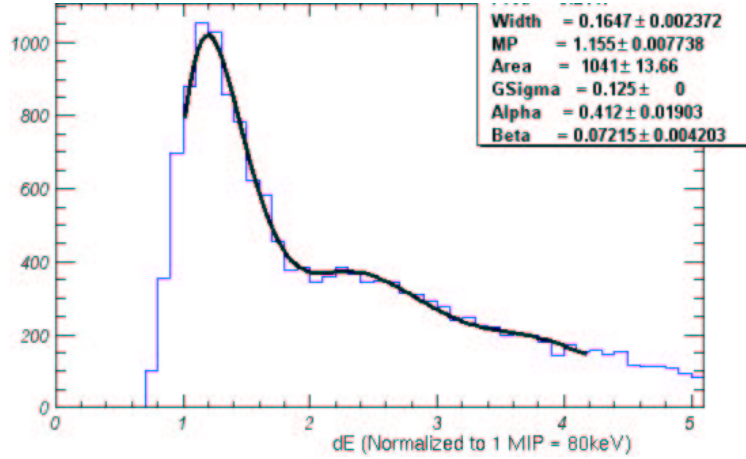


Figure B-3: Distribution of energy signals measured in pads near $\eta = 0$ for central events

Consider a process in which N charged particles deposit energies Δ_i through ionization in materials characterised by parameters ξ_i , and have most probable energy losses given by Δ_{mp}^i . The product of N such Landau probability distribution functions is:

$$\frac{d^N P}{d\Delta_1 \cdots d\Delta_N} = \prod_{i=1}^N f(\Delta_i; \Delta_{mp}^i, \xi_i) \quad (\text{B.8})$$

where the individual p.d.f.'s are of the Landau form:

$$f(\Delta_i; \Delta_{mp}^i, \xi_i) = \frac{1}{\xi_i} \phi\left(\frac{\Delta_i - \Delta_{mp}^i}{\xi_i}\right) \quad (\text{B.9})$$

where the function ϕ as written before is:

$$\phi(\lambda) = \frac{1}{2\pi i} \int_{-i\infty}^{+i\infty} \exp(u \ln u + \lambda u) du \quad (\text{B.10})$$

In expanded form, we therefore have:

$$\begin{aligned} \frac{d^N P}{d\Delta_1 \cdots d\Delta_N} &= \frac{1}{(2\pi i)^N} \frac{1}{\prod_{i=1}^N \xi_i} \int_{-i\infty}^{+i\infty} \cdots \int_{-i\infty}^{+i\infty} \\ &\quad \exp \left[\sum_{i=1}^N u_i \ln u_i + \left(\frac{\Delta_i - \Delta_{mp}^i}{\xi_i} \right) u_i \right] du_1 \cdots du_N \end{aligned}$$

Now we perform the transformation of variables $(\Delta_1, \Delta_2, \dots, \Delta_N) \rightarrow (\Delta, \Delta'_2, \dots, \Delta'_N)$ as follows:

$$\Delta = \sum_{i=1}^N \Delta_i; \Delta'_2 = \Delta_2; \Delta'_3 = \Delta_3 \cdots \quad (\text{B.11})$$

which implies the reverse transformation:

$$\Delta_1 = \Delta - \sum_{i=2}^N \Delta'_i; \Delta_2 = \Delta'_2; \Delta_3 = \Delta'_3 \cdots \quad (\text{B.12})$$

It is trivial to check that the Jacobian of this transformation is 1. Substituting for $(\Delta_1, \Delta_2, \dots, \Delta_N)$ in Eqn. (B.11) and integrating over $d\Delta'_2, d\Delta'_3, \dots, d\Delta'_N$ we get:

$$\begin{aligned} \frac{dP}{d\Delta} &= \frac{1}{(2\pi i)^N} \frac{1}{\prod_{i=1}^N \xi_i} \left(\int_{-\infty}^{+\infty} \right)^{N-1} \left(\int_{-i\infty}^{+i\infty} \right)^N \\ &\quad \exp \left[u_1 \ln u_1 + \left(\frac{\Delta - \sum_{i=2}^N \Delta'_i - \Delta_{mp}^1}{\xi_1} \right) u_1 + \sum_{i=2}^N u_i \ln u_i + \left(\frac{\Delta'_i - \Delta_{mp}^i}{\xi_i} \right) u_i \right] \\ &\quad du_1 \cdots du_N d\Delta'_2 \cdots d\Delta'_N \end{aligned}$$

Bringing the $d\Delta'_2, d\Delta'_3, \dots, d\Delta'_N$ forward, and rearranging terms, we obtain:

$$\begin{aligned} \frac{dP}{d\Delta} &= \frac{1}{(2\pi i)} \frac{1}{\prod_{i=1}^N \xi_i} \left(\int_{-i\infty}^{+i\infty} \right)^N \exp \left[\frac{\Delta}{\xi_1} u_1 + \sum_{i=1}^N \left(u_i \ln u_i - \frac{\Delta_{mp}^i}{\xi_i} u_i \right) \right] \\ &\quad \left[\prod_{i=2}^N \frac{1}{(2\pi i)} \int_{-\infty}^{+\infty} \exp \left(\left(\frac{u_i}{\xi_i} - \frac{u_1}{\xi_1} \right) \Delta'_i \right) d\Delta'_i \right] du_1 \cdots du_N \end{aligned}$$

Now, using the fact that $\frac{1}{2\pi i} \int_{-\infty}^{+\infty} e^{ikx} dx = \delta(k)$, we obtain for each of the $(N-1)$ Δ'_i integrals above:

$$\xi_i \delta\left(u_i - \frac{\xi_i}{\xi_1} u_1\right) \quad (\text{B.13})$$

which simplifies to:

$$\begin{aligned} \frac{dP}{d\Delta} &= \frac{1}{(2\pi i)} \frac{1}{\xi_1} \left(\int_{-i\infty}^{+i\infty} \right)^N \exp \left[\frac{\Delta}{\xi_1} u_1 + \sum_{i=1}^N \left(u_i \ln u_i - \frac{\Delta_{mp}^i}{\xi_i} u_i \right) \right] \\ &\quad \prod_{i=2}^N \delta\left(u_i - \frac{\xi_i}{\xi_1} u_1\right) du_1 \cdots du_N \\ &= \frac{1}{(2\pi i)} \frac{1}{\xi_1} \int_{-i\infty}^{+i\infty} \exp \left[\frac{\Delta}{\xi_1} u_1 + \sum_{i=2}^N \frac{\xi_i}{\xi_1} u_1 \ln \left(\frac{\xi_i}{\xi_1} u_1 \right) - \frac{\Delta_{mp}^i}{\xi_i} u_i + u_1 \ln u_1 - \frac{\Delta_{mp}^1}{\xi_1} u_1 \right] du_1 \\ &= \frac{1}{(2\pi i)} \frac{1}{\xi_1} \int_{-i\infty}^{+i\infty} \exp \left[\frac{\sum_{i=1}^N \xi_i}{\xi_1} u_1 \ln u_1 + \sum_{i=2}^N \frac{\xi_i}{\xi_1} u_1 \ln \left(\frac{\xi_i}{\xi_1} u_1 \right) \right. \\ &\quad \left. + \left(\frac{\Delta - \sum_{i=1}^N \Delta_{mp}^i}{\xi_1} \right) u_1 \right] du_1 \end{aligned}$$

Let $u = \frac{\sum_{i=1}^N \xi_i}{\xi_1} u_1$, then:

$$\begin{aligned} \frac{dP}{d\Delta} &= \frac{1}{(2\pi i)} \frac{1}{\xi_1} \int_{-i\infty}^{+i\infty} \exp \left[u \ln \frac{\xi_1}{\sum_{i=1}^N \xi_i} u + \left(\sum_{i=2}^N \frac{\xi_i}{\xi_1} \ln \left(\frac{\xi_i}{\xi_1} \right) \right) \frac{\xi_1}{\sum_{i=1}^N \xi_i} u \right. \\ &\quad \left. + \left(\frac{\Delta - \sum_{i=1}^N \Delta_{mp}^i}{\xi_1} \right) \frac{\xi_1}{\sum_{i=1}^N \xi_i} u \right] \frac{\xi_1}{\sum_{i=1}^N \xi_i} du \\ &= \frac{1}{(2\pi i)} \frac{1}{\sum_{i=1}^N \xi_i} \int_{-i\infty}^{+i\infty} \exp \left[u \ln u + u \ln \left(\frac{\xi_1}{\sum_{i=1}^N \xi_i} \right) + \frac{\xi_1}{\sum_{i=1}^N \xi_i} \left(\sum_{i=2}^N \frac{\xi_i}{\xi_1} \ln \left(\frac{\xi_i}{\xi_1} \right) \right) u \right. \\ &\quad \left. + \left(\frac{\Delta - \sum_{i=1}^N \Delta_{mp}^i}{\sum_{i=1}^N \xi_i} \right) u \right] du \\ &= \frac{1}{(2\pi i)} \frac{1}{\sum_{i=1}^N \xi_i} \int_{-i\infty}^{+i\infty} \exp \left[u \ln u + \right. \\ &\quad \left. \left(\frac{\Delta - (\sum_{i=1}^N \Delta_{mp}^i + (\sum_{i=1}^N \xi_i) \ln \left(\frac{\xi_1}{\sum_{i=1}^N \xi_i} \right) + \sum_{i=2}^N \xi_i \ln \frac{\xi_i}{\xi_1})}{\sum_{i=1}^N \xi_i} \right) u \right] du \\ &= \frac{1}{(2\pi i)} \frac{1}{\sum_{i=1}^N \xi_i} \int_{-i\infty}^{+i\infty} \exp \left[u \ln u + \left(\frac{\Delta - (\sum_{i=1}^N \Delta_{mp}^i + \sum_{i=1}^N \xi_i \ln \frac{\sum_{j=1}^N \xi_j}{\xi_i})}{\sum_{i=1}^N \xi_i} \right) u \right] du \end{aligned}$$

We have thus obtained a form similar to the original Landau p.d.f Eqn. (B.9) and Eqn. (B.10) with the dimensionless parameter λ :

$$\lambda = \frac{\Delta - \Delta_{mp}^{eff}}{\xi^{eff}} \quad (\text{B.14})$$

where the effective most-probable value Δ_{mp}^{eff} , and effective ξ^{eff} are:

$$\begin{aligned} \Delta_{mp}^{eff} &= \sum_{i=1}^N \left[\Delta_{mp}^i + \xi_i \ln \frac{\sum_{j=1}^N \xi_j}{\xi_i} \right] \\ \xi^{eff} &= \sum_{i=1}^N \xi_i \end{aligned}$$

For the common case when all the charged particles are in the relativistic rise regime $\Delta_{mp}^i = \Delta_{mp}$ and a single material is used $\xi_i = \xi$, the above formulae reduce to:

$$\Delta_{mp}^{eff} = N\Delta_{mp} + \xi N \ln N \quad (\text{B.15})$$

$$\xi^{eff} = N\xi \quad (\text{B.16})$$

Thus we have arrived at the simple result that the N^{th} MIP peak in a convolution of multiple Landau distributions is positioned at N times the first MIP peak, plus a small correction as indicated in Fig. B-2.

Appendix C

Comparison of different MC simulations

In this appendix, we will aim to answer the following question: What is the affect of high occupancy on the occupancy and background correction terms. For the occupancy correction terms: does the method of determining occupancy corrections work at higher occupancies in central collisions at $\sqrt{s_{NN}} = 200$ GeV and $\sqrt{s_{NN}} = 130$ GeV? Since the background correction term is completely derived from MC simulations, how sensitive is it to the details of the simulation, and in particular, to the event generator input?

In order to answer the above questions, the analysis chain was run separately on large statistics Monte Carlo simulation runs using HIJING, RQMD and VENUS event generators. A first pass through the ‘data’ generated by the simulations (including smearing of signals to simulate detector noise and gains), yielded the occupancy correction term. The second pass applied the occupancy correction term and extracted $dN_{ch}/d\eta$, uncorrected for backgrounds. By comparing the reconstructed $dN_{ch}/d\eta$ to the event generator input, the background correction was obtained.

Simulated signals from the paddle detectors were *not* used as measure of the centrality for this study, since our aim is to study the response of the silicon detector in extreme conditions of occupancy, and it is pointless to add further complexity by convoluting in the simulated response of another detector type. The occupancy of the detector itself, measured in terms of the total number of merged hits found in Octagon and Ring detectors was used to categorize events into different classes. Fig. C-1 demonstrates the binning used

for $\sqrt{s_{NN}} = 130$ GeV collisions. The distribution of the number of found hits in Oct+Rings is shown in Fig. C-1a. VENUS seems to provide the largest number of raw hits ≈ 4800 . A scale of 0-5400 hits with 18 bins was then used to tag each event, and the distribution of events in the various bins is shown in Fig. C-1b. In this way ‘Occupancy bin 9’ corresponds to roughly the same occupancy of the detector in all three simulations– it also corresponds roughly to the maximum occupancy seen in the detector for central $\sqrt{s_{NN}} = 130$ GeV collisions.

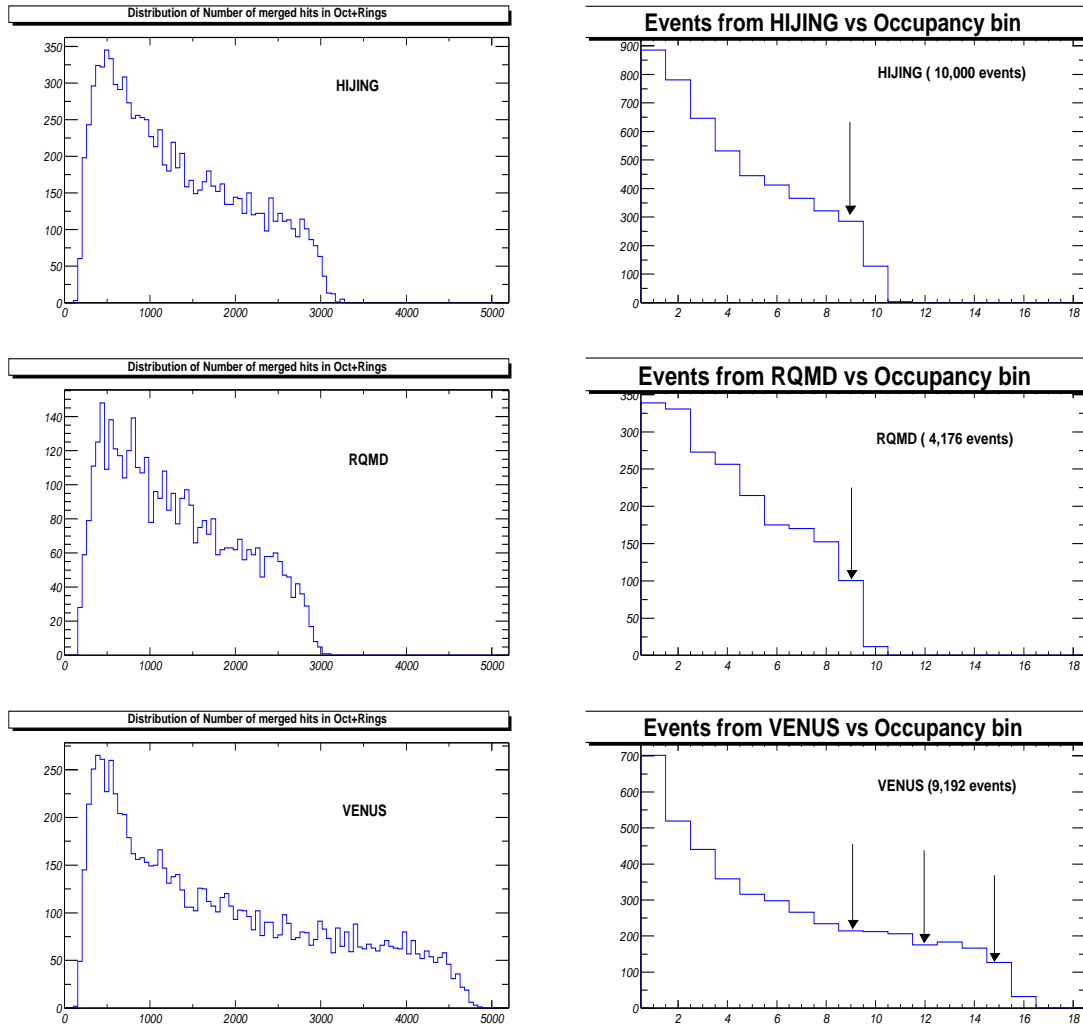


Figure C-1: (Left) Distribution of merged hits in HIJING, RQMD and VENUS simulations for $\sqrt{s_{NN}} = 130$ GeV Au+Au collisions. (Right) 18 ‘Occupancy Bins’ are defined between 0-5400 hits. The arrows indicate the bins whose results are shown in the following figures. Bin 9 corresponds to the highest occupancy bin in HIJING and RQMD, and also measured in the data at $\sqrt{s_{NN}} = 130$ GeV.

The results of reconstructed $dN_{ch}/d\eta$ for HIJING, RQMD and VENUS are shown compared to the ‘truth’ input information in Fig. C-2a at $\sqrt{s_{NN}} = 130$ GeV and in Fig. C-2b at $\sqrt{s_{NN}} = 200$ GeV. For clarity, only the top occupancy bin is shown for HIJING and RQMD and the top 3 occupancy bins are shown for VENUS. From these two sets of figures it is clear that at the highest occupancy levels seen in the data (corresponding to about bin 9 of both HIJING and RQMD), and at even higher occupancy levels seen in VENUS simulations, the reconstruction procedure seems to provide a sensible output, without any signs of saturation.

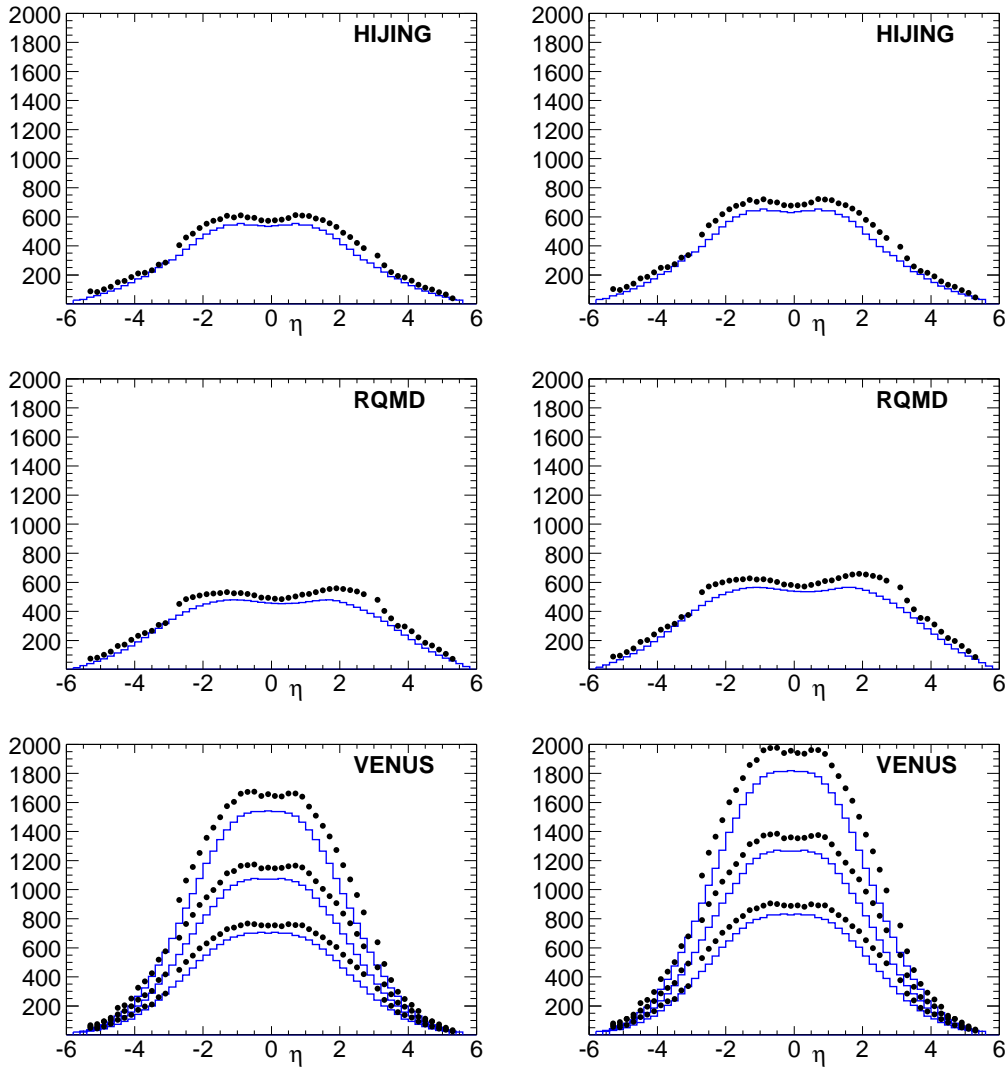


Figure C-2: HIJING (Top) RQMD (middle) and VENUS (Bottom): Pseudorapidity distributions of charged particles reconstructed (circles) and input as truth (lines) in the simulations at $\sqrt{s_{NN}} = 130$ GeV (left) and $\sqrt{s_{NN}} = 200$ GeV (right)

A crucial test of the consistency of background corrections computed in this manner is the fact that while they vary substantially as a function of η , they remain nearly unchanged for the different MC simulations at the same occupancy bin. Fig. C-3 shows the ratios of primary particle input to the reconstructed output from HIJING (a), RQMD (b) and VENUS (c) simulations. By definition, the background correction accounts for secondaries produced away from the primary vertex as the primary particles stream through the beam pipe and other intervening material on their way to the detector. Hence, the reconstructed output must be proportional to the primary particle input, with the constant of proportionality being the background correction we compute. In particular, as the primary particle input is varied (p_T spectrum, η distribution) across different MC simulations, the output should change *linearly* with the proportionality factor, *i.e.*, the background correction, remaining unchanged. This is indeed borne out by Fig. C-3.

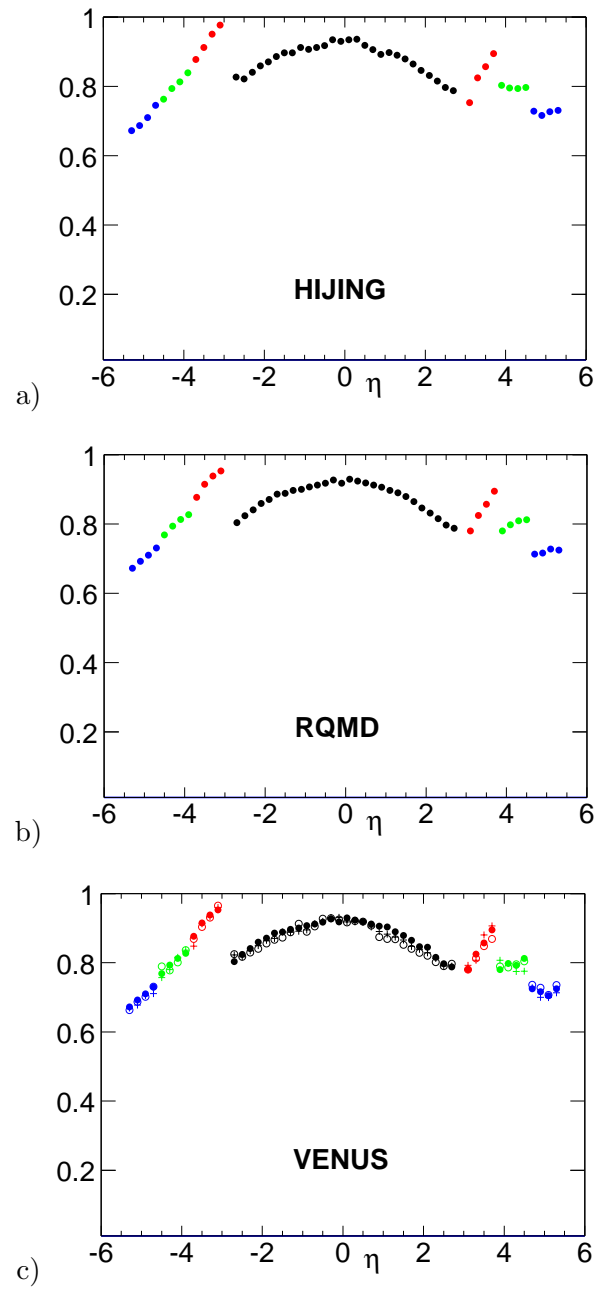


Figure C-3: (a) HIJING, (b) RQMD and (c) VENUS: Background corrections derived as a ratio of Truth to reconstructed $dN_{ch}/d\eta$.

Bibliography

- [1] J. C. Maxwell. *A Treatise on Electricity and Magnetism, Vol 1 and 2*. Dover Student Editions, 1967 (originally published 1873). ISBN 0486606368. In order to interpret the symbols and language used, it should probably be read with a modern accompaniment like *Maxwell on the Electromagnetic Field: A Guided Study (Masterworks of Discovery)* by T. K. Simpson and A. Farrell (1997) ISBN 081352363X. 1
- [2] K. Hagiwara *et al* (Particle Data Group). *Phys. Rev.*, C66:10001, 2002. See also Mohr *et al*, *Rev. Mod. Phys.* 72, 351. 1, C
- [3] K. Hagiwara *et al* (Particle Data Group). *Phys. Rev. D*, 66:10001, 2002. See also Mohr *et al*, *Rev. Mod. Phys.* 72, 351. 1
- [4] R. Hofstadter. In *Nobel Lectures*. 1961. 1
- [5] M. Gell-Mann. *Phys. Lett.*, 8:214, 1964. 1
- [6] G. Zwiig. Technical report, CERN, 1964. CERN-TH 401 and CERN-TH 412. 1
- [7] V. E. Barnes *et al*. *Phys. Lett.*, 12:134, 1964. 1
- [8] H. L. Anderson. *Journal de Physique*, Tome 43, Supp. 12:8–101, Dec. 1982. This is an excellent review of the early discoveries of particle resonances. See also <http://www.osti.gov/accomplishments/pdf/DE84017107/DE84017107.pdf> for a historical account. 1
- [9] Y. Nambu. *Phys. Rev.*, 139B:1006, 1965. 1
- [10] O. W. Greenberg. *Phys. Rev. Lett.*, 13:598, 1964. 1
- [11] Y. Nambu. *Quarks*. *Frontiers in Physics*, 1967. ISBN 9971966654. 1, A-3

- [12] H. W. Kendall, J. Friedman, and F. Taylor. In *Nobel Lectures*. 1972. 1
- [13] M. Fritzsch, M. Gell-Mann, and H. Leutwyler. *Phys. Lett. B*, 47:365, 1971. 1
- [14] S. Weinberg. *Phys. Rev. Lett.*, 31:494, 1973. See also *Rev. Mod. Phys.* 46, 255 (1974).
1
- [15] C. N. Yang and R. L. Mills. *Phys. Rev.*, 96:191–195, 1954. 1
- [16] D. Gross and F. Wilczek. *Phys. Rev. Lett.*, 30:1343, 1973. 1
- [17] H. Politzer. *Phys. Rev. Lett.*, 30:1346, 1973. 1
- [18] S. Wienberg. *Phys. Rev. Lett.*, 40:223, 1978. 1
- [19] F. Wilczek. *Phys. Rev. Lett.*, 40:279, 1978. 1
- [20] L. Rosenberg and K. A. van Bibber. *Phys. Rep.*, 325:1, 2000. 1
- [21] D. Gross and F. Wilczek. *Phys. Rev. D*, 8:3633, 1973. 1
- [22] S. Bethke. In *QCD 02 High Energy Physics International Conference in QCD*, Montpellier, France, July 2-9,2002. Available as hep-ex/0211012. See also, S. Bethke *J. Phys. G*26, R27(2000) and M. Schmelling, hep-ex/9701002. 1-2, 7, C
- [23] J. Zinn-Justin. *Phys. Rep.*, 70:109, 1981. Pedagogical review of Borel resummability of field theories, concentrating on scalar field theories. See also references therein. 1
- [24] G. West. *Found. Phys.*, 30:695–704, 2000. A recent review on the convergence of QCD perturbative expansions. 1
- [25] J. Schwinger. *Phys. Rev.*, 128:2425, 1962. 1
- [26] J. D. Bjorken. In *Recent Advances in High Energy Physics*, Barbizon Hotel, New York, 1973. New York Academy of Science. 1
- [27] A. Casher, J. Kogut, and L. Susskind. *Phys. Rev. D*, 10:732, 1974. 1
- [28] J. W. Rohlf. *Modern Physics from a to Z0*. Wiley, 1994. Chapter 15, ISBN 0471572705.

- [29] G. 't Hooft. *Nucl. Phys. B*, 72:461, 1974. t'Hooft's conjecture that for large N , $SU(N)$ theories of QCD are equivalent to string theories with string tension $\sim k/N$, since only planar Feynman diagrams contribute. 3
- [30] J. M. Maldacena. *Adv.Theor.Math.Phys.*, 2:231–252, 1998. 3
- [31] Yu. L. Dokshitzer and S. I. Troyan. *Proceedings of 19th Leningrad Winter School*, 1:144–188, 1984. For development of Modified Leading Log Approximation (MLLA), and Local Parton-Hadron Duality (LPHD). See also Mueller, A.H Nucl. Phys. B213 85, B241 141 (1983) and Dokshitzer *et al* Z. Phys. C27 65 (1985). For a recent review of jet fragmentation physics and phenomenolgy, see hep-ph/0109282, a condensed version of which appears in the annual Particle Data Book. 3
- [32] L. McLerran and R. Venugopal. *Phys. Rev. D*, 59:094002, 1999. An effective field theory approach to computing structure functions at small x . Also available as hep-ph/9809427. 3
- [33] K. Hagiwara *et al* (Particle Data Group). *Phys. Rev. D*, 66:10001, 2002. 1.1
- [34] W. M. Fairbank *et al*. *American Journal of Physics*, 50(5):394–397, 1982. Review article on experiments carried out in 1960's and 1970's. 1.1
- [35] D. Morpurgo *et al*. *Phys. Lett.*, 23:609, 1966. 1.1
- [36] P. F. Smith. *Ann. Rev. Nucl. and Part. Sci.*, 39:73, 1989. 1.1
- [37] J. C. Collins and M. J. Perry. *Phys. Rev. Lett.*, 34:1353, 1975. First mention of 'superdense' matter: motivation from Astrophysics. 1.1
- [38] E. Teller *et al*. *Phys. Rev. D.*, 8:4302, 1974. First mention of 'highly excited nuclear matter': motivation from medium energy nuclear physics. 1.1, 4
- [39] E. Shuryak. *Phys. Rep.*, 61:71, 1980. This is a mammoth review of the state of the art in our understanding of the dense phase of QCD at the end of the 'initial' development period of QCD. In some sense, these ideas are still the state of the art, *i.e.*, we know little more now than what we knew then! The term 'Quark Gluon Plasma' was coined in this paper. 1.1
- [40] B. Carter and H. Quintana. *Astrophys. Lett.*, 14:105, 1973. 1.1

- [41] Ya. B. Zel'dovich and I. D. Novikov. *Relativistic Astrophysics, Vol. 1: Stars and Relativity*. Univ. of Chicago Press, Chicago, Ill., 1971. 1.1
- [42] A. M. Polyakov. *Phys. Lett. B*, 72:477, 1978. 1.1
- [43] K. G. Wilson. *Phys. Rev. D*, 10:2445, 1974. 4
- [44] F. Karsch. In *40th Internationale Universitatswochen fuer Theoretische Physik: Ddense Matter (IUKT 40)*, Schladming, Styria, Austria, March 3-10,2001. Available as hep-lat/0106019. 4, 1-5, 1-6, C
- [45] K. Kajantie *et al.* *Phys. Rev. Lett.*, 79:3130, 1997. 4
- [46] P. Decowski. *Energy and centrality dependence of mid-rapidity charged particle multiplicity in relativistic heavy-ion collisions*. PhD thesis, Massachusetts Institute of Technology, 2001. 6, 13, 4.3, 6.1.2
- [47] Except for correlated production of particles of a specific charge from an isolated 'domain', for example pion production from a chiral domain. For further discussion see [65] and references therein. 7
- [48] M. M. Aggarwal *et al* (WA98). *Phys. Lett.*, B420:169–179, 1998. 7
- [49] K. Hagiwara *et al* (Particle Data Group). *Phys. Rev.*, D66:010001–2 and 010001–5, 2002. 1-7, 6-9, C
- [50] X.-N. Wang and M. Gulassy. *Phys. Rev.*, D45:844, 1992. 1-7, C
- [51] R. P. Feynman. *Photon-Hadron Interactions*. W. A. Benjamin, Reading, MA, 1972. ASIN 0805325107. Newer Edition with ISBN 0201360748 is also available. 7
- [52] M. Botje. *Nucl. Phys. Proc. Suppl.*, 79:111–114, 1999. Presented at DIS99, Zeuthen, Germany, April 19-23, 1999. Available as hep-ph/9905518. See also Eur.Phys.J. C12 (2000) 243-262 (hep-ph/9907512). 7
- [53] W. Busza and R. Ledoux. *Ann. Rev. of Nucl. and Part. Sci.*, 38:119–159, 1988. 1-8, 1-9, C
- [54] V. Koch. In *Quark Matter*, Nantes, France, 2002. Very interesting talk, available as a preprint nucl-th/0210070. 7

- [55] I. Otterlund. *Acta. Phys. Pol.*, B8:119, 1977. See also W. Busza, 333 (1977) *ibid.* 7
- [56] C. DeMarzo *et al* (NA5). *Phys. Rev.*, D26:1019–1035, 1982. See also *Phys. Rev. D* 29:2476(1984) by the same authors. 1-9, C
- [57] J. Benecke, T. T. Chou, C-N. Yang, and E. Yen. *Phys. Rev.*, 188:2159, 1969. 7, 6.1.2
- [58] A. Bialas, M. Bleszyński, and W. Csyż. *Nucl. Phys.*, B111:461, 1976. See also A. Bialas *et al*, *Acta Physica Polonica* B18:591. 7
- [59] W. Busza and M. Goldhaber. *Phys. Lett. B*, 139:235, 1984. 7, 15
- [60] A. Sandoval *et al.* *Phys. Rev. Lett.*, 45:874, 1980. See also, *Phys. Rev. Lett.* 58(1987) 463 and for a recent review, see M. Gazdzicki and D. Rohrlich, *Z. Phys. C* 65(1995)pp215-223. 1-11
- [61] J. Klay. *Transverse Mass and rapidity spectra of protons and pions from Au+Au collisions at the AGS.* PhD thesis, University of California, Davis CA, 2001. 1-11, 6-7, 6-9
- [62] P. Seyboth. In *ICPAQGP*, Jaipur, India, 2001. Available as hep-ex/0206046. See also contribution by P. Seyboth to proceedings of 17th Winter Workshop on Nuclear Dynamics, Park City, Utah, March 2001, available at <http://theo08.nsl.msu.edu/winterworkshop/proceedings/toc.htm>. In addition, see [126]. 1-11, 6-7, 6-9
- [63] R. J. Glauber. In *Lectures in Theoretical Physics, Vol I, Lectures delivered at the Summer Institute for Theoretical Physics, University of Colorado, Boulder*, pages 315–414, 1958. 7
- [64] W. Busza. Private communication. “The loss of color degrees of freedom when deconfined QGP goes back to confined hadrons will cause entropy to decrease (second law violation) *unless* the hadronization is accompanied by expansion”. 7
- [65] P. Steinberg. *Search for disoriented chiral condensates in 158 AGeV Pb+Pb Collisions.* PhD thesis, Massachusetts Institute of Technology, 1997. 7, 47
- [66] J. Kapusta. *Phys. Rev. C.*, 27:2037, 1983. 7

- [67] PHOBOS collaboration. *Phys. Rev. Lett.*, 89:222301, 2002. 7
- [68] C. Y. Wong. *Introduction to High-Energy Heavy-Ion Collisions*. World Scientific, 1994. ISBN 9810202636. 7
- [69] L. P. Csernai and D. D. Strottman. *Relativistic Heavy Ion Physics, Vol 5 and 6 of the International Review of Nuclear Physics*. World Scientific, 1991. ISBN 9810205503. For a recent review, see also N. Armesto and C. Pajares, *Int.J.Mod.Phys. A*15 (2000) 2019-2052, hep-ph/0002163. 1.3
- [70] H. Sorge, H. Stocker, and W. Greiner. *Ann. Phys.*, 192:266, 1989. See also H. Sorge, *Phys. Rev. C*52:3291(1995). 1, 4.2.2
- [71] M. Bleicher *et al.* *J. Phys.*, G25:1859, 1999. See also hep-ph/9906398. 1
- [72] K. Werner. *Phys. Rep.*, 232:87, 1993. 1, 4.2.2
- [73] H. J. Drescher, M. Hladik, S. Ostapchenko, and K. Werner. *J. Phys.*, G25:L91, 1999. 1
- [74] X.-N. Wang and M. Gyulassy. *Phys. Rev.*, D44:3501, 1991. 2
- [75] K. J. Eskola and K. Kajantie. *Z. Phys.*, C75:515, 1997. See also hep-ph/9909456 and hep-ph/9906438. 2
- [76] P. Braun-Munzinger. In *Quark Matter*, Torino, Italy, May 10-15, 1999. Also available as nucl-ex/9908007. 3
- [77] K. J. Eskola. In *Quark Matter*, Stony Brook, USA, 2001. Available as hep-ph/0104058. 1-13
- [78] H.-U. Bengtsson and T. Sjostrand. *Comput. Phys. Commun.*, 46:43, 1987. 1.3.1
- [79] B. Andersson, G. Gustafson, and B. Nilsson-Almqvist. *Nucl. Phys.*, B281:289, 1987. 1.3.1
- [80] D. Kharzeev *et al.* *Phys. Lett.*, B507:121–128, 2001. nucl-th/0012025, hep-ph/0111315 and full review: hep-ph/0204014 (cargese summer school lectures). 1.3.2, 1-15, 6.3.3, C

- [81] "rhic design manual". Technical report, BNL, NY, Rev. 1998 and 2000. Available at http://www.agrhome.bnl.gov/NT-share/rhicdm/00_toc1i.htm. 2.1
- [82] D. Beavis *et al* Conceptual design report for the brahms experiment at rhic. Technical report, 1996. Available at <http://www.rhic.bnl.gov/brahms/www/cdr/cdr.html>. See also the review article in *Nucl. Instrum. and Methods* Vol. 499 Issues 2,3 (2003) devoted to RHIC and its experiments. 2.1
- [83] PHENIX Collaboration. Conceptual design report. Technical report, 1993. See also the review article in *Nucl. Instrum. and Methods* Vol. 499 Issues 2,3 (2003) devoted to RHIC and its experiments. 2.1
- [84] PHOBOS Collaboration. Conceptual design report. Technical report, 1995. See also the review article in *Nucl. Instrum. and Methods* Vol. 499 Issues 2,3 (2003) devoted to RHIC and its experiments. 2.1
- [85] STAR Collaboration. Conceptual design report. 1993. See also the review article in *Nucl. Instrum. and Methods* Vol. 499 Issues 2,3 (2003) devoted to RHIC and its experiments. 2.1
- [86] V. I. Vlesker. *Compt. Rend. Acad. Sci. USSR*, 43:329, 1944. 9
- [87] E. M. McMillan. *Phys. Rev.*, 20:143, 1945. 9
- [88] K. Hagiwara *et al* (Particle Data Group). *Phys. Rev.*, D66:010001–1, 2002. See Section on Accelerator Physics. 9
- [89] R. Bindel *et al*. *Nucl. Instr. and Meth. A*, 474:38, 2001. 2.2.1, 3.2.2, 4.1
- [90] C. Adler *et al*. *Nucl. Instr. and Meth. A*, 461:337, 2001. 2.2.1
- [91] A. Baltz *et al*. *Nucl. Instr. and Meth. A*, 417:1, 1998. 2.2.1, 2.2.1
- [92] M. Chiu *et al*. *Phys. Rev. Lett.*, 89:012302, 2002. Electronic version available at <http://www.rhic.bnl.gov/~white/zcal/mcd24.pdf>. 2.2.1
- [93] R. Nouicer *et al* (PHOBOS). *Nucl. Instr. and Meth. A*, 461:143, 2001. 2.2.2, 141

- [94] B. Wadsworth *et al.* *Nuclear Science Symposium Conference Record, IEEE*, pages 76–80, 2001. An expanded version of this article has been submitted to *IEEE Transactions on Nuclear Science*, 2001. 2.3
- [95] Produced by IDE AS, Veritasveien 9, N-1322 Hovik, Norway (using AMS’s 1.2 μm , N-well CMOS, double-metal, double-poly process). The PHOBOS front-end system uses two versions of the front-end chip: VA64-HDR1, with 64 channels; and VA-HDR1 with 128 channels. 2.3.1, B.1
- [96] E. Nygaard, P. Aspell, P. Jarron, P. Weilhammer, and K. Yoshioka. *Nucl. Instr. and Meth. A*, 301:506–516, 1991. 2.3.1, B.1
- [97] O. Toker, S. Masciocchi, E. Nygaard, A. Rudge, and P. Weilhammer. *Nucl. Instr. and Meth. A*, 340:572–579, 1994. 2.3.1, B.1
- [98] E. Griesmayer, H. Fraiss-Kolbl, H. Pernegger, B. Wadsworth, and J. Fitch. *IEEE Trans. Nucl. Sci.*, 48:1565–1569, 2001. 2.3.1, B.1
- [99] V. G. Palmeri *et al.* *Nucl. Instr. and Meth. A*, 413:475–478, 1998. 2.3.3
- [100] B. L. Gregory and B. D. Shafer. *IEEE Trans, Nucl. Sci.*, 20:293, 1973. 2.3.3
- [101] VITA Standards Organization. Serial front panel data port (fpdp), draft standard vita 17.1 - 199x. Draft 0.5, February 26, 2001, 7825 East Gelding Drive, Suite 104, Scottsdale, AZ 85260. 2.3.4
- [102] A. Sukhanov *et al* (PHOBOS Collaboration). *IEEE Transactions on Nuclear Science*, 2001. 2.3.5, 2.3.5
- [103] VITA Standards Organization. Raceway interlink functional specification, standard vita 5 - 1994 and vita 5.1 - 1999. 1994. 1
- [104] ANSI Standards Organization. Ieee standard fastbus modular high-speed data acquisition and control system, ansi/ieee 960-1986. 1986. 2
- [105] R. Brun *et al.* *Linux Journal*, 51, 1998. 2.3.5
- [106] IBM. *HPSS (High Performance Storage System) Ver 4.2 Reference Guide*, 2000. 2.3.5

- [107] <http://www.avistor.com> Avistor Co. *S100 ServerRAID disk array system Reference Guide*, 2000. 2.3.5
- [108] W. R. Leo. *Techniques for Nuclear and Particle Physics Experiments: A How-To approach*. Springer-Verlag, New York, 1991. ISBN 3540173862. 3.1.3, 3.2, 3.2.1
- [109] K. Hagiwara *et al* (Particle Data Group). *Phys. Rev.*, D66:10001, 2002. See Section on ‘Experimental methods and Colliders’ (Particle Detectors). 11, 3-6
- [110] R. Brun *et al*. Geant detector description and simulation tool. Technical report, 1994. CERN Program Library, W5013. The GEANT manual can be found at http://wwwasdoc.web.cern.ch/wwwasdoc/geant_html3/geantall.html. 3.2
- [111] L. D. Landau. *J. Phys. USSR*, 8:201, 1944. 3.2, 3.2.1, B.2
- [112] P. V. Vavilov. *Soviet Physics JETP*, 5:749, 1957. 3.2, 12
- [113] P. Shulek, B. M. Golovin, L. A. Kulyukina, S. V. Medved, and P. Pavlovic. *Yad. Fiz.*, 4:564, 1966. 3.2, 12
- [114] R. M. Sternheimer. *Phys. Rev.*, 145:247, 1966. 12
- [115] F. Q. Wang. *Kaon Production and K/pi Ratios in Au+Au Collisions at 11.09 AGeV/c at the AGS*. PhD thesis, Columbia University, 2001. See chapter 6 on model comparisons. 13
- [116] G. J. Alner *et al* (UA5). *Z. Phys. C*, 33:1, 1986. 6.1.2, 6-4, 6.1.3
- [117] R. P. Feynman. *Phys. Rev. Lett.*, 23:1415, 1969. 15
- [118] D. S. Barton *et al*. *Phys. Rev. D.*, 27:2580, 1983. 15
- [119] P. Deines-Jones *et al*. *Phys. Rev. C.*, 62:014903, 2000. 15
- [120] M. Baker (PHOBOS). *Phys. Rev. Lett.*, 2003. In press, pre-print available as nucl-ex/0210015. 15
- [121] K. Gulbrandsen (PHOBOS). *Phys. Rev. C (Rapid Comm.)*, 67:021901(R), 2003. 16
- [122] J. E. Elias *et al*. *Phys. Rev. Lett.*, 41:285, 1978. 16

- [123] W. Thome *et al.* *Nucl. Phys.*, B129:365–389, 1977. Compilation of ISR $p + p$ data. 6-7
- [124] G. J. Alner *et al* (UA5). *Z. Phys. C*, 33:1, 1986. 6-7
- [125] F. Abe *et al.* *Phys. Rev. D.*, 41:2330, 1990. 6-7
- [126] M. Gazdzicki (NA49). *Phys.Rev.*, C66:054902, 2002. Available as nucl-ex/0205002. 6.1.4, 62
- [127] X.-N. Wang. *Phys. Rev. Lett.*, 86:3496, 2001. 6.3.1
- [128] X.-N. Wang M. Gyulassy, I. Vitev and B-W. Zhang. In R.C. Hwa and X.-N. Wang, editors, *Quark Gluon Plasma 3*. World Scientific, Singapore. Available as nucl-th/0302077, See also nucl-th/0209089. 6.3.1
- [129] X-N. Wang. *Phys. Lett.*, B527:85–91, 2002. hep-ph/9605214. 6.3.1
- [130] C. Adler *et al* (STAR). *Phys. Rev. Lett.*, 89:202301, 2002. Available as nucl-ex/0206011. 6.3.1
- [131] D. Kharzeev *et al.* *Phys. Lett.*, 507:121–128, 2001. Available as nucl-th/0012025. 6.3.2, 6.3.2
- [132] D. Kharzeev *et al.* *Z. Phys.*, C74:307, 1997. 6.3.2
- [133] X-N. Wang. *Phys. Rev. Lett.*, 86:3496, 2001. nucl-th/0008014. 6.3.2
- [134] Lord Kelvin. *Baltimore Lectures on Molecular Dynamics and the Wave Theory of Light*. Cambridge University Press, 1st. Ed., xxi+694., 1904. A.1
- [135] C. M. Bender and T. T. Wu. *Phys. Rev.*, 184:1231–1260, 1969. 23
- [136] E. V. Shuryak. *Phys. Lett.*, B107:103, 1981. See also F. Kartsch and M. Lutgemeier, *Nucl. Phys.* B550:449-464, 1999, for an analysis of QCD with adjoint fermions, in which the deconfinement temperature T_d and chiral symmetry restoration temperature T_c are explicitly found to be different. In addition, see A. Casher *Phy. Lett.* B83:395, 1979. 23
- [137] R. Pisarski and F. Wilczek. *Phys. Rev. D*, 29:338, 1984. A.2

- [138] L. P. Csernai and J. I. Kapusta. *Phys. Rep.*, 131:223, 1986. See also, W. Trautmann in Dronten, 1996, “Correlations and Clustering phenomena in subatomic physics”, nucl-ex/9611002. A.2
- [139] S. P. Klevansky. *Rev. Mod. Phys.*, 64:649, 1992. A.2
- [140] D. Bialin and A. Love. *Phys. Rep.*, 107:325, 1984. See also: M. Alford, K. Rajagopal and F. Wilczek, *Phys. Lett.* B422:247, 1998. A.2
- [141] W. T. Lin *et al.* *Nucl. Instrum. and Meth.*, A389:415–420, 1997. See also [93]. The silicon sensors were fabricated by ERSO of Taiwan. B.1
- [142] Thin Air. 2003. See also ‘Common Sense’. B.1
- [143] G. Cowan. Technical report, University of Siegen, 1995. An excellent ALEPH tech. note (ALEPH 95-101) that compares the virtues of using truncated means to maximum likelihood estimation to extract a particles’ $\beta\gamma$ from measured dE/dx . This note is available at http://www.pp.rhul.ac.uk/~cowan/aleph/landau_note.ps. Fig. B-2 is taken from this document. B.2
- [144] H. D. Maccabee and D. G. Papworth. *Phys. Lett.*, A30:241, 1969. B.2
- [145] K. Gulbrandsen (PHOBOS). Private communication. B.3

Acknowledgments

This thesis would not have been possible without the help and support of a number of people, both within and outside of PHOBOS.

First, I would like to thank my advisor, Bolek Wyslouch. He has been a constant source of encouragement and support through my graduate career (often in a non-intuitive fashion!). He managed the PHOBOS project in its nascent stages and was instrumental in making it a successful experiment. I have learnt a lot through watching him at work, both about physics and about working successfully in an experimental collaboration. I am particularly thankful to him for encouraging me to take time and understand the physics implications of my thesis measurements. In this respect, I would also like to thank Wit Busza, our spokesperson, who has been a great physics mentor to me. Wit's knack for paring a problem down to its bare essentials, and emphasis on understanding one's assumptions thoroughly, has been a great source of inspiration for me. I am also thankful to my thesis committee consisting of Frank Wilczek, Leslie Rosenberg and Gunther Roland, and George Stephans, who taught me the value of questioning everything.

Two people who have been instrumental in my development as an experimental physicist are Bernie Wadsworth and Piotr Kulinich. Through their vastly different approach to solving experimental problems, whether they be in electronics design, ground loop debugging or cable cross-talk, they have taught me the relative importance of pre-thinking one's ideas thoroughly before embarking on an experimental project, and 'learning on the job'. My stay at BNL was made immensely more enjoyable through my close association with Andrei Sukhanov, the resident DAQ guru. I gained invaluable training in assembling, testing and commissioning silicon detectors from Heinz Pernegger and Gerrit van Nieuvenhuizen, who taught me the importance of details. For my thesis analysis on the multiplicity detector, invaluable help was provided by the Illinois gang (they built it after all!). Alan

Wuosmaa, in particular, motivated my initial forays into measuring charged particle distributions, and Rachid Nouicier has been of priceless help in debugging my analysis and taking it many steps further. Peter Steinberg, Mark Baker and Patrick Decowski have helped me understand and appreciate the difficulties of heavy ion physics, and have served as inspiring role models as I embark on my post-doctoral career. In terms of inspiration, I cannot fail to mention Leslie Rosenberg—any person who uses Jackson’s ‘Electrodynamics’ as bedside reading material is pretty cool in my book!

The MIT students, Kris, Conor, Corey, Jay and Carla have been great comrades. My office-mate Kris’s interminable ramblings, often the source of many insights on Life, the Universe and everything else, also gave me plenty of encouragement to finish up my thesis in a hurry. Our secretary Anna, the record-holder for the ‘HIG-secretary-survival’ test, has been of inestimable help in making administrative tasks painless, especially during the long times I spent at BNL.

I would like to especially thank my friends (and room-mates) Augustine, Deep and Ananth who have been a constant source of good humor, cheer, and home-brewed beer. Our hiking and camping trips, the long weekends spent taking cars (and other things) apart not knowing quite how to put them back together, will provide lots of fond memories of graduate school for me. I have Augustine in particular to thank for infecting me with a love of DIY audio electronics and photography, two hobbies that I hope to pursue for a long time to come. I would also like to thank the MIT REUSE community for proving to be an invaluable source of ‘junk’ for my projects,

None of this would have been possible without the support and nurturing of my parents. I have learnt a great deal about life from my Dad’s tenacity and single-minded approach to projects, and my Mom’s remarkable faith in herself and her simple philosophy that ‘everything works out ok in the end’. Finally, I would like to thank the producer-director who made this show a reality—my wife Sahana, whose unflinching support and loving companionship (accompanied by tastily prepared meals!) I hope to cherish forever.

*I dedicate this thesis to my grandfather,
who introduced me to the joy of analytical thinking.*

List of Figures

1-1	Feynman diagrams of QED and QCD	12
1-2	$\alpha_s(Q^2)$ world summary[22]	13
1-4	Lines of force between (a) e^+e^- pair in QED and (b) $q + \bar{q}$ pair in QCD. . .	15
1-3	t'Hooft's conjecture for large N_c	15
1-5	Numerical calculation[44] of pressure P/T^4 variation with temperature T .	19
1-6	$\langle\psi\bar{\psi}\rangle$ and quark free energy function $L(f_q(T))$ as a function of T	21
1-7	Compilation of N_{ch} [49] and $dN_{ch}/d\eta$ [50, 2] in $p + p$	24
1-8	Compilation[53] of p_T distribution of π^- produced in $p + p$ and $p + A$ collisions.	25
1-9	Compilations[53, 56] of $dN_{ch}/d\eta$ in $p + A$ collisions.	26
1-10	Schematic of multiplicity distributions in $p + p$ and $p + A$	27
1-11	$\langle N_{ch} \rangle / (\langle N_{pp} \rangle / 2)$ as a function of $\sqrt{s_{NN}}$ in central $A + A$	28
1-12	Schematic of an $A + A$ collision	29
1-13	Model predictions for $dN_{ch}/d\eta$ at $\eta = 0$ in central Au+Au collisions	31
1-14	HIJING predictions for $dN_{ch}/d\eta$ in Au+Au collisions at $\sqrt{s_{NN}} = 200$ GeV .	32
1-15	Predictions for $dN_{ch}/d\eta$ in Au+Au from Kharzeev <i>et al</i> [80].	34
2-1	Layout of RHIC/AGS	37
2-2	PHOBOS experimental hall	39
2-3	The PHOBOS experiment	40
2-4	a) Design of a single paddle module. b) 16 paddle modules mounted together.	41
2-5	Schematic of a ZDC module	42
2-6	Components of the multiplicity detector	43
2-7	Cross section of a silicon sensor	44
2-8	Layout of the PHOBOS silicon readout system	45

2-9	Partial schematic of VA chip	46
2-10	Schematic of Front-End-Controller signal board	48
2-11	Latch-up protection circuit schematic	50
2-12	Data concentrator for multiplexing data from FECs	52
2-13	Layout of the PHOBOS DAQ	53
2-14	Data acquisition timing diagram	54
3-1	Raw data ADC values from Silicon sensor (1 event)	58
3-2	Calculated noise in ADC units for a typical Octagon sensor	60
3-3	Calculation of common mode shift	61
3-4	Gain calibration	63
3-5	Measured energy loss spectrum	65
3-6	Mean E_{loss} for π 's in Si from Bethe-Bloch equation	66
3-7	Comparison of energy loss spectrum in data and GEANT simulation	68
3-8	Comparison of mean paddle response, DATA and MC	69
4-1	PHOBOS trigger logic	72
4-2	Distribution of 'hit' paddle scintillators in a typical data run	73
4-3	Distribution of δt_{Pdl}	74
4-4	Signal and timing correlation between ZDC and paddle detectors	75
4-5	Truncated signal mean from paddle detectors (DATA(a) and MC(b))	77
4-6	Distribution of $(N_n + N_p)$ for data and MC	78
4-7	Centrality Bins for data, MC and N_{part} distribution	79
4-8	Effect of underestimating the total cross section on the error in $\langle N_{part} \rangle$	80
4-9	Effect of smearing on error in $\langle N_{part} \rangle$	81
4-10	$\langle N_{part} \rangle$ obtained from other MC models, VENUS and RQMD	81
4-11	a) Efficiency of RMSSelVertex b) σ_z of RMSSelVertex as a function of z_{vtx}	83
5-1	Event display	85
5-2	Geometry of energy deposition in pads of multiplicity detector	86
5-3	Algorithm for merging hits in adjacent pads	87
5-4	$\delta E_{minmerge}^{oct}$ applied for hit merging	89
5-5	δE_{corr} as a function of η (before merging)	89

5-6	Determination of $\delta E_{maxmerge}^{oct}$ cut from simulation	90
5-7	Variation of N_{hits} as a function of cut parameter E_0	91
5-8	Geometrical acceptance of multiplicity detectors	92
5-9	Number of dead pads as a function of $N\sigma$ cut	93
5-10	Map of dead pads in octagon and ring detectors	94
5-11	Occupancy corrections based on Poisson statistics	96
5-12	Distribution of energy signals measured in pads near $\eta = 0$ for central events	97
5-13	Occupancy corrections derived from fitting the energy loss distribution . . .	98
5-14	MC versus ‘True’ $dN_{ch}/d\eta$ comparison	100
5-15	Background corrections from HIJING	101
5-16	Background corrections from (a) HIJING, (b) RQMD, and (c) VENUS . .	101
6-1	$dN_{ch}/d\eta$ as a function of η for $\sqrt{s_{NN}} = 130$ GeV and $\sqrt{s_{NN}} = 200$ GeV . . .	105
6-2	$dN_{ch}/d\eta$ as a function of η for $\sqrt{s_{NN}} = 130$ GeV	106
6-3	$dN_{ch}/d\eta$ as a function of η for $\sqrt{s_{NN}} = 200$ GeV	107
6-4	$dN_{ch}/d\eta'$ in central Au+Au and $p + \bar{p}$ collisions.	109
6-5	A $p + \bar{p}$ collision	109
6-6	Comparison of $dN_{ch}/d\eta' / \langle N_{part} \rangle / 2$ between central and peripheral collisions.	111
6-7	$dN_{ch}/d\eta / \langle N_{part} / 2 \rangle$ at $\eta = 0$	113
6-8	Comparison of scaled $dN_{ch}/d\eta'$ with NA49 measurements at $\sqrt{s_{NN}} = 17$ GeV	114
6-9	The integrated N_{ch} yield, scaled by $\langle N_{part} / 2 \rangle$	115
6-10	$dN_{ch}/d\eta$ for $\eta > 0$ (\bullet) versus $\eta < 0$ (\square) reflected about $\eta = 0$	116
6-11	Baseline shifts	117
6-12	Comparison of $dN_{ch}/d\eta^{reconstructed}$ to $dN_{ch}/d\eta^{primary}$ from HIJING	122
6-13	Comparison of measured $dN_{ch}/d\eta$ to predictions from the HIJING	124
6-14	Comparison of measured $dN_{ch}/d\eta$ to two-component fit	126
6-15	Comparison of measured $dN_{ch}/d\eta$ to predictions from semi-classical QCD. .	128
6-16	Comparison of measured $dN_{ch}/d\eta$ near $\eta = 0$ to semi-classical QCD approach	129
A-1	Chirality	131
A-2	Helicity	133
A-3	Helicity flip through Lorentz transformation	134
A-4	Anharmonic oscillator potential	137

A-5	QCD Phase Diagram	138
B-1	Noise model	142
B-2	Landau distribution and Δ_{mp}	144
B-3	Distribution of energy signals measured in pads near $\eta = 0$ for central events	145
C-1	Distribution of merged hits in HIJING, RQMD and VENUS.	150
C-2	Truth versus reconstructed $dN_{ch}/d\eta$ from HIJING, RQMD and VENUS . .	151
C-3	Background corrections from HIJING, RQMD and VENUS	153

List of Tables

2.1	RHIC/AGS/Booster parameters over 3 running periods	38
4.1	Summary of offline cuts	75
4.2	Centrality bins and $\langle N_{part} \rangle$	80
6.1	Summary of Data and Simulation Runs used for analysis.	103
6.2	Summary of systematic errors from various sources	123
B.1	Parameters for the equivalent noise model of a single preamplifier channel. .	142